Biomimetic Rotor-Configuration Design for Optimal Performance in Drone

性能最適化を目指すドローンのロータ構成のバイオミメティクスデザイン

February 2022

YI LI

Graduate School of
Science and Engineering

CHIBA UNIVERSITY

（千葉大学審査学位論文）

Biomimetic Rotor-Configuration Design for Optimal Performance in Drone

February 2022

YI LI

Graduate School of
Science and Engineering

CHIBA UNIVERSITY

Biomimetic Rotor-Configuration Design for Optimal Performance in Drone

Abstract

It is meaningful and significant to improve the aerodynamic performance of drone due to its extensive applications in different fields. Motivated by optimal combination of paired wings configuration and stroke-plane inclination in biological flapping flights that can achieve high aerodynamic performance, we propose a biomimetic rotor-configuration design to explore optimal aerodynamic performance in multirotor drones. With a combination of CFD (Computational Fluid Dynamics)-based simulation and a novel surrogate model, we explore the optimal aerodynamic performance of rotor-configuration in hovering quadrotor drones in terms of the aerodynamic effects of tip distance, height difference and tilt angle of propellers. The rotor-configuration that is capable of optimizing both lift force production and FM efficiency has a large tip distance and some height difference with zero tilt angle, which can affect the tip vortex, the inner vortex sheet and the induced flow (downwash) of each propeller, leading to the least downwash-jet interference between adjacent propellers and maximal interaction between the upper and lower propellers that can increase the induced velocity of the lower propellers, hence resulting in the increase of lift force production and FM efficiency of multirotor, *i.e.* achieving the optimal aerodynamic performance in quadrotor drone. However, this obtained optimal rotor-configuration has a larger frame compared with that in basic rotor-configuration, which is harmful to the agility of drone. Thus, it is an urgency to propose a design to reduce the frame dimension while maintain the high aerodynamic performance of drone. Motivated by the thrust increase of quadcopter with ducted-propeller, we conceive a concept to improve the aerodynamic performance of the quadrotor drone while contract the obtained optimal rotor-configuration by adopting a ducted-propeller design. With a high-performance duct that explored from a series of different duct morphological characteristics, the optimal ducted multirotor configuration that is beneficial to aerodynamic performance improvement and frame contraction is found by employing the high-performance duct in the quadrotor model through the combination of CFD-based simulation and surrogate modeling over a design space associated with tip distance and height difference of ducted propellers. The optimal ducted multirotor configuration that explored from the calculations is a ducted rotor-configuration with a minimal tip distance and an appropriate height difference, resulting from the increase of induced velocity and pressure gradient of lower ducted-propellers and little damage on the downwash-jet separation of adjacent ducted-propellers. Furthermore, during the analyses of non-ducted rotor-configuration, it is also found that the tip distance-induced interactions could most alter lift force production and hence lead to remarked improvement in FM efficiency, and the height difference also plays a key role in the improvement of aerodynamic performance, while the tilt angle effect is less important. Whereas, as to the ducted multirotor configuration, it is indicated that the tip distance-induced interactions have a noticeable effect in impairing the lift force production and FM efficiency but are limited to small tip distances, while the height difference-induced interactions have an impact on enhancing the aerodynamic performance over a certain range. Eventually, we conduct an experiment to investigate the effect on aerodynamic performance of non-ducted multirotor configuration for validating the conclusions obtained from numerical simulations. In addition, with the fabrication of high-performance duct and a novel assembly design for the ducted-propeller, the effect on aerodynamic performance of ducted multirotor configuration is also carried out for the validation experimentally. According to the experimental results, it proves that the effects of non-ducted and ducted multirotor configuration on aerodynamic performance investigated by numerical simulations are consistent with the findings obtained from experiment, which means that the biomimetic rotor-configuration design is convincing and reliable in improving the aerodynamic performance of quadrotor drone, and it is also valuable and practical for the optimal design in quadrotor drone.

Key Words: bioinspiration, rotor-configuration, ducted-propeller, aerodynamic performance, aerodynamic interaction, computational fluid dynamics, surrogate modeling

Acknowledgements

First and foremost, I want to express the depth of my gratitude to my supervisor, Pro. Hao Liu, for his generosity of giving me the opportunity to enter our lab and start the research on the biomimetics and biomechanics. I truly appreciate him for having the confidence on me when I met the difficulties in the research, and giving me the freedom and intelligent instruction during the pursuit of my research. I am also grateful for his kind support, constant patience, valuable suggestion and encouragement, as well as his great effort made to revise and review my thesis.

I would also like to thank Prof. Toshiyuki Nakata, Ryusuke Noda, Wei Wang, Koichi Yonezawa and Dr. Gen Li, Yi Yang for their guidance and advice on my research. Particularly, I am thankful to Prof. Koichi Yonezawa for helping and guiding in the field of quadrotor drone experiment.

I want to thank the teachers and faculty members in Chiba University as well for their patient teaching in my Japanese language courses and selfless help in any situations I met in the campus, and also thank the Chiba university for providing the support during my research in Japan.

I am also grateful to the members in Liu-lab for the tutoring guidance provided by Testuya Ueda in my first year living in Japan, the large assistance in the experiment of my research provided by Ryo. Aoki, and Dr. Jianwei Sun, the instruction of device utilization and the introduction of life in Japan given from Dr. Sakito Koizumi, Dr. Yuta Murayama, Kenta Ishibashi and other Japanese students, the valuable suggestion and great help supplied by Dr. Di Chen, Xiancheng Zhang, Ru Xu, Xuefei Cai, Jinxin Wang as well as the happy time obtained from the spending together with Dr. Jiaxin Rong, Yujing Xue, Ruichen Li, Sirui Wang and other Japanese and Chinese students.

Finally, I am greatly and genuinely appreciative of the support and encouragement from my grandpa, parents, brother and sister, as well as the accompanying and sacrifice from my girlfriend Qiqi Cao during the period of my research and life in Chiba University, Japan.

This work was supported by the Grant-in-Aid for Scientific Research of KAKENHI No. 19H02060, 19H00750, JSPS and a Global Prominent Research Program, Chiba University.

Yi Li
Chiba University
February 2022

Table of Contents

List of Figures

List of Tables

Chapter 1 General Introduction

1.1 Introduction of drone

The drone being capable of vertical take-off and landing (VTOL) that is called unmanned aerial vehicle (UAV) or micro air vehicle (MAV), has a great development and draws much interest in researches and applications of different fields during the past years [1-5]. The vertical flight idea has been conceived and developed for centuries in human civilization, being realized firstly in 1907 known as a helicopter named Gyroplane (Figure 1-1a) built by Breguet brothers but was limited in mobility and range of flight [1]. Later in 1920s, a more stable VTOL quadcopter with a name of Oemichen 2 (Figure 1-1b) was constructed by Etienne Oemichen [1-4]. And contemporaneously, George De Bothezat designed and fabricated a similar quadcopter which was named as De Bothezat (Figure 1-1c) [1-5]. However, these early quadrotors were hard to control because it was difficult to adjust the four rotors rotating in a same speed for lacking of the digital computers or sensors, which made the early quadrotors inefficient and unpractical for the utilization and transportation [1]. Besides, these early quadrotors always had many additional rotors equipped on different locations in the quadrotors for additional stability, which led to the complexity and unreliability of the design of quadrotors [1]. After world war II, owing to the development of materials and engineering practices, a more controllable quadcopter named Covertawings Model A (Figure 1-1d) was exploited and constructed by D.H. Kaplan during the 1950s [1-4]. After that, the quadrotors drew little attention until the 1990s.

Since the mid-1990s, the small UAV had a greater and larger development due to the advancement of technology, and the interest drawing from military and commerce [5]. Furthermore, nowadays the drone realizes a more fast and extensive development because of its vast potentiality in application, which has been mainly developed and formed into three different prototypes in the UAV or MAV [1,6-9], being categorized to be the fixed wing drone (Figure 1-2a) [9-14], the rotary wing drone (Figure 1-2b) [8,9,15-19], and the flapping wing drone (Figure 1-2c) [9,20-24]. Moreover, bioinspired by the flight performance of birds and insects, some creative drones or function integrated drones are also designed and tested, such as the drone with flexible or foldable wings (Figure 1-3a) [25-29], the drone with collision resilient structures (Figure 1-3b) [30,31], the drone with integrated functions of walking and flying (Figure

1-3c) [32,33] and so on. Considering the windy or gusty condition outdoors, hovering capability indoors, endurance in hovering and frame size, the rotary wing drone may be a more practical and valuable option for the majority of missions due to its hover and flight capabilities [1,8]. Particularly, the quadrotor drone is a widely used type of the rotary wing UAVs because of its small size, mechanical simplicity, large operational envelopes, outstanding maneuverability, unique flight capacity, controllable agility, excellent flight stability and low cost [1, 6-8]. Due to these merits and advantages, it is extensively used for surveillance, reconnaissance, border patrol monitoring, assault and uninhabited combat aerial vehicle in military field, search and rescue, terrain and environment mapping, firefighter, traffic monitoring, agricultural operation, as well as pollution detection in civil field [1,6-9].

For the sake of completing various missions accurately and perfectly, the quadrotor drone should possess some fantastic characteristics including robust, stability, controllability, practicability, high efficiency, long aerial endurance, and so on [1,6-8]. In order to realize these goals, many researches have been conducted and are mainly classified into the hardware and software categories, where it refers to the hardware researches comprising of the improvement of the components of drone by optimizing their blade flapping, induced velocity distribution, angle of attack, and even air flow distribution [34,35], modification of the configuration of drone by compacting the frame [6], optimization of the rotor-rotor and rotor-fuselage interactions for the aerodynamic performance improvement [7], refinement of the drone structure for elevating the capacity of flight endurance by optimizing the propulsion system, battery system, blade number, and wight [36-39]. On the other side, it refers to the software researches about the creation of quadrotor drone model aiming to examine different control strategies [40-43] relative to the software installed in the drone regarding perfecting the control methods of PID, LQR, backstepping feedback, sliding mode and the integration of these methods [44-47], enriching the controller utilizing vision control of compound eye or cinema [48,49], and integrating different control strategies for autonomous mission or swarm communication [50,51], which aims to promote the stability, agility and controllability of drone [52-54]. Furthermore, as the development of lightweight materials, manufacture, and sensors, as well as the great progress in flight dynamics, control, navigation, and lift capabilities [1], it makes some creative concepts and designs of quadrotor drone to be feasible and realizable, which is potential for improving the flight controllability of quadrotor drone, such as tilting propeller [55-59], potable fuselage [60], and ducted propeller [61-64] as depict in Figure 1-4.

Beyond these previous researches, it is still significant and meaningful to improve the aerodynamic performance of drone due to its increasingly extensive application in different fields, which aims to realize the long endurance of the flight, the less cost of the power, and the high efficiency of the drone system. Thus, we exert ourselves to improve the aerodynamic performance of quadrotor drone from the enlightenment of biomimetics that provides some bioinspired concepts for the design of quadrotor drone from the exquisite flight performance of flying birds or insects [65-69]. Motivated by optimal combination of paired wings configuration and stroke-plane inclination in biological flapping flights that can achieve high aerodynamic performance [70-73], we propose a biomimetic rotor-configuration design to explore optimal aerodynamic performance in multirotor drones. Furthermore, motivated by the improvement of tidal turbine performance realized by multirotor fence configuration [74], and thrust increase of quadcopter with ducted-propeller [75], we conceive a concept to maintain or further improve the aerodynamic performance of multirotor drones with contracting the former obtained optimal rotor-configuration by adopting the ducted-propeller design. As the aerodynamic capabilities in different configurations will be indicative for the design of required adjustment in the drone’s flight, the aerodynamic performance of these biomimetic design in steady statue will be analyzed numerically. Moreover, beyond the analyses from numerical simulations to examine these concepts, we also conduct systematic experiments to validate the conclusions obtained from the investigations of these biomimetic design concepts in the end.

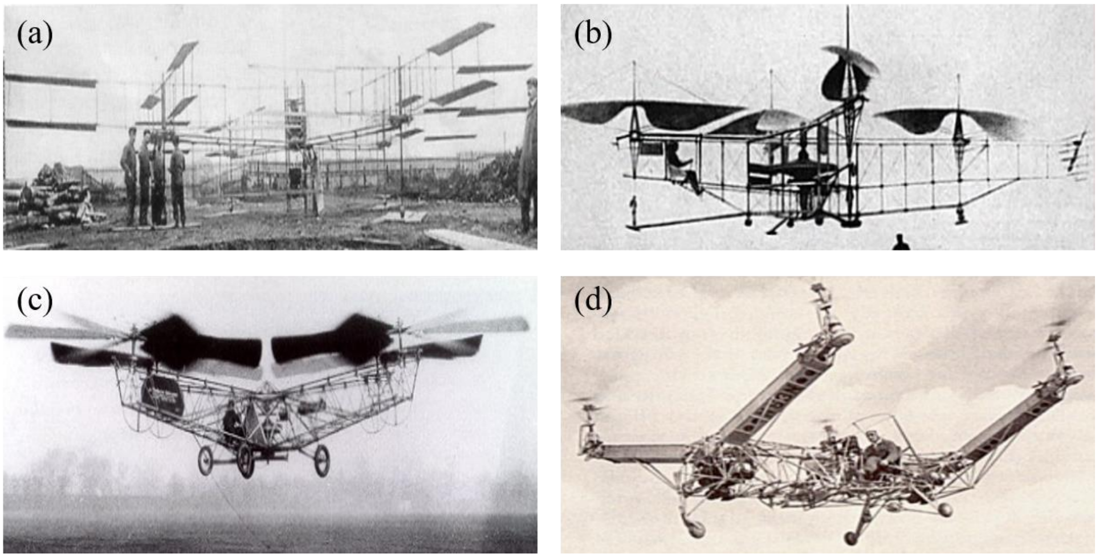

Figure 1-1 Illustration of the early quadrotor prototype. (a) The Gyroplane [1]; (b) the Oemichen 2 [1-4]; (c) the De Bothezat [1-5]; (d) the Convertawings, Model A [1-4].

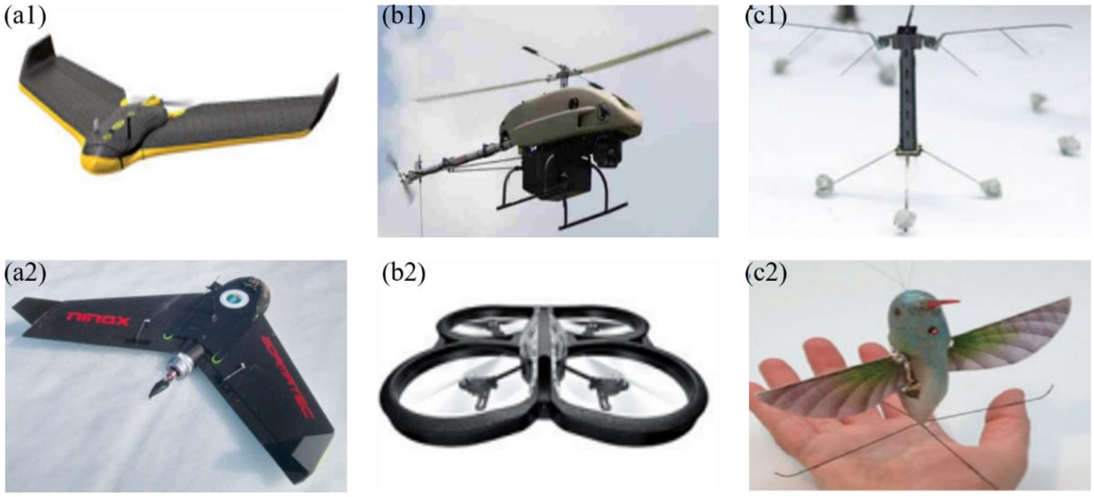

Figure 1-2 Illustration of different categories of drone. (a1 - a2) Fixed wing drones of eBee [9] and UAV BORMATEC Ninox [12]; (b1 – b2) rotary wing drones of conventional single-main-rotor (SMR) MAV [8] and AR. Drone 2.0 [9]; (c1 – c2) flapping wing drones of RoboBee [9] and Nano Hummingbird [9].

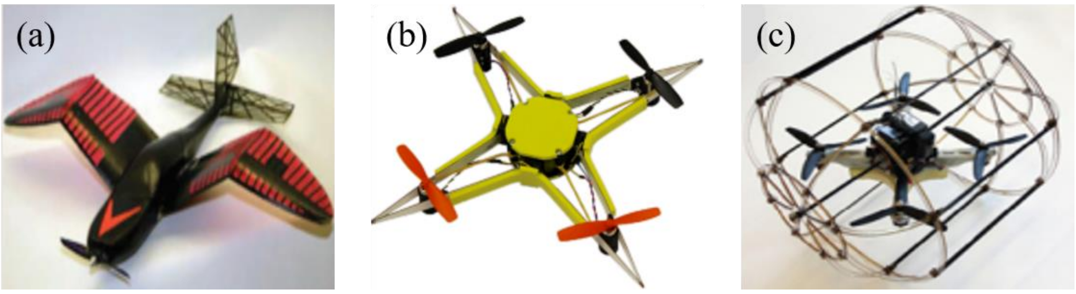

Figure 1-3 Illustration of the creative drones. (a) Drone with flexible wing [27]; (b) drone of collision resilient [30]; (c) drone with hybrid function of walking and flying [32].

Figure 1-4 Illustration of the quadrotor drone with creative design. (a) Drone with tilt rotor [59]; (b) drone being potable with foldable structures [60]; (c) drone with ducted rotors [64].

1.2 Contributions of biomimetic rotor-configuration design for drone

The biomimetic rotor-configuration is potential to improve the aerodynamic performance of quadrotor drone bioinspired from the flight of insects and birds. Thus, the concept of biomimetic rotor-configuration design was conceived and analyzed to explore the optimal aerodynamic performance associated with lift force production and FM efficiency in the quadrotor drone. Further, the ducted-propeller design was also utilized for the aerodynamic performance improvement of quadrotor drone. What's more, the designs of biomimetic rotor-configuration with and without ducts are probably potential to contribute other performances of quadrotor drone associated with ground effect, aero-acoustic, and controllability because of the aerodynamic variation of each propeller caused by the rotor-configuration designs and duct utilization.

Firstly, owing to that the direction related to the quadrotor layout heavily determines the outwash from the quad rotors and the wake is related to the vortex [67,76], the biomimetic non-ducted rotor-configuration can generate a different outwash from the quad rotors compared with the basic rotor-configuration, which will affect the ground effect of quadrotor drone. Furthermore, as the duct impacts the induced flow and the wake of the propeller, it will also have an influence on outwash from quad rotors compared with the rotor-configuration without duct, which means that the biomimetic rotor-configuration and ducted rotor-configuration will both affect the ground effect of quadrotor drone.

Furthermore, due to the vortex shedding noise around biomimetic airfoil can be restrained by some biomimetic structures with transforming the shedding vortices in laminar mode to regular horseshoe-type vortices in the wake, and reducing the spanwise correlation of large-scale vortices [77], as well as that the main source of drone noise comes from the interaction between airflow and drone structure [78], it is reasonably considered that the aerodynamic interactions of quad rotors caused by the biomimetic rotor-configuration and ducted rotor-configuration probably have an influence on the overall sound pressure levels (OASPLs) around the multi propellers, which may affect the aero-acoustic performance of the quadrotor drone in these rotor-configuration designs of biomimetics and duct utilization.

In addition, the quadrotor drone conventionally realizes the flight through one pair of propellers rotating in a clockwise direction, while the other pair of propellers rotating in an anticlockwise direction, which makes the drone flight be controlled by changing the rotational speed of each propeller [1]. As well, this approach is capable of balancing the moment created by each of the spinning rotor pairs [1]. However, the limitation of this classical design is that it needs to control the six outputs of dimensional position and attitude with only four independent control inputs, which is impossible to control the six outputs independently [1]. As for the solution of this problem, the biomimetic design associated with tilting propeller or other measures may be a potential alternative [79,80]. Besides, the biomimetic design associated with tip distance and height difference also affect the moment of spinning propellers, which may also affect the controllability and maneuverability of quadrotor drones due to that the aerodynamic has an influence on the controllability of quadrotor [81-83]. Beyond the effect on maneuverability, as the control strategy has been changed with the biomimetic tilting propeller or height different propeller, the power output for the maneuverability will be different from the traditional control strategy, which can increase the endurance of drone probably. Moreover, as the duct can generate an additional moment, it may also take an effect on the drone maneuverability on windy or gusty condition.

Beyond these, the biomimetic rotor-configuration may provide a choice for the layout of fuselage. In addition, the duct surrounding the propeller may provide a protection for the drone from collision with ground or other obstacles during the flight.

1.3 Objective and outline

There are many approaches to research the aerodynamic performance of airfoil or quadrotor drone, such as the CFD-based simulation [84-86]. However, as the high fidelity CFD model costs too much in the course of calculation, it is necessary to adopt an approximative approach to solve the solution in a consecutive parameter design space, such as the surrogate model which is effective in approximation problem [87-92]. Thus, it is feasible to adopt the CFD-and surrogate model-fusion method in the airfoil design and other optimization problems [93-97]. In this study, we adopt the method of CFD simulation combining the surrogate modeling to examine the effects on aerodynamic performance in various non-ducted/ducted rotor-configurations and explore the optimal rotor-configuration in terms of the aerodynamic effects.

The objective of biomimetic rotor-configuration design is first to create the multi-rotor (propeller) models with different rotor-configurations based on the 3D model of single propeller from the quadrotor drone of DJI phantom 3 advanced (as illustrated in Figure 1-5). Then an extensive CFD-based analysis is carried out to investigate the effects on aerodynamic performance of different rotor-configurations in hovering in terms of the configuration parameters associated with tip distance, height difference and tilt angle. Furthermore, an analysis is conducted to explore the optimal rotor-configuration in this typical multi-rotor drone, which can optimize aerodynamic performance through over a broad parameter space by combining CFD-based simulations and a novel surrogate modeling. Eventually, a rotor-configuration with a large tip distance and some height difference with zero tilt angle is explored (as illustrated in Figure 1-6), being enable to optimize both lift force production and FM efficiency, which thus could offer a novel optimal design for multirotor UAVs.

In addition, the objective of ducted rotor-configuration design is first to explore a high-performance duct design in terms of duct cross-section, tip clearance and duct volume based on a series of CFD simulations relative to the single propeller model assembled with a duct. Then, this novel duct design is equipped to the former obtained optimal multirotor model (Figure 1-6) to investigate the effect of ducted multirotor configuration on aerodynamic performance through adjusting tip distance and height difference of ducted propellers. Eventually, the optimal ducted multi-propeller configuration will be examined by an extensive analysis in a broad-parameter space of the tip distance and height difference through the combination of CFD-based simulations and surrogate modeling, which is verified to improve both lift force production and FM efficiency, being expected to provide a potential optimal design for ducted multirotor UAVs.

What’s more, a series of experiments are conducted to validate the findings from numerical simulations ultimately. Thus, the outline of this thesis is mainly comprised by the optimization of non-ducted rotor-configuration in chapter 2, the optimization of ducted rotor-configuration in chapter 3, the experiment validation in chapter 4 and the conclusions and perspectives in chapter 5.

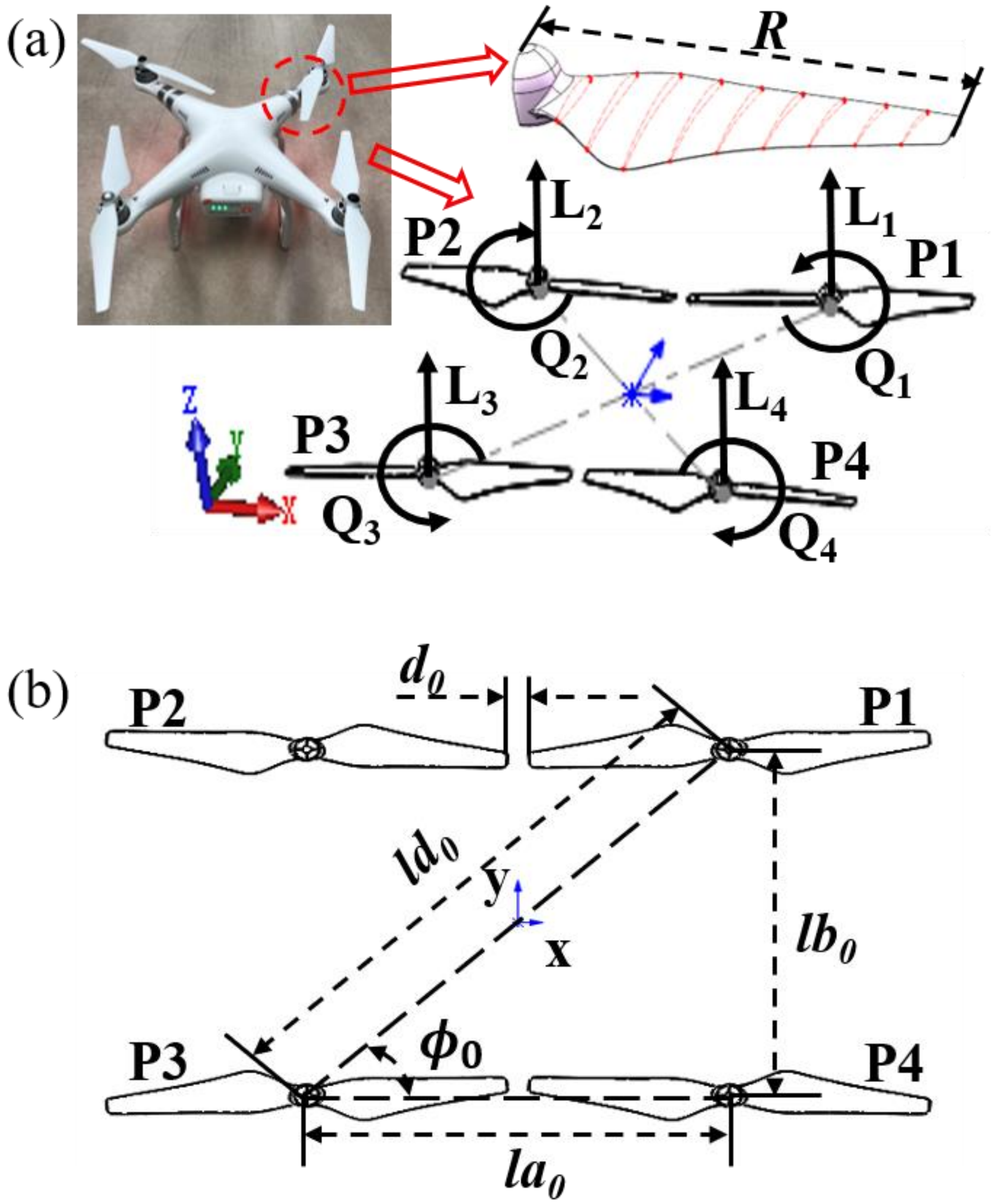

Figure 1-5 Illustration of the basic quadrotor configuration and morphological parameters. (a) Propellers from quadrotor copter (DJI phantom 3 advanced) with radius $R = 0.12$m, and definitions of vertical force (L) and torques (Q); (b) basic rotor-configuration with $la_0 \approx 0.252$m, $lb_0 \approx 0.243$m, $ld_0 = 0.35$m, $d_0 \approx 0.012$m, $\phi_0 \approx 44°$.

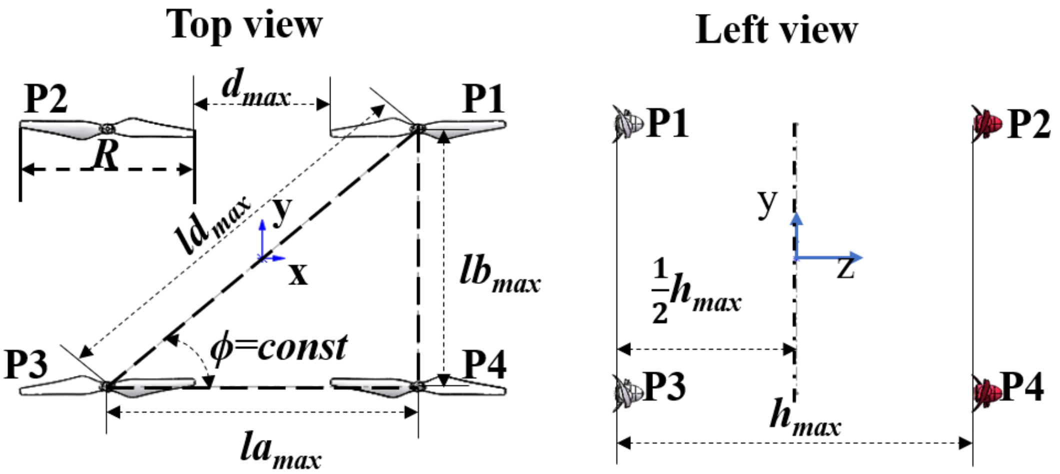

Figure 1-6 Illustration of the quadrotor in maximum (optimal) multi-propeller configuration. Morphological parameters: la_{max} ≈0.425 m, lb_{max} ≈0.410 m, ld_{max} =0.59 m, d_{max} ≈0.185 m, $\emptyset$ ≈44°at height difference, h_{max} = 0.24 m.

Reference

[1] Nemati A. Designing , Modeling and Control of a Tilting Rotor Quadcopter. 2016, 1–128.

[2] DiCesare A, Gustafson K, Lindenfelzer P. Design Optimization of a Quad-Rotor Capable of Autonomous Flight. 2008, 83.

[3] Balakrishnan S. Duct Fanned Shielding Design for Quadrotors. 2016.

[4] Senasi Annamalai. Fractured penis: two case reports. *Med J Malaysia.*, 1986, 41, 278–280.

[5] Diana de Sousa Baptista Morais Carvalho I, Aeronáutica E, Miguel Ângelo Rodrigues Silvestre D. Low Reynolds Propellers for Increased Quadcopters Endurance. *Hélices de Baixo Reynolds para Aumento da Autonomia em Quadricópteros*, 2013.

[6] Chopra I. Optimal propulsion system design for a micro quadrotor. 2011.

[7] Aleksandrov D. Light-Weight Multicopter Structural Design for Energy Saving. 2013.

[8] Bogdanowicz CM. Experimental Investigation of a Quad-rotor Biplane Micro Air Vehicle. 2015, 139.

[9] Floreano D, Wood RJ. Science, technology and the future of small autonomous drones. *Nature*, 2015, 521, 460–466. https://doi.org/10.1038/nature14542.

[10] Gunarathna JK, Munasinghe R. Development of a quad-rotor fixed-wing hybrid unmanned aerial vehicle. *MERCon 2018 - 4th Int. Multidiscip. Moratuwa Eng. Res. Conf., IEEE*, 2018, 72–77. https://doi.org/10.1109/MERCon.2018.8421941.

[11] Jackson SP. Controlling Small Fixed Wing UAVs to Optimize Image Quality from On-Board Cameras. *ProQuest Diss Theses.*, 2011, 3498833:138.

[12] Pfeifer C, Barbosa A, Mustafa O, Peter HU, Rümmler MC, Brenning A. Using fixed-wing uav for detecting and mapping the distribution and abundance of penguins on the South Shetlands Islands, Antarctica. *Drones*, 2019, 3, 1–22. https://doi.org/10.3390/drones3020039.

[13] Fari S. Guidance and control for a fixed-wing UAV. *MSc Thesis, Politec Mliano*, 2017.

[14] Beard R, Kingston D, Quigley M, Snyder D, Christiansen R, Johnson W, et al. Autonomous vehicle technologies for small fixed-wing UAVs. *J Aerosp Comput Inf Commun.*, 2005, 92–108. https://doi.org/10.2514/1.8371.

[15] Mian AA, Wang D. Modeling and backstepping-based nonlinear control strategy for a 6 DOF quadrotor helicopter. *Chinese J Aeronaut*., 2008, 21, 261–268. https://doi.org/10.1016/S1000-9361(08)60034-5.

[16] Runcharoon K. Sliding mode control of quadrotor. 2013, 552–557. https://doi.org/10.1109/TAEECE.2013.6557334.

[17] Zlatanov N. Multirotor Aircraft Dynamics, Simulation and Control. 2016.

[18] Elfeky M, Elshafei M, Saif AWA, Al-Malki MF. Modeling and simulation of quadrotor UAV with tilting rotors. *Int J Control Autom Syst*., 2016, 14, 1047–1055. https://doi.org/10.1007/s12555-015-0064-5.

[19] Ucgun H, Yuzgec U, Bayilmis C. A review on applications of rotary-wing unmanned aerial vehicle charging stations. *Int J Adv Robot Syst*., 2021, 18, 1–20. https://doi.org/10.1177/17298814211015863.

[20] Hasan N, Sabbir FH, Mortuza G, Haque E. Design and Model Construction of a Flapping Wing UAV Ornithopter. *Int Conf Mech Ind Energy Eng.,* 2016, 1–5.

[21] Han J, Lee J, Kim D. Bio-inspired flapping UAV design: a university perspective. Heal. *Monit. Struct. Biol. Syst. 2009*, vol. 7295, 2009, 72951I. https://doi.org/10.1117/12.815337.

[22] Chin YW, Kok JM, Zhu YQ, Chan WL, Chahl JS, Khoo BC, et al. Efficient flapping wing drone arrests high-speed flight using post-stall soaring. *Sci Robot.*, 2020, 5. https://doi.org/10.1126/scirobotics.aba2386.

[23] Bin Abas MF, Bin Mohd Rafie AS, Bin Yusoff H, Bin Ahmad KA. Flapping wing micro-aerial-vehicle: Kinematics, membranes, and flapping mechanisms of ornithopter and insect flight. *Chinese J Aeronaut*., 2016, 29, 1159–1177. https://doi.org/10.1016/j.cja.2016.08.003.

[24] Nozawa T, Nakamura K, Katsuyama R, Kuwajima S, Li Z, Nomizu A, et al. The wifly: Flapping-wing small unmanned aerial vehicle with center-of-gravity shift mechanism. *J Robot Mechatronics,* 2021, 33, 205–215. https://doi.org/10.20965/jrm.2021.p0205.

[25] Dufour L, Owen K, Mintchev S, Floreano D. A drone with insect-inspired folding wings. *IEEE Int. Conf. Intell. Robot. Syst.*, vol. 2016-Nov., 2016, 1576–1581. https://doi.org/10.1109/IROS.2016.7759255.

[26] Kovač M, Zufferey JC, Floreano D. Towards a self-deploying and gliding robot. *Fly. Insects Robot.*, 2010, 271–284. https://doi.org/10.1007/978-3-540-89393-6_19.

[27] Brenchley PJ, Harper DAT, Brenchley PJ, Harper DAT. Adaptive morphology. *Palaeoecology*, 1998, 103–147. https://doi.org/10.1007/978-1-4684-1410-3_4.

[28] Di Luca M, Mintchev S, Heitz G, Noca F, Floreano D. Bioinspired morphing wings for extended flight envelope and roll control of small drones. *Interface Focus*., 2017, 7. https://doi.org/10.1098/rsfs.2016.0092.

[29] Hedayatpour M, Mehrandezh M, Janabi-Sharifi F. A unified approach to configuration-based dynamic analysis of quadcopters for optimal stability. *IEEE Int. Conf. Intell. Robot. Syst.*, vol. 2017-Sep., 2017, 5116–5121. https://doi.org/10.1109/IROS.2017.8206397.

[30] Mintchev S, Rivaz S De, Floreano D, Member S. Insect-inspired mechanical resilience for multicopters. *IEEE*, 2017, 1248-1255.

[31] Briod A, Kornatowski P, Zufferey JC, Floreano D. A collision-resilient flying Robot. *J F Robot.*, 2014, 31, 496–509. https://doi.org/10.1002/rob.21495.

[32] Daler L, Mintchev S, Stefanini C, Floreano D. A bioinspired multi-modal flying and walking robot. *Bioinspiration and Biomimetics,* 2015, 10. https://doi.org/10.1088/1748-3190/10/1/016005.

[33] Vidyasagar A, Zufferey JC, Floreano D, Kovač M. Performance analysis of jump-gliding locomotion for miniature robotics. *Bioinspiration and Biomimetics,* 2015, 10, 1–12. https://doi.org/10.1088/1748-3190/10/2/025006.

[34] Hoffmann GM, Huang H, Waslander SL, Tomlin CJ. Quadrotor helicopter flight dynamics and control: Theory and experiment. *Collect. Tech. Pap. - AIAA Guid. Navig. Control Conf. 2007,* vol. 2, 2007, 1670–1689. https://doi.org/10.2514/6.2007-6461.

[35] Dumitrache A, Pricop M-V, Niculescu M-L, Cojocaru M-G, Ionescu T. Design and analysis methods for UAV rotor blades. *Sci Res Educ AIR FORCE,* 2017, 19, 115–126. https://doi.org/10.19062/2247-3173.2017.19.1.48.

[36] Winslow J, Benedict M, Hrishikeshavan V, Chopra I. Design, development, and flight testing of a high endurance micro quadrotor helicopter. *Int J Micro Air Veh.*, 2016, 8, 155–169. https://doi.org/10.1177/1756829316653694.

[37] Dai X, Quan Q, Cai KY. Design automation and optimization methodology for electric multicopter UAVs. *ArXiv.*, 2019, 1–27.

[38] Ampatis C, Papadopoulos E. Parametric design and optimization of multi-rotor aerial vehicles. *Proc - IEEE Int Conf Robot Autom.*, 2014, 30, 6266–6271. https://doi.org/10.1109/ICRA.2014.6907783.

[39] Dai X, Quan Q, Ren J, Cai KY. An analytical design-optimization method for electric propulsion systems of multicopter UAVs with desired hovering endurance. *IEEE/ASME Trans Mechatronics,* 2019, 24, 228–239. https://doi.org/10.1109/TMECH.2019.2890901.

[40] Kim J, Gadsden SA, Wilkerson SA. A Comprehensive Survey of Control Strategies for Autonomous Quadrotors. *ArXiv.*, 2020, 1–14. https://doi.org/10.1109/CJECE.2019.2920938.

[41] Zulu A, John S. A Review of Control Algorithms for Autonomous Quadrotors. *Open J Appl Sci.,* 2014, 04, 547–556. https://doi.org/10.4236/ojapps.2014.414053.

[42] Önder Efe M. Sliding mode control for unmanned aerial vehicles research. *Stud. Syst. Decis. Control*, vol. 24, 2015, 239–255. https://doi.org/10.1007/978-3-319-18290-2_12.

[43] Sadr S, Moosavian SAA, Zarafshan P. Dynamics modeling and control of a quadrotor with swing load. *J Robot.,* 2014. https://doi.org/10.1155/2014/265897.

[44] Moussid M, Sayouti A, Medromi H. Dynamic Modeling and Control of a HexaRotor using Linear and Nonlinear Methods. *Int J Appl Inf Syst.,* 2015, 9, 9–17. https://doi.org/10.5120/ijais2015451411.

[45] Njinwoua BJ, Wouwer A Vande. Cascade attitude control of a quadcopter in presence of motor asymmetry. *IFAC-PapersOnLine*, vol. 51, Elsevier B.V., 2018, 113–118. https://doi.org/10.1016/j.ifacol.2018.06.055.

[46] Wang P, Man Z, Cao Z, Zheng J, Zhao Y. Dynamics modelling and linear control of quadcopter. *Int. Conf. Adv. Mechatron. Syst. ICAMechS, IEEE*, 2016, 498–503. https://doi.org/10.1109/ICAMechS.2016.7813499.

[47] Xuan-Mung N, Hong SK. Improved altitude control algorithm for quadcopter unmanned aerial vehicles. *Appl Sci.*, 2019, 9. https://doi.org/10.3390/app9102122.

[48] Leitel R, Brückner A, Buß W, Viollet S, Pericet-Camara R, Mallot H, et al. Curved artificial compound-eyes for autonomous navigation. *Micro-Optics 2014*, vol. 9130, 2014, 91300H. https://doi.org/10.1117/12.2052710.

[49] McCarthy C, Barnes N. Performance of temporal filters for optical flow estimation in mobile robot corridor centring and visual odometry. *Australas. Conf. Robot. Autom.*, 2003.

[50] Huang H, Hoffmann GM, Waslander SL, Tomlin CJ. Aerodynamics and control of autonomous quadrotor helicopters in aggressive maneuvering. *Proc. - IEEE Int. Conf. Robot. Autom., IEEE*, 2009, 3277–3282. https://doi.org/10.1109/ROBOT.2009.5152561.

[51] Hernandez A, Copot C, De Keyser R, Vlas T, Nascu I. Identification and path following control of an AR.Drone quadrotor. *2013 17th Int. Conf. Syst. Theory, Control Comput. ICSTCC 2013*; *Jt. Conf. SINTES 2013, SACCS 2013, SIMSIS 2013 - Proc., IEEE*, 2013, 583–588. https://doi.org/10.1109/ICSTCC.2013.6689022.

[52] Capello E, Guglieri G, Quagliotti F. A design configuration and optimization for a multi rotor UAV. *NATO RTO Symp Intell.*, 2009, 1–20.

[53] Kumar V, Michael N. Opportunities and challenges with autonomous micro aerial vehicles. *Springer Tracts Adv. Robot.*, vol. 100, 2017, 41–58. https://doi.org/10.1007/978-3-319-29363-9_3.

[54] Tarek N.Dief and SY. Review: Modeling and Classical Controller Of Quad-rotor. *IRACST - Int J Comput Sci Inf Technol Secur.*, 2015, 5, 314–319.

[55] Ryll M, Bülthoff HH, Giordano PR. Modeling and control of a quadrotor UAV with tilting propellers. *Proc. - IEEE Int. Conf. Robot. Autom.*, 2012, 4606–4613. https://doi.org/10.1109/ICRA.2012.6225129.

[56] Ryll M, Bulthoff HH, Giordano PR. First flight tests for a quadrotor UAV with tilting propellers. *Proc. - IEEE Int. Conf. Robot. Autom.*, 2013, 295–302. https://doi.org/10.1109/ICRA.2013.6630591.

[57] Ferrarese G, Giulietti F, Avanzini G. Modeling and simulation of a quad-tilt rotor aircraft. *IFAC Proc. Vol.*, vol. 2, IFAC, 2013, 64–70. https://doi.org/10.3182/20131120-3-FR-4045.00037.

[58] Fukuda T, Sakaguchi A, Takimoto T, Ushio T. Modeling and Stabilization of the Novel Quadrotor with Tilting Propeller. 2016, 173–176.

[59] Henrique Bezerra Diógenes, Davi Antônio dos Santos. Modelling, Design and Simulation of a Quadrotor with Tilting Rotors Actuated by a Memory Shape Wire. *An. do IX Congr. Nac. Eng*. Mecânica, 2016. https://doi.org/10.20906/cps/con-2016-0452.

[60] Mintchev S, Daler L, L'Eplattenier G, Saint-Raymond L, Floreano D. Foldable and self-deployable pocket-sized quadrotor. *Proc. - IEEE Int. Conf. Robot. Autom.*, vol. 2015- June, IEEE, 2015, 2190–2195. https://doi.org/10.1109/ICRA.2015.7139488.

[61] L.Pereira J. Hover and Wind-Tunnel Testing of Shrouded Rotors for Improved Micro Air Vehicle Design. *PhD Thesis,* 2008, 349.

[62] Zubair J. Design and implementation of a shrouded rotor for increasing quadrotor performance. 2017.

[63] Lal H. Efficiency based flight analysis for a novel quadrotor system. 2019.

[64] Yonezawa K. Aerodynamic Characteristics of a Quad-Rotor-Drone with Ducted Rotors. *8th Asian/Australian Rotorcraft Forum,* Mitaka, Tokyo, Japan, 2019, 1–7.

[65] Henningsson P, Bomphrey RJ. Time-varying span efficiency through the wingbeat of desert locusts. *J R Soc Interface.* 2012, 9, 1177–1186. https://doi.org/10.1098/rsif.2011.0749.

[66] Le TQ, Van Truong T, Tran HT, Park SH, Ko JH, Park HC, et al. How could beetle's elytra support their own weight during forward flight? *J Bionic Eng.,* 2014, 11, 529–540. https://doi.org/10.1016/S1672-6529(14)60065-2.

[67] Henningsson P, Michaelis D, Nakata T, Schanz D, Geisler R, Schröder A, et al. The complex aerodynamic footprint of desert locusts revealed by large-volume tomographic particle image velocimetry. *J R Soc Interface.* 2015, 12. https://doi.org/10.1098/rsif.2015.0119.

[68] Tobalske BW, Warrick DR, Clark CJ, Powers DR, Hedrick TL, Hyder GA, et al. Three-dimensional kinematics of hummingbird flight. *J Exp Biol.,* 2007, 210, 2368–2382. https://doi.org/10.1242/jeb.005686.

[69] Clark CJ, Mistick EA. Kinematic control of male Allen's hummingbird wing trill over a range of flight speeds. *J Exp Biol.,* 2018, 221. https://doi.org/10.1242/JEB.173625.

[70] Gao N, Liu H. Passive dynamic stability of a hovering fruit fly: A comparison between linear and nonlinear methods. *J Biomech Sci Eng.,* 2010, 5, 591–602. https://doi.org/10.1299/jbse.5.591.

[71] Gao N, Aono H, Liu H. Perturbation analysis of 6DoF flight dynamics and passive dynamic stability of hovering fruit fly Drosophila melanogaster. *J Theor Biol.,* 2011, 270, 98–111. https://doi.org/10.1016/j.jtbi.2010.11.022.

[72] Liu H, Wang X, Nakata T, Yoshida K. Aerodynamics and flight stability of a prototype flapping micro air vehicle. *2012 ICME Int Conf Complex Med Eng C, 2012 Proc*., 2012, 657–662. https://doi.org/10.1109/ICCME.2012.6275676.

[73] Noda R, Nakata T, Liu H. Body flexion effect on the flight dynamics of a hovering hawkmoth. *J Biomech Sci Eng.,* 2014, 9, 1–11. https://doi.org/10.1299/jbse.14-00409.

[74] Vogel CR, Willden RHJ. Improving Tidal Turbine Performance Through Multi-Rotor Fence Configurations. *J Mar Sci Appl.,* 2019, 18, 17–25. https://doi.org/10.1007/s11804-019-00072-y.

[75] Kuantama E, Tarca R. Quadcopter thrust optimization with ducted-propeller. *MATEC Web Conf.,* 2017, 126, 1–4. https://doi.org/10.1051/matecconf/201712601002.

[76] Tanabe Y, Sugawara H, Sunada S, Yonezawa K, Tokutake H. Quadrotor drone hovering in ground effect. *J Robot Mechatronics,* 2021, 33, 339–347. https://doi.org/10.20965/jrm.2021.p0339.

[77] Wang J, Zhang C, Wu Z, Wharton J, Ren L. Numerical study on reduction of aerodynamic noise around an airfoil with biomimetic structures. *J Sound Vib.,* 2017, 394, 46–58. https://doi.org/10.1016/j.jsv.2016.11.021.

[78] Aamir MA, Zaheer SQ. Aeroacoustics analysis of 2D UAV wing at different flap deflections and incorporation of bio inspired aeroacoustics reduction techniques. *Proc. 2018 15th Int. Bhurban Conf. Appl. Sci. Technol. IBCAST 2018*, vol. 2018- Janua, 2018, 593–599. https://doi.org/10.1109/IBCAST.2018.8312285.

[79] Yao J, Yeo KS. A simplified dynamic model for controlled insect hovering flight and control stability analysis. *Bioinspiration and Biomimetics*, 2019, 14. https://doi.org/10.1088/1748-3190/ab2cc5.

[80] Zhu HJ, Meng XG, Sun M. Forward flight stability in a drone-fly. *Sci Rep.*, 2020, 10, 1–12. https://doi.org/10.1038/s41598-020-58762-5.

[81] Simone MCDE, Giovanni V, Ii P, Corso F, Napoli UI, Giovanni V, et al. Influence of Aerodynamics on Quadrotor Dynamics. 2015, 111–118. https://doi.org/10.13140/RG.2.1.5099.3128.

[82] Perozzi G. A toolbox for quadrotors: from aerodynamic science to control theory. To cite this version: HAL Id: hal-01696344 A toolbox for quadrotors: from aerodynamic science to control theory, 2018, 1–25.

[83] Todd C, Koujan H, Fasciani S. A Hybrid Controller for Inflight Stability and Maneuverability of an Unmanned Aerial Vehicle in Indoor Terrains. *Autom Control Syst Eng J.*, 2017, 17.

[84] Subramanian A, Yogesh SA, Sivanandan H, Giri A, Vasudevan M, Mugundhan V, et al. Effect of airfoil and solidity on performance of small scale vertical axis wind turbine using three dimensional CFD model. *Energy*, 2017, 133, 179–190. https://doi.org/10.1016/j.energy.2017.05.118.

[85] Li Y, Pan D, Zhao Q, Ma Z, Wang X. Hydrodynamic performance of an autonomous underwater glider with a pair of bioinspired hydro wings–A numerical investigation. *Ocean Eng.*, 2018, 163, 51–57. https://doi.org/10.1016/j.oceaneng.2018.05.052.

[86] Xiang J, Schluter J, Duan F. Numerical study of the tip clearance flow in miniature gas turbine compressors. *Aerosp Sci Technol.*, 2019, 93, 105352. https://doi.org/10.1016/j.ast.2019.105352.

[87] Forrester AIJ, Keane AJ. Recent advances in surrogate-based optimization. *Prog Aerosp Sci.*, 2009, 45, 50–79. https://doi.org/10.1016/j.paerosci.2008.11.001.

[88] Tatari M, Dehghan M. A method for solving partial differential equations via radial basis functions: Application to the heat equation. *Eng Anal Bound Elem.*, 2010, 34, 206–212. https://doi.org/10.1016/j.enganabound.2009.09.003.

[89] Han Z, Zhang K. Surrogate-Based Optimization. *Real-World Appl. Genet. Algorithms*, 2012. https://doi.org/10.5772/36125.

[90] Queipo N V., Haftka RT, Shyy W, Goel T, Vaidyanathan R, Kevin Tucker P. Surrogate-based analysis and optimization. *Prog Aerosp Sci.,* 2005, 41, 1–28. https://doi.org/10.1016/j.paerosci.2005.02.001.

[91] Du X, Leifsson L. Optimum aerodynamic shape design under uncertainty by utility theory and metamodeling. *Aerosp Sci Technol.,* 2019, 95, 105464. https://doi.org/10.1016/j.ast.2019.105464.

[92] Pagliuca G, Kipouros T, Savill MA. Surrogate modelling for wing planform multidisciplinary optimisation using model-based engineering. *Int J Aerosp Eng., 2019*. https://doi.org/10.1155/2019/4327481.

[93] Arias-Montaño A, Coello Coello CA, Mezura-Montes E. Multi-objective airfoil shape optimization using a multiple-surrogate approach. *2012 IEEE Congr Evol Comput, CEC 2012,* 2012, 10–15. https://doi.org/10.1109/CEC.2012.6256491.

[94] Liu F, Han ZH, Zhang Y, Song K, Song WP, Gui F, et al. Surrogate-based aerodynamic shape optimization of hypersonic flows considering transonic performance. *Aerosp Sci Technol.,* 2019, 93, 105345. https://doi.org/10.1016/j.ast.2019.105345.

[95] Tesfahunegn YA, Koziel S, Leifsson L, Bekasiewicz A. Surrogate-based airfoil design with space mapping and adjoint sensitivity. *Procedia Comput. Sci.*, vol. 51, 2015, 795–804. https://doi.org/10.1016/j.procs.2015.05.201.

[96] Leifsson L, Koziel S, Bekasiewicz A. Fast low-fidelity wing aerodynamics model for surrogate-based shape optimization. *Procedia Comput. Sci.*, vol. 29, Elsevier Masson SAS, 2014, 811–820. https://doi.org/10.1016/j.procs.2014.05.073.

[97] Introduction I. Application of Direct and Surrogate-Based Optimization. 2015, 1–20.

Chapter 2 A Biomimetic Rotor-Configuration Design for Optimal Aerodynamic Performance in Quadrotor Drone

2.1 Introduction

Insects and birds can achieve high aerodynamic performance and flight control with some optimal combination of flapping wings configuration and stroke-plane inclination [1–5] as shown in Figures 2-1a and 2-1b, which is mainly realized by time-varying wing twist and folding [6–8], elevation and tilt of stroke plane during the flight [9,10]. Moreover, insects normally enable smart flight stabilization and control in various modes of hovering and forward/maneuvering flights by means of a combination of stroke plane angle variation and adjustment of the wing kinematics comprising positional, feathering and elevation angles [2], which benefits much from increasing the lifting surface [4,11–13]. From Figures 2-1c and 2-1d, it is seen that during the middle downstroke that contributes to lift generation, the LEV (leading-edge vortex), the TV (wing tip vortex) and the shed TEV (trailing-edge vortex) totally form a downstroke vortex ring around each wing, which is beneficial to lift generation with intense downward jet stream forming the downstroke downwash [3,4,11]. Generally, the vortices are generated around the wings, whereas the wing root vortex is close to body leading to slight wing-body interaction and hence less contribute to lift production [14,15]. Thus, flying insects can realize remarked aerodynamic force production owing to few wing-wing and wing-body interactions during hovering except the clap-and-fling mechanism with large wing stroke amplitude [16]. This configuration of paired wings in flying insects is likely to produce a downwash jet effectively, with very few aerodynamic interactions between two wings, which provides some hints for our quadrotor configuration design that rotors with few interactions in between may be more effective. Besides, the wing rotation or motion accompanying wing-body morphology also have a great effect on maneuverability and stability [9,10,17,18]. Inspired by the wing kinematics of flying animals, some modification concepts can be conceived for the design of quadrotor drone (DJI phantom 3 advanced for example in Figure 1-5a) that is extensively employed for different applications [19]. Although some researches had been performed on aerodynamic performance improvement [20-23], and some creative designs had been conducted to gain better flight performance and maneuverability of quadrotor drones [24-28], the bio-inspired rotor-configuration effects on aerodynamic performance that may play a crucial role in multi-copter performance remains poorly understood. As the quadrotor drones exhibit their flight by changing the rotational speed of propellers traditionally (Figure 1-5a), while flying animals can perform exquisite control of flight with flapping and flexible wings aerodynamics (Figure 2-1a and 2-1b) of stroke-plane inclination [1,2], wings rotation or flapping wings' Euler angles asymmetry [3,9,10,17], it is potential that the quadrotor drones could be modified by the design of rotor-configuration with improving the aerodynamic performance from the bioinspiration, which may further realize the long endurance of flight, the less cost of power, and the high efficiency of drone system.

With respect to aerodynamic performance of rotor-configurations, Aleksandrov, D. and Penkov, I. conducted CFD simulations and experiments with analyzing the effect of distances between rotors on angular velocity, finding that air flows through the rotors can affect each other and optimal gap distance exists in terms of lift force production [29]. Dhwanil Shukla and Narayanan Komerath investigated the aerodynamic interactions between side-by-side rotors over a range of rotor separation and Reynolds numbers with performance measurements from high-speed Stereo Particle Image Velocimetry (SPIV) to analyze inter-rotor interactions and rotor efficiency [30]. Seokkwan, Y. *et al* studied the interactional aerodynamic performance and efficiency of multirotor systems through numerical simulations of Reynolds-averaged Navier–Stokes equations (RANS), one-equation Sqalart-Allmars (SA) turbulence model and Detached Eddy Simulation (DES) model [31]. B. Theys *et al* investigated the influences and interference effects of coaxial and overlapping propellers, as well as pusher or puller propeller configurations [32]. Lei *et al* proposed an aerodynamic model of nonplanar quadrotor with various rotor spacings and disk plane angles by CFD (computational fluid dynamics)-based simulations and experiments [33]. Duc Hung Nguyen *et al* confirmed the aerodynamic interference between tandem configuration by wind tunnel experiments [34], in terms of various unsteady aerodynamic parameters based on theoretical and experimental analyses [35]. These studies however mainly focused on some specific aspects of the rotor-configuration effect. It still remains poorly understood how the different rotor-configurations alter aerodynamic performance of multi-rotor copters associated with lift force production and FM (Figure of Merit) efficiency in terms of tip distance, height difference, and tilt angle of propellers.

In this chapter, we carry out an extensive CFD-based analysis to explore the optimal rotor-configurations in a typical multi-rotor copter, which can optimize aerodynamic performance through over a broad parameter space by combining CFD-based simulations and a novel surrogate modeling. We then demonstrate that a rotor-configuration with a large tip distance and some height difference with zero tilt angle enables optimizing both lift force production and FM efficiency compared to those in basic rotor-configuration, which coincides with the observation in insects that there almost exist no aerodynamic interaction between two wings' downwash because of downstroke vortex ring formed by the LEV, the TV and the shed TEV around each wing (Figures 2-1c and 2-1d), and thus could offer a novel optimal design for multirotor UAVs.

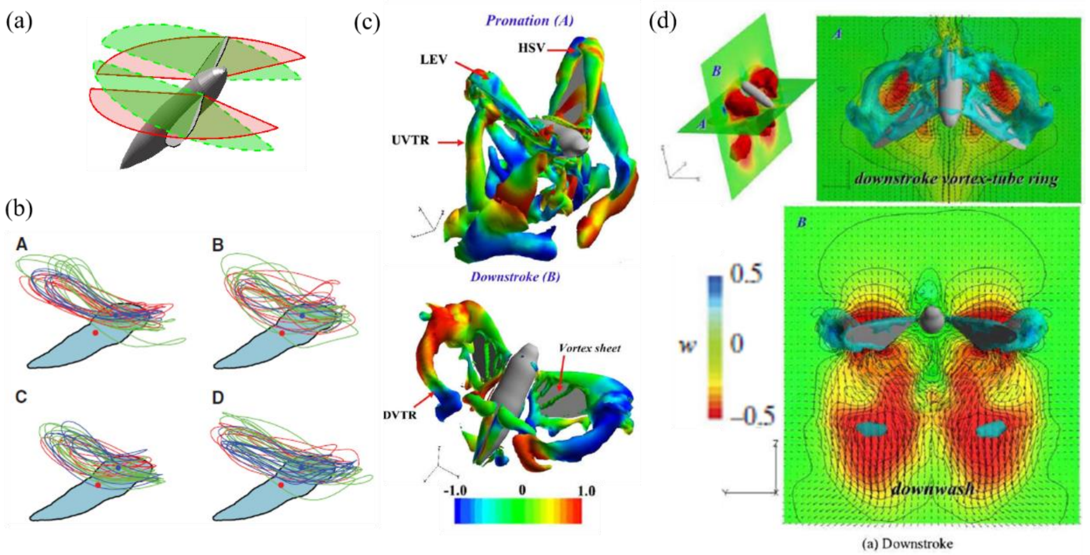

Figure 2-1 Illustration of flapping wing flight. (a) Stroke-plane inclination of a hawkmoth; (b) measured wing tip trajectories during pitch maneuver of hawkmoths [1]; (c) near- and far-field vortical flow structures about hawkmoth hovering [3,4,11]; (d) wake topology and downwash of hawkmoth hovering [3,4,11].

2.2 Methods and materials

2.2.1 Geometric models of single propeller and multi-propeller

2.2.1.1 Single propeller geometry

The 3D geometry of a single propeller as utilized in our previous study with reconstruction by digitizing from a laser scanner (Laser Scan Arm V2, FARO Technologies Inc.) [36] comes from the quadrotor drone of DJI phantom 3 advanced (DJI Ltd.) (Figure 1-5a), and is adopted in the single propeller CFD model which is introduced as a baseline for comparison of the aerodynamic performance between multi-propeller and the isolated propeller [29–31]; the basic multi-propeller model was also employed as a baseline rotor-configuration for exploring the rotor-configuration effects on aerodynamic performance with comparisons of different multi-propeller configurations.

2.2.1.2 Multi-propeller geometry

The geometry of a base multi-propeller (rotor) model as shown in Figure 1-5b is generated by SolidWorks 2013, where one propeller pair rotates clockwise and the other anti-clockwise with the same geometry (Figure 1-5a). The nondimensional configuration parameters of the model are listed in Table 2-1.

In order to explore the aerodynamic interactions among propellers in terms of rotor-configurations, we further define various rotor-configurations by introducing three key parameters with considering the six-degree of freedom about the rotor-configuration system: a tip distance (d) between left (P2&P3) and right propellers (P1&P4), a height difference (h) between two different pairs of propellers, and a tilt angle (TA) of propellers, which totally result in six parameters of $d_{14-23,\phi}$, $d_{14-23,lb}$, $h_{u24-l13}$, $h_{u23-l14}$, α and β, as shown in Figures 2-2 to 2-4. The parameter $d_{14-23,\phi}$ (Figure 2-2a) defines the tip distance between propellers P1&P4 and P2&P3 being stretched in diagonal direction with a constant inclination angle of ϕ. Here the maximum $ld_m = ld_0 + 2\mathrm{R}$ corresponds to the maximum $d_{m_{14-23,\phi}} = 1.54\mathrm{R}$, which leads the design space of $d_{14-23,\phi}$ over a range of [0.1, 1.54]. The parameter $d_{14-23,lb}$ (Figure 2-2b) denotes the tip distance of propellers P1&P4 and P2&P3 in longitudinal direction while keeping the parameter lb unchanged, which has the same range of design space with $d_{14-23,\phi}$ of [0.1, 1.54]. The parameter $h_{u24-l13}$ (Figure 2-3a) represents the height difference between propellers P1&P3 and P2&P4 through adjusting their relative height whereas the parameter $h_{u23-l14}$ (Figure 2-3b) is for the height difference between propellers P2&P3 and P1&P4, where the maximum height difference is also set to be $h_m = h_0 + 2\mathrm{R}$, which makes the design space of $h_{u24-l13}$ and $h_{u23-l14}$ vary over a range of [0, 2]. The parameter α (Figure 2-4a) corresponds to the tilt angle of propellers through rotating propellers P2&P3 around axes, y_2 and y_3, while rotating propellers P1&P4 around axes, y_1 and y_4 in rotor-fixed reference system simultaneously. Furthermore, a positive α is defined to be identical to an anticlockwise rotation of P2&P3 while a clockwise rotation has a negative α; the parameter β (Figure 2-4b) denotes the tilt angle with each propeller rotated around axes, x_i and y_i in rotor-fixed reference frame equally, being negative when propellers tilt towards to the center of rotor-configuration but positive vice versus. In Ref. [33], it was pointed out that the aerodynamic performance could be improved over a range of 0° - 50° with the designed tilt angle. With consideration of some lift force loss and interference between propeller and fuselage, the design space of tilt angle in this study is set to be $[-20°, 20°]$ for both α and β. In addition, a uniform step of 0.2 is set for both tip distance and height difference, while 5° for the tilt angle; all the parameters employed in design space are summarized in Table 2-2. These parameters will be selected and grouped to form various rotor-configurations to explore the optimal aerodynamic performances based on the CFD simulations (section 2.3.1) and a surrogate model-based optimization algorithm (section 2.3.2).

Table 2-1 Dimensions of the base model about multi-propeller

la_0/R	lb_0/R	ld_0/R	ϕ_0	**Tip distance (d_0/R)**	**Height difference (h_0/R)**	**Tilt angle (TA_0)**
2.1	2.025	2.917	44°	0.1	0	0°

Subscript "0" means the original value in base model.

Table 2-2 Cases of various rotor-configurations about multi-propeller model

$i = d_{14-23,\phi}/\mathrm{R}$	0.3	0.5	0.7	0.9	1.1	1.3	1.5	1.54		
$i = d_{14-23,lb}/\mathrm{R}$	0.3	0.5	0.7	0.9	1.1	1.3	1.5	1.54		
$i = h_{u24-l13}/\mathrm{R}$	0.2	0.4	0.6	0.8	1.0	1.2	1.4	1.6	1.8	2.0
$i = h_{u23-l14}/\mathrm{R}$	0.2	0.4	0.6	0.8	1.0	1.2	1.4	1.6	1.8	2.0
α	−20°	−15°	−10°	−5°	5°	10°	15°	20°		
β	−20°	−15°	−10°	−5°	5°	10°	15°	20°		

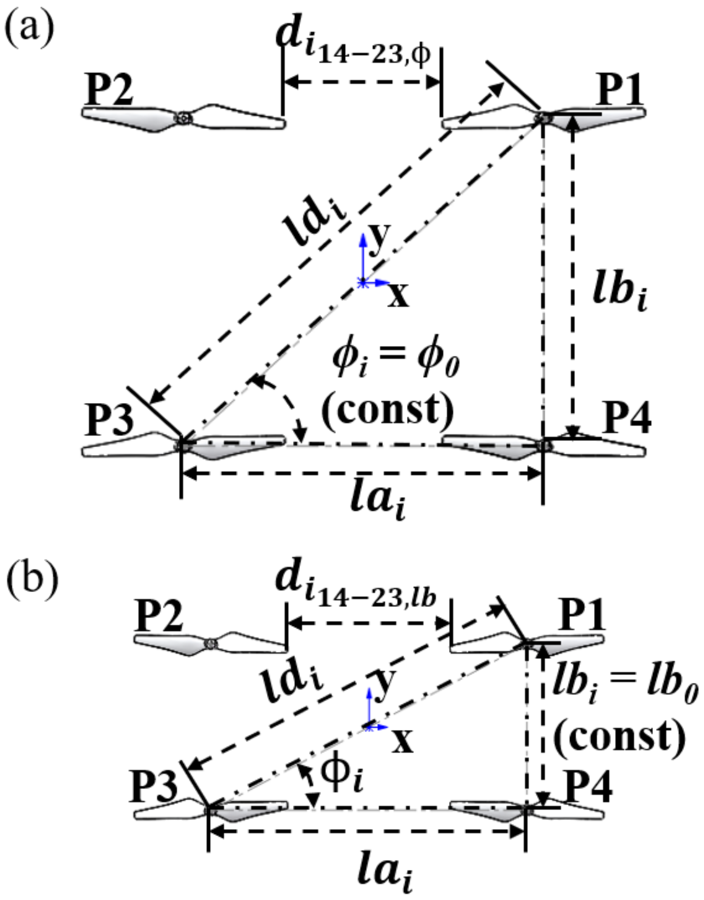

Figure 2-2 Definitions of various rotor-configurations and parameters regarding tip distance. (a) Parameter $d_{14-23,\phi}$ (top), $i = d_{14-23,\phi}/\mathrm{R}$; (b) parameter $d_{14-23,lb}$ (top), $i = d_{14-23,lb}/\mathrm{R}$.

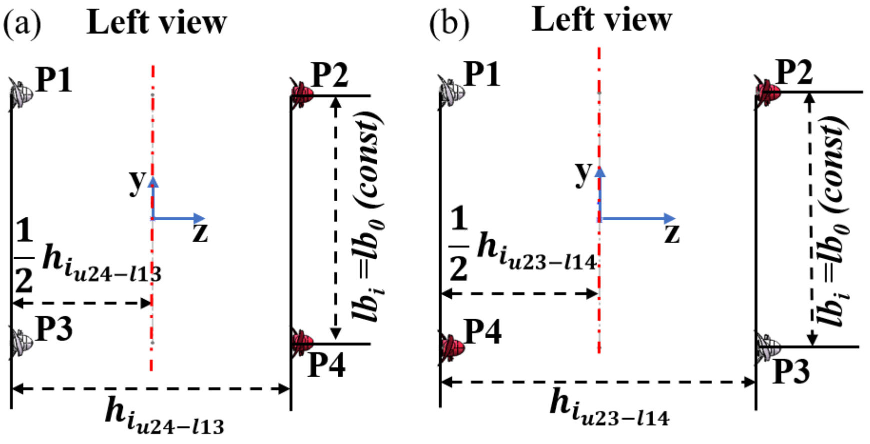

Figure 2-3 Definitions of various rotor-configurations and parameters regarding height difference. (a) Parameter $h_{u24-l13}$ (left), $i = h_{u24-l13}/\mathrm{R}$ and (b) parameter $h_{u23-l14}$ (left), $i = h_{u23-l14}/\mathrm{R}$ with top view same as Figure 1-5b.

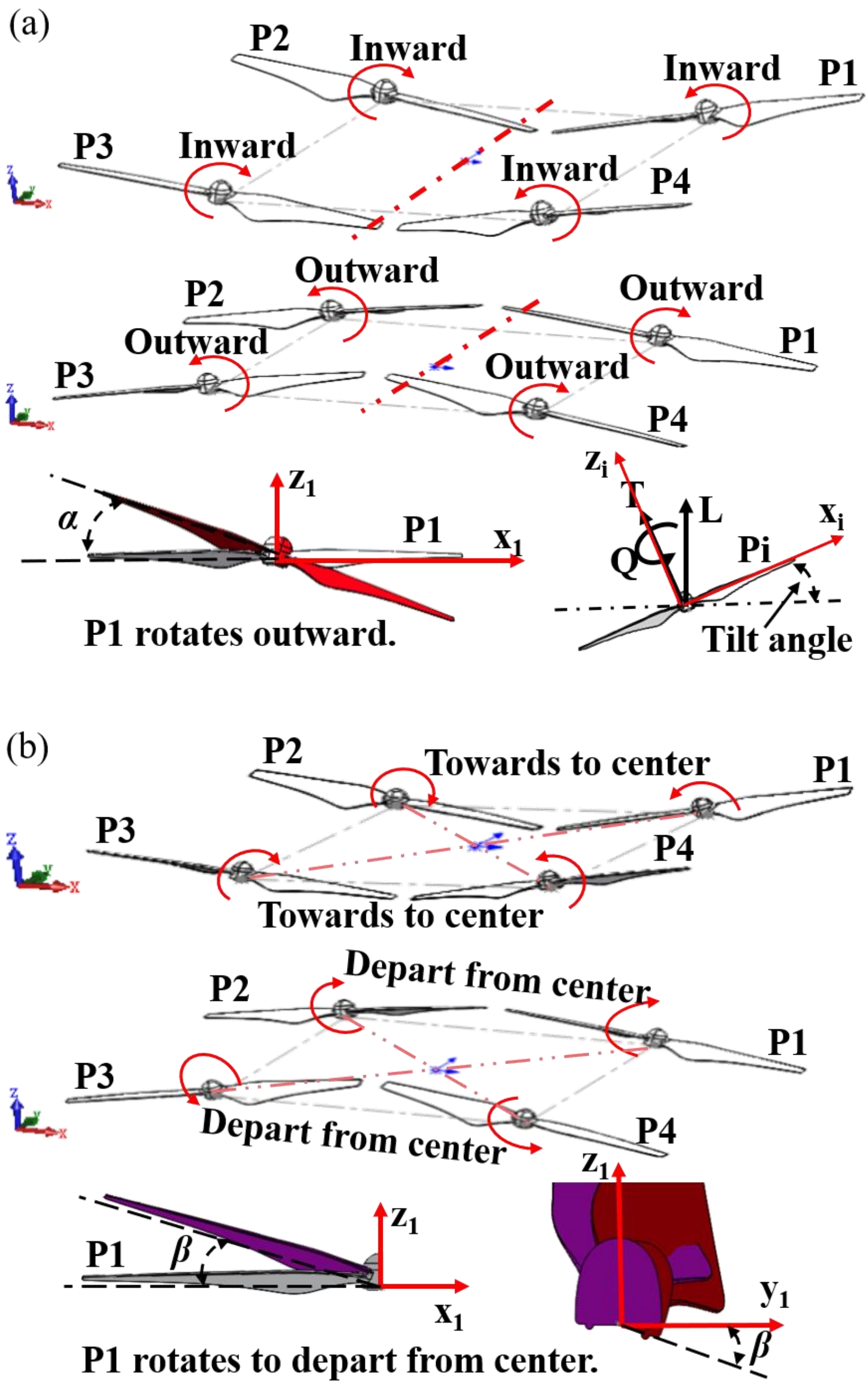

Figure 2-4 Definitions of various rotor-configurations and parameters regarding tilt angle. (a) Parameter α (negative when tilting inward but positive outward); (b) parameter β (being generated through rotating propeller around y_i firstly and around x_i with same angle secondly).

2.2.2 CFD modeling

2.2.2.1 Single propeller modeling

Aerodynamic performance associated with single propeller was investigated based on CFD simulations with commercial software, ANSYS CFX 14.5 (ANSYS Inc). Given the rotational speed, 5400rpm, of propellers in Phantom 3 advanced [36], the Reynolds number of a single propeller [30] was calculated to be

$$R_e = \frac{\rho U l}{\mu} = 7.4\text{x}10^4, \tag{2-1}$$

where $\rho = 1.2kg/m^3$ is air density, $U = R\omega = 2\pi \mathrm{R}n$ is tip velocity (the rotational angular velocity, ω, and the rotational speed, n), $l = 0.162m$ is the chord length at 75%R of propeller, and $\mu = 1.79 \times 10^{-5} Pa \cdot s$ is air viscosity.

The RANS modeling of turbulent flow with the SST (Shear Stress Transport) turbulence model was employed with a “high resolution” mode for the simulation of single propeller model (Figures 2-5a to 2-5c) with a cross-section of Figure 2-5d. Follow Refs. [36,37], the inflation layer meshes were generated with seven layers surrounding the rotor surface to ensure high resolution of the boundary layer adjacent to walls while being clustered at wingtip, leading edge, and trailing edge, resulting in the total meshes of approximately 16 million for the single propeller CFD model. At the interface between rotating and static region, a “Frozen Rotor (FR)” model was adopted to give the rotor an appointed constant rotating speed in order to “freeze” the relative movements between the two frames so as to achieve the convergence to a stable state. At outside boundary of the spherical surface, open (free-stream boundary) condition was imposed with 0 Pa pressure, as listed in Table 2-3.

Aerodynamic performance of single propeller can be evaluated with lift force coefficient, C_L, and figure of merit, *FM* [36,38,39], defined as

$$C_\mathrm{L} = \frac{L}{0.5\rho U^2 S_2}, \tag{2-2}$$

where L is the lift force of a single propeller, ρ is the air density ($\rho = 1.2kg/m^3$), U is the speed of wingtip, S_2 is the second moment of wing area ($S_2 = 9.5 \times 10^{-4} m^4$), respectively.

$$FM = \frac{P_{RF}}{P_{CFD}}, \tag{2-3}$$

where P_{RF} denotes the minimum power for generating lift force based on numerical results and Rankin-Froude momentum theory; P_{CFD} is defined as product of torque around rotational axis, Q, and rotational angular velocity, ω, such as:

$$P_{RF} = L\sqrt{\frac{L}{2\rho A_0}},\ P_{CFD} = Q \cdot \omega. \tag{2-4}$$

where L denotes the lift force, A_0 the actuator disk's area defined by radius, R, of the propeller, and ρ the air density, respectively. Furthermore, it is better for efficiency of drone when the value of FM is closer to 1.0.

2.2.2.2 Multi-propeller modeling

Flow structures and aerodynamic performances associated with hovering quadrotor drone were also studied in terms of rotor-configuration effects based on CFD simulations with commercial software, ANSYS CFX 14.5 (ANSYS Inc). The numerical settings and boundary conditions of the multirotor model in CFD simulations are the same as those in the single propeller model, with total meshes of approximately 55 million, as shown in Figures 2-5e to 2-5h and Table 2-3.

In addition, Equations (2-2) – (2-4) are employed for the evaluation of aerodynamic performances associated with average lift force coefficient, $\overline{C_{\mathrm{L}}}$ and average figure of merit, $\overline{FM}$ in multirotor models in a manner of various rotor-configurations, where the lift force, L, P_{RF}, P_{CFD}, and torque, Q, should be substituted by the average lift force of multirotor ($\bar{L}$), $\overline{P_{RF}}$, $\overline{P_{CFD}}$, and average torque of multirotor ($\bar{Q}$) in theses equations. In addition, average thrust coefficient, $\overline{C_T}$ is derived from average thrust of multirotor ($\bar{T}$) as a substitution of L in Eq. (2-2), and $\overline{FM}$ is calculated via the average thrust ($\bar{T}$) as a substitution of L in Eqs. (2-3) – (2-4) with maintaining the value A_0 [38] when tilt angle exists in the cases of different quadrotor configurations.

2.2.3 Rotor-configuration-based optimization of aerodynamic performance

As a series of CFD-based simulations of 52 cases (listed in Table 2-2) with different non-ducted rotor-configurations associated with tip distance, height difference and tilt angle were performed to investigate the effect of non-ducted rotor-configurations on aerodynamic performance, it was indicated that the optimal non-ducted rotor-configuration will be a configuration of fixed maximal tip distance but uncertain height difference and tilt angle. Thus, in the procedure of optimization for non-ducted rotor-configuration for the three parameters associated with tip distance, height difference, and tilt angle, we constructed a series of CFD-based cases (45 cases in total, illustrated in section 2.3.2.1), applying a surrogate model with combination of the CFD models to explore an optimal rotor-configuration in terms of average lift coefficient ($\overline{C_{\mathrm{L}}}$), average thrust coefficient ($\overline{C_T}$) and equivalent average figure of merit ($\overline{FM}$) in a parametric space of these three parameters associated with tip distance, height difference, and tilt angle.

As a common method to predict the outcome of a parametric space in a manner of optimization [40–42], the surrogate modeling of Radial basis functions (RBFs) model method [43–46] was adopted. Three steps were included in the process of optimization for non-ducted rotor-configuration, which are: (1) specifying a design of CFD-based numerical experiments including 45 Points *in toto* in a parametric space comprising those three parameters; (2) CFD simulations at design points; and (3) constructing a surrogate model based on CFD simulations to generate a continuous output ($\overline{C_\mathrm{L}}$ ($\overline{C_T}$) and $\overline{FM}$) over the entire design space.

The approximation of optimal aerodynamic performance via RBFs approach in terms of $\overline{C_\mathrm{L}}$ ($\overline{C_T}$), $\overline{FM}$ as an unknown function *f(x)* at an untried point x is formally derived from a linear combination of radial basis functions, which is defined as [43–46]

$$f(x) = \sum_{i=1}^{n} w_i \varphi(r), \tag{2-5}$$

where w_i is the i-th weight coefficient, and $\varphi(r) = \varphi(\|x^i - x\|)$ is the basic function determined by the Euclidean distance between the prescribed observed point x^i and untried point x. In order to determine the weight coefficient w_i, a series of interpolation points of x^j that have known results from CFD simulations were introduced to substitute the untried points of x, where all the interpolation points should satisfy:

$$f(x^j) = \sum_{i=1}^{n} w_i \varphi(r) = \sum_{i=1}^{n} w_i \varphi(\|x^i - x^j\|) = y^j, \text{j=1, 2, …, n.} \tag{2-6}$$

where x^j and y^j denotes the interpolation point, and the result at the corresponding interpolation point, respectively. Thus, with the known observed points and interpolation points, the weight coefficient w_i can be determined subsequently. For sake of determining the locations of interpolation points in the design space, DoE (Design of Experiments) method in terms of Uniform Design (UD) [43] was employed to maximize the amount of information obtained from a limited number of sample discrete points, i.e., CFD simulation-based $\overline{C_\mathrm{L}}$ ($\overline{C_T}$), $\overline{FM}$. Nine interpolation points (n = 9) were employed based on the parametric space virtually through trial-and-error, which is verified to be effective enough to provide a reasonable approximation. Moreover, the optimal observed points were determined in the vicinity of interpolation points by Random selection.

The basic function of IMQ (Inverse Multiquadric) function was selected in a manner of trial-and-error from multiple options of basic function (as listed in Table 2-4) in RBFs model [43–46] and utilized at all untried and test points, corresponding to those based on CFD simulations, because it was confirmed capable of giving reasonable results on the approximation of $\overline{C_{\mathrm{L}}}$, $\overline{FM}$ with least relative error, which is defined as

$$\varphi(r) = \frac{1}{\sqrt{r^2+c^2}}, 0 < c < 4. \tag{2-7}$$

The weight coefficient w_i was determined by adjusting the coefficient, c, in the basic function of $\varphi(r)$ through solving the Eq. (2-5) based on the information at interpolated and observed points. To estimate the numerical errors between surrogate modeling and CFD simulations, three variables ($\bar{e}$, R^2 and σ_e) were introduced at test points, in which an average relative error ($\bar{e}$) is defined as

$$\bar{e} = \frac{1}{n_t}\sum_{i=1}^{n_t} e^i = \frac{1}{n_t}\sum_{i=1}^{n_t} \left\| \frac{\widehat{y^i} - y^i}{y^i} \right\|, \tag{2-8}$$

where n_t is the number of test points (n_t = 45); y^i is the true value (came from the results of CFX calculations), and $\widehat{y^i}$ is the prediction of surrogate modeling at the i-th test point, respectively.

The R-squared (R^2) is defined as

$$R^2 = 1 - \frac{\sum_{i=1}^{n_t}(y^i - \widehat{y^i})^2}{\sum_{i=1}^{n_t}(y^i - \bar{y})^2}, \tag{2-9}$$

where $\bar{y}$ denotes the average of true value based on CFD simulations. And the root mean squared error (σ_e) is defined as

$$\sigma_e = \sqrt{\frac{1}{n_t}\sum_{i=1}^{n_t}(e^i)^2}. \tag{2-10}$$

Convergence criteria are defined as $\bar{e} < 0.005$, $R^2 > 0.95$, and $\sigma_e < 0.005$ for the non-ducted rotor-configuration optimization. An inner iteration is designed to examine the optimal variables with the coefficient (c) over a predetermined range [43–46], which is conducted as described in flow chart of the optimization procedure (Figure 2-6).

Table 2-3 Numerical settings and boundary conditions of CFD model for rotor-configuration

	Single propeller model	**Multi-propeller model**
Simulation type	Steady	Steady
Turbulence model	Shear stress transport (SST)	Shear stress transport (SST)
Open boundary	Free-outflow with 0 Pa pressure	Free-outflow with 0 Pa pressure
Wall boundary	No-slip, smooth wall	No-slip, smooth wall
Rotation region's domain interface	Frozen rotor	Frozen rotor
Rotational speed (rpm)	5400	5400
Mesh elements number ($\boldsymbol{N_m}$)	Approx. 16 million	Approx. 55 million

Table 2-4 Other common functions used in RBFs model method except the IMQ function.

Basic functions	**Formulations**
Power (PW)	$\varphi(r) = r^c, 1 \leq c \leq 3$
Thin Plate Spline (TPS)	$\varphi(r) = r^2 \ln(cr), 0 < c < 3$
Gaussian (GS)	$\varphi(r) = e^{-cr^2}, 0 < c < 10$
Multiquadric (MQ)	$\varphi(r) = \sqrt{r^2 + c^2}, 0 < c < 4$

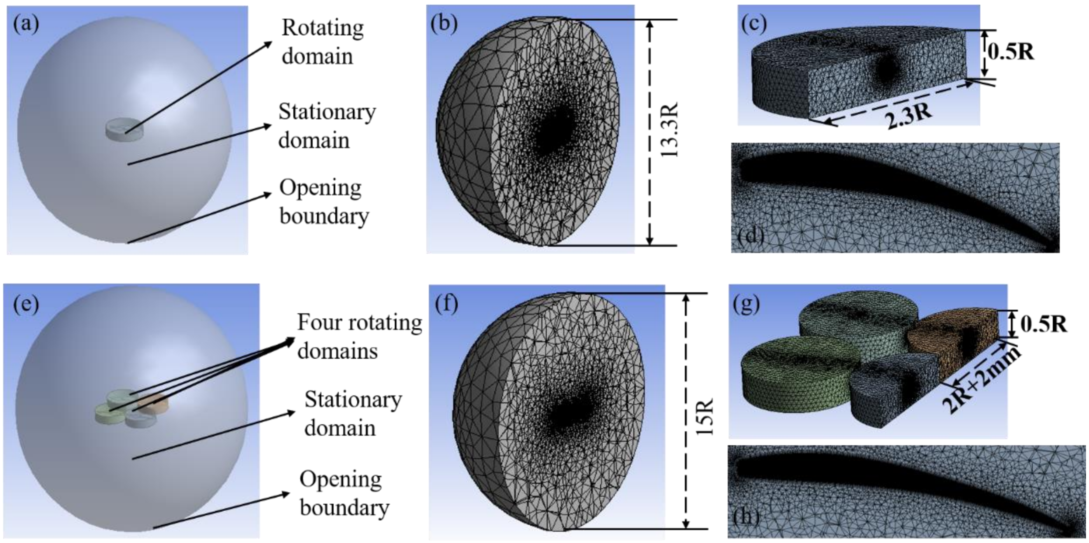

Figure 2-5 Grid systems, boundary conditions, mesh systems and meshes at a cross-section of 80%R in CFD simulations for the rotor-configuration. (a-d) Single propeller model; (e-h) multi-propeller model.

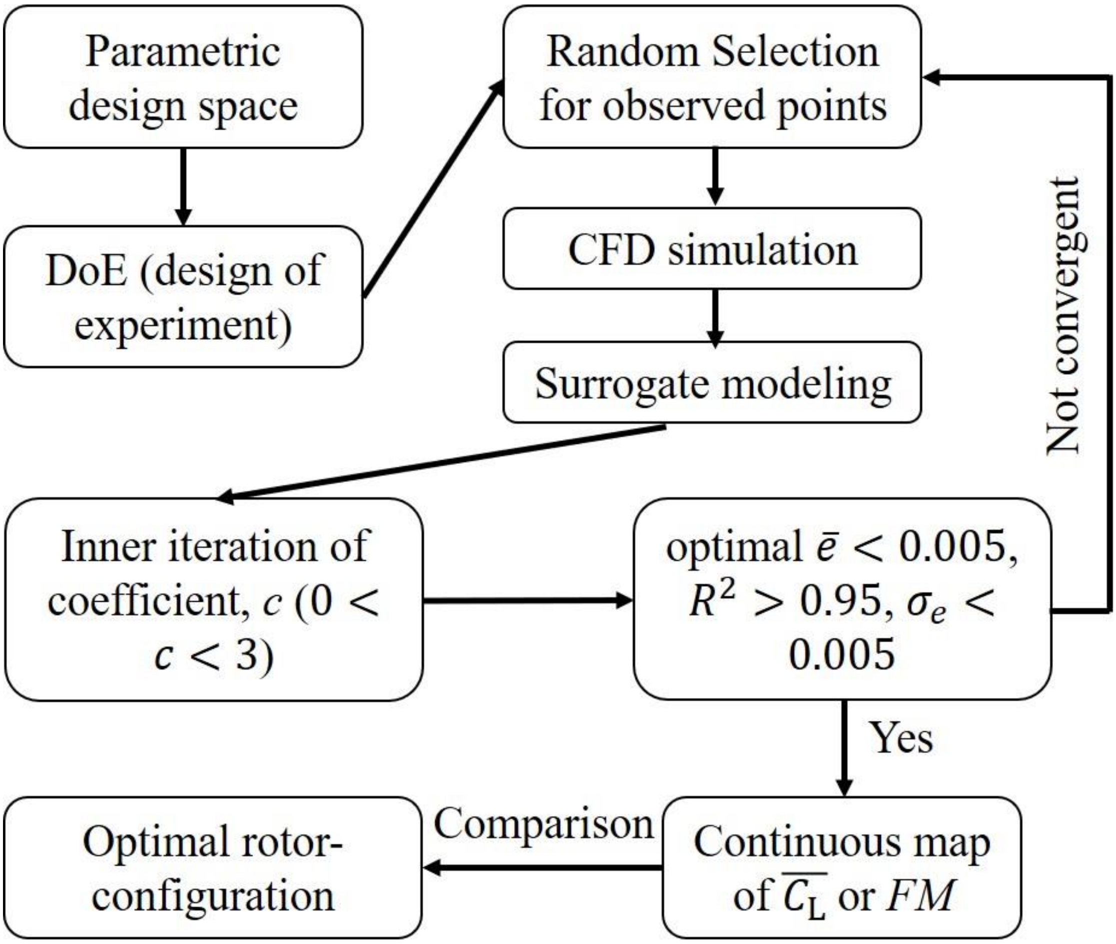

Figure 2-6 Flow chart of CFD-and surrogate model-based optimization analysis for rotor-configuration.

2.3 Results and discussions

2.3.1 Verification and validation

Verification was conducted in a manner of self-consistency on mesh independency [37]. The minimum grid spacing adjacent to wall (propeller) surface, δ_m [37], is controlled by $\delta_m \approx 0.1l/\sqrt{R_e}$, where Reynold number, $R_e = 7.4 \times 10^4$, chord length, l = 0.0162m at 75%R, resulting in a minimum spacing among grids of 0.015mm. We set a baseline case of single propeller model (SP-1) with 11 million meshes as used in our previous study [36], and two fine-mesh cases including 16 million meshes (SP-2) and 23 million meshes (SP-3), resulting in different computed C_L and FM of single propeller as shown in Figure 2-7a, all in excellent agreement with those in Ref. [36] (SP). Thus, the data of SP was utilized in the following for single propeller model. The mesh-dependency was further conducted associated with basic quadrotor-configuration model (Figure 1-5b), with four mesh systems including BMP-1 (basic multi-propeller - 1) of 26 million meshes, BMP-2 of 39 million meshes, BMP-3 of 47 million meshes and BMP-4 of 55 million meshes, respectively. Comparisons of computed $\overline{C_L}$ and $\overline{FM}$ (Fig. 2-7b) further confirmed the marginal differences among the four cases, the BMP-4 was thus selected for all the CFD simulations of quadrotor configuration model. Note that all the simulations associated with mesh-dependency were carried out to satisfy the criterion of numerical convergence so that the maximum residual of pressure was less than 5×10^{-5} and the iteration steps was taken more than 3000.

Furthermore, the CFD simulations were validated through comparisons with experiment data [34] under same conditions, in terms of relation in hover state and the interference effect of tandem rotor during forward flight (α = –5°, V = 6 $m \cdot s^{-1}$, $l/$R = 2.83). As shown in Figure 2-8, the CFD results are well consistent with the measurements while indicating that thrust (T) increases in a linear manner with increasing the square of angular velocity (ω^2), and thrust coefficient of rear rotor are obviously lower than that of front rotor during forward flight. Note that as also observed in previous studies [29-31,33], the average lift force of quadrotor configuration model is less than that of isolated propeller model, indicating that there exist propeller-propeller aerodynamic interactions, and thus some optimal configuration of propellers could maximize the aerodynamic performances of lift force production and FM efficiency.

2.3.2 Aerodynamic performance of single propeller effect

The effects of tip distance, height difference and tilt angle on $\overline{C_\mathrm{L}}$ and $\overline{FM}$ of different quadrotor configurations are investigated in terms of the parameters $d_{14-23,\phi}$, $d_{14-23,lb}$, $h_{u24-l13}$, $h_{u23-l14}$, α and β as depicted in Figures 2-2 to 2-4. Figure 2-9a shows that the $\overline{C_\mathrm{L}}$ increases with increasing nondimensionalized parameters $d_{14-23,\phi}/$R and $d_{14-23,lb}/$R, which is particularly remarkable with a notable increase rate of 7.0% associated with $d_{14-23,\phi}/$R (red line) compared to that of basic quadrotor configuration at $d/$R = 1.54, less than the magnitude of single propeller. Comparatively, a merely 2.0% increase rate as maxima is observed with increasing $d_{14-23,lb}/$R (blue line). Same trend is observed in $\overline{FM}$, which increases with increasing nondimensionalized parameters $d_{14-23,\phi}/$R and $d_{14-23,lb}/$R, again being significant with an increase rate of 10.4% associated with $d_{14-23,\phi}/$R (magenta line) while 2.9% for $d_{14-23,lb}/$R (green line), compared to those of basic quadrotor configuration at $d/$R = 1.54. Figure 2-9b shows that the $\overline{C_\mathrm{L}}$ increases with increasing the nondimensionalized parameters $h_{u24-l13}/\mathrm{R}$ and $h_{u23-l14}/\mathrm{R}$, which is distinctly notable accompanying a remarked increase rate of 4.3% associated with $h_{u24-l13}/\mathrm{R}$ (red line) compared to that of basic quadrotor configuration when h/R = 2.0. Comparatively, a 2.1% increase rate as maxima is observed with increasing $h_{u23-l14}/\mathrm{R}$ (blue line). Same trend is observed in $\overline{FM}$, which increases with increasing nondimensionalized parameters $h_{u24-l13}/\mathrm{R}$ and $h_{u23-l14}/\mathrm{R}$, again being remarkable with an increase rate of 8.4% associated with $h_{u24-l13}/\mathrm{R}$ (magenta line) while 3.1% for $h_{u23-l14}/\mathrm{R}$ (green line), compared to those of basic quadrotor configuration at h/R = 2.0. Figure 2-9c shows that $\overline{C_T}$ displays remarked increase rates of 0.7% and 1.4% compared to that of basic quadrotor configuration when α (magenta line) is –20° and 20°, respectively. Comparatively, the increase rates are –3.1% and –6.6% about β (cyan line) at –20° and 20°, respectively. Meanwhile, due to the tilt angle, $\overline{C_\mathrm{L}}$ both decreases with changing α and β, being remarked with increase rates of –5.4% and –4.7% compared to that of basic quadrotor configuration when α (red line) is –20° and 20°, respectively. Comparatively, the increase rates are –14.0% and –18.0% about β (blue line) at –20° and 20°, respectively. Same trend is observed in $\overline{FM}$ as illustrated in Figure 2-9d, with the increase rates of 1.5% and 1.7% at α (red line) of –20° and 20°, and of 2.7% and –4.1% regarding β (blue line) at –20° and 20°, respectively. Therefore, it is obvious that proper adjustments of parameters $d_{14-23,\phi}$, $h_{u24-l13}$, and α with positive value associated with tip distance effect, height difference effect, and tilt angle effect are effective in improving aerodynamic performances, which were thus employed in our further optimization procedure.

According to the momentum theory, the rotating rotor induces a downward air flow through the rotor blade, the so-called induced flow (downwash), which is most pronounced at hover. And based on the blade element theory, the wake of a single-rotor blade in hover is affected by the tip vortex and inner vortex sheet essentially. The tip vortex, the inner vortex sheet and the downward moving wake contribute to the lift force generation of the single propeller [33,34,47], as illustrated in Figure 2-10a. With respect to the tip distance effect, the downwashes induced by each propeller that form a twin downwash-jet separated with each other are likely to improve the lift force production at a large tip distance. Comparatively, the $d_{14-23,\phi}$ based aerodynamic interactions play a more important role in aerodynamic performance than that of $d_{14-23,lb}$ since separated propellers with less interactions can work more effectively [30]. With respect to the height difference effect, the downwashes from upper propellers increase the induced flow of lower propellers, which is beneficial to lift force production of lower propellers, although this effect turns to be weaken at larger height differences [33,34,47].

Furthermore, the $h_{u24-l13}$ based aerodynamic interactions have better performance because of no interaction between tip vortices interactions in the same plane between propellers P2&P3 and propellers P1&P4. The tilt angle effect also attributes to the impact of induced flow variation [33], although the interactions owing to tilt angle α alter the induced velocity and wake velocity, it leads to solely slight improvement on thrust generation. In addition, any change of β relative to the basic quadrotor configuration will lead to a reduction of $\overline{C_T}$ probably due to the alteration in angle of attack (AoA) (as shown in Figure 2-10b) [34,47]. These results are supported by the visualized flow structures associated with various quadrotor configurations at cross-sections of y/R =1.013, and 1.707, the planes that the centers of propellers P1 & P2 located in as illustrated in Figure 2-11.

2.3.3 Optimization of aerodynamic performances via CFD-and surrogate model-fusion

As pointed out in section 2.3.2, the tip distance $d_{14-23,\phi}$ has most significant effect on improving aerodynamic performances and the height difference $h_{u24-l13}$ has secondary significant effect on aerodynamic performances improvement, whereas the tilt angle α has least influence on improving aerodynamic performances. Thus, the maximum $d_{14-23,\phi}$/R = 1.54 is fixed to be constant for the optimization procedure of quadrotor-configuration. The optimization procedure based on the design space of three parameters combination associated with fixed tip distance $d_{m_{14-23,\phi}}$ (d_m), height difference $h_{u24-l13}$ (h) and tilt angle α is defined as:

$$Max.\ \overline{C_L}\ (\overline{C_T})\ \text{or}\ \overline{FM},\ \text{s. t.}\ 0 \le h/\text{R} \le 2.0, 0 \le \alpha \le 20°. \tag{2-11}$$

2.3.3.1 Optimization via CFD simulation

The numerical simulations with CFX 14.5 have the same setting with basic quadrotor-configuration CFD model, and the rotor-configuration with d_m/R = 1.54, h = 0, and α = 0 which is called large tip distance configuration (LT-config., $hA_{0,0}$) is designated as the baseline in the optimization procedure. Through an extensive study of mesh-dependency associated with the LT-config. model, a mesh system with 47 million meshes ($N_m/N_{m,BMP}$ =0.855) was confirmed to be able to ensure a reasonable numerical accuracy. The total cases utilized in the CFD-based optimization are 45 based on the design space in Eq. (2-11), which comprises 25 cases selected uniformly and other 20 cases chosen randomly, as shown in Table 2-5.

Figures 2-12a to 2-12c show that the $\overline{C_T}$, $\overline{C_{\mathrm{L}}}$ and $\overline{FM}$ increase with increasing height difference at $\alpha = 0$, but change slightly when some tilt angle exists, capable of achieving the maximum at $d_m/\mathrm{R} = 1.54$, $h/\mathrm{R} = 2.0$, and $\alpha = 0$. Figure 2-12b further shows that the $\overline{C_{\mathrm{L}}}$ decreases with increasing tilt angle at some fixed height difference. Note that unlike the tilt angle effect observed in the basic rotor-configuration model (Figure 2-9c), $\overline{C_T}$ turns to be almost stable when the tilt angle α is greater than 5° independent of height difference, indicating that the aerodynamic interactions are negligible at large tip distance. Moreover, the maximum increase rate of $\overline{C_{\mathrm{L}}}$ ($\overline{C_T}$) is 1.6% compared to that of LT-configuration (Figures 2-12a and 2-12b), and 8.8% compared to that of basic quadrotor configuration at $d_m/\mathrm{R} = 1.54$, $h/\mathrm{R} = 2.0$, and $\alpha = 0$, respectively. Correspondently, the maximum increase rate of $\overline{FM}$ is 2.8% compared to that of LT-configuration (Figure 2-12c), and 12.9% compared to that of basic quadrotor configuration. As a result, the optimal quadrotor configuration can be achieved with a combination of $d_m/\mathrm{R} = 1.54$, $h/\mathrm{R} = 2.0$, and $\alpha = 0$.

2.3.3.2 Optimization via CFD-and surrogate model-fusion

Here we determine the maximum $\overline{C_T}$ and $\overline{C_{\mathrm{L}}}$ of the optimization procedure in surrogate modeling because $\overline{FM}$ shows similar trend with $\overline{C_T}$. Figures 2-13a and 2-13d show the interpolation points and optimal observed points in the surrogate modeling. The boundary of observed points was limited in the vicinity of interpolation points depicted by the red dashed frame. The surrogate modeling-based results with inverse multiquadric (IMQ) function in RBFs model are illustrated in Figures 2-13b and 2-13e, where the green cross markers represent the maxima $\overline{C_T}$ and $\overline{C_{\mathrm{L}}}$ of surrogate modeling, and the red cross markers for the maxima $\overline{C_T}$ and $\overline{C_{\mathrm{L}}}$ of CFD simulation. It gives an estimation of the maximum $\overline{C_{\mathrm{L}}}$ with an increase rate of 10.01% compared to that of Basic-configuration (BMP) and 2.81% compared to that of LT-configuration (LTMP), respectively, as listed in Table 2-6. The surrogate modeling indicates that the optimal quadrotor configuration is assigned at $d_m/\mathrm{R} = 1.54$, $h/\mathrm{R} = 0.6$, and $\alpha = 0$ based on $\overline{C_{\mathrm{L}}}$, while it is assigned at $d_m/\mathrm{R} = 1.54$, $h/\mathrm{R} = 1.56$, and $\alpha = 0$ in the view of $\overline{C_T}$, which are close to the CFD-based result. Besides, it also shows that the $\overline{C_{\mathrm{L}}}$ has slight loss ($\leq$ 2%) with retaining $\overline{C_T}$ within the range of tilt angle less than 10°, which is beneficial to maneuver design for quadrotors. In summary, our results thus point out a novel biomimetic design of optimal rotor-configuration for multirotor UAVs, which has a large tip distance and some height difference with zero tilt angle, resulting from the least interference of downwash-jet among adjacent propellers and the maximum positive interaction among upper and lower propellers on conditions of this optimal rotor-configuration in quadrotor drone.

Table 2-5 Calculation cases (45 points in total) utilized in CFD of optimization procedure regarding rotor-configuration

	Uniform selection (h/R)					**Random selection (h/R)**			
$\boldsymbol{\alpha = 0°}$	0	0.5	1.0	1.5	2.0	0.2	0.6	1.2	1.6
$\boldsymbol{\alpha = 5°}$	0	0.5	1.0	1.5	2.0	0.2	0.6	1.2	1.6
$\boldsymbol{\alpha = 10°}$	0	0.5	1.0	1.5	2.0	0.2	0.6	1.2	1.6
$\boldsymbol{\alpha = 15°}$	0	0.5	1.0	1.5	2.0	0.2	0.6	1.2	1.6
$\boldsymbol{\alpha = 20°}$	0	0.5	1.0	1.5	2.0	0.2	0.6	1.2	1.6

Table 2-6 Comparisons between CFD and surrogate modeling regarding rotor-configuration

	CFD	**Surrogate modeling**
Maximum $\overline{\boldsymbol{C}_{\mathbf{L}}}$ compared with LTMP	1.43%	2.81%
Maximum $\overline{\boldsymbol{C}_{\mathbf{L}}}$ compared with BMP	8.5%	10.01%
Optimal position	$h/\mathrm{R} = 2,\ \alpha = 0$	$h/\mathrm{R} = 0.6,\ \alpha = 0$
Variables about relative error	$c = 0.93,\ R^2 = 0.9652,\ \bar{e} = 0.0033,\ \sigma_e = 0.0047$	

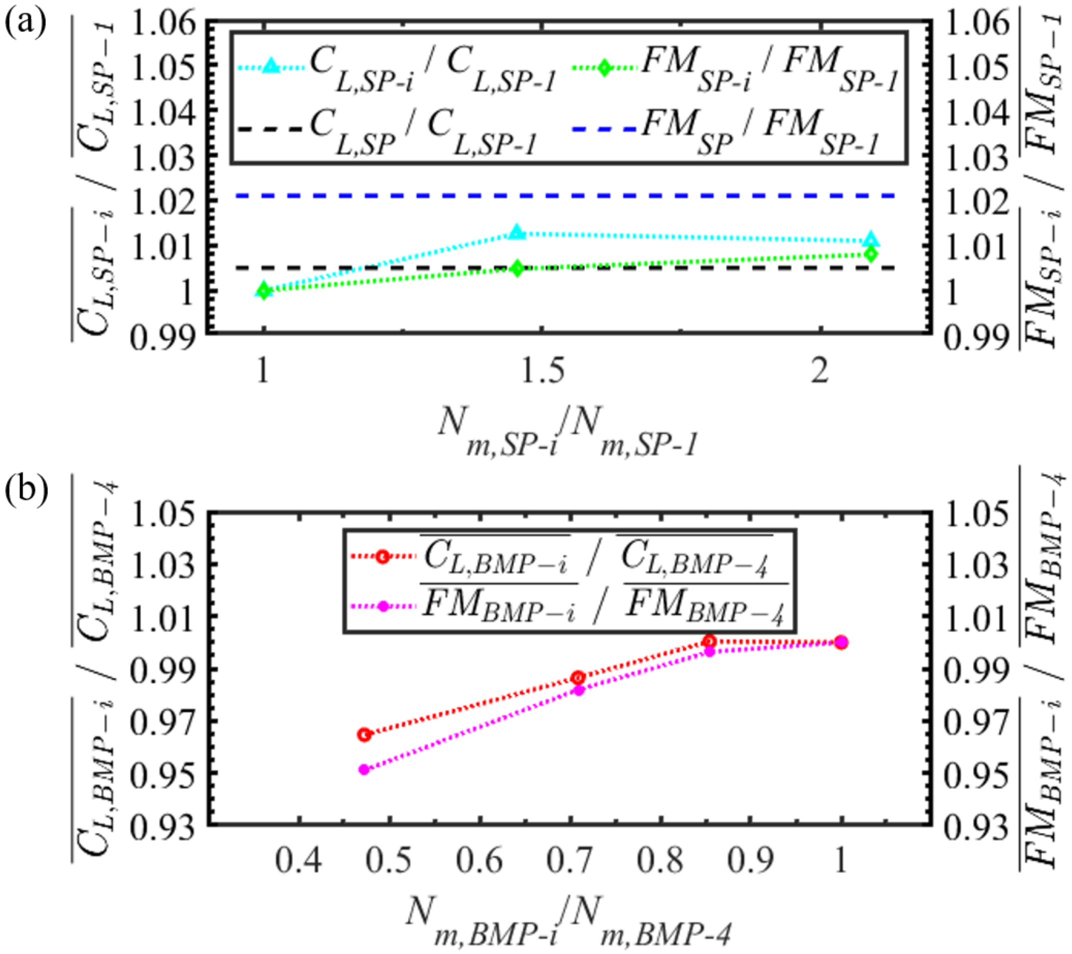

Figure 2-7 Grid sensitivity in CFD simulations for the rotor-configuration. (a) Simulations for single propeller model; (b) simulations for multi-propeller model.

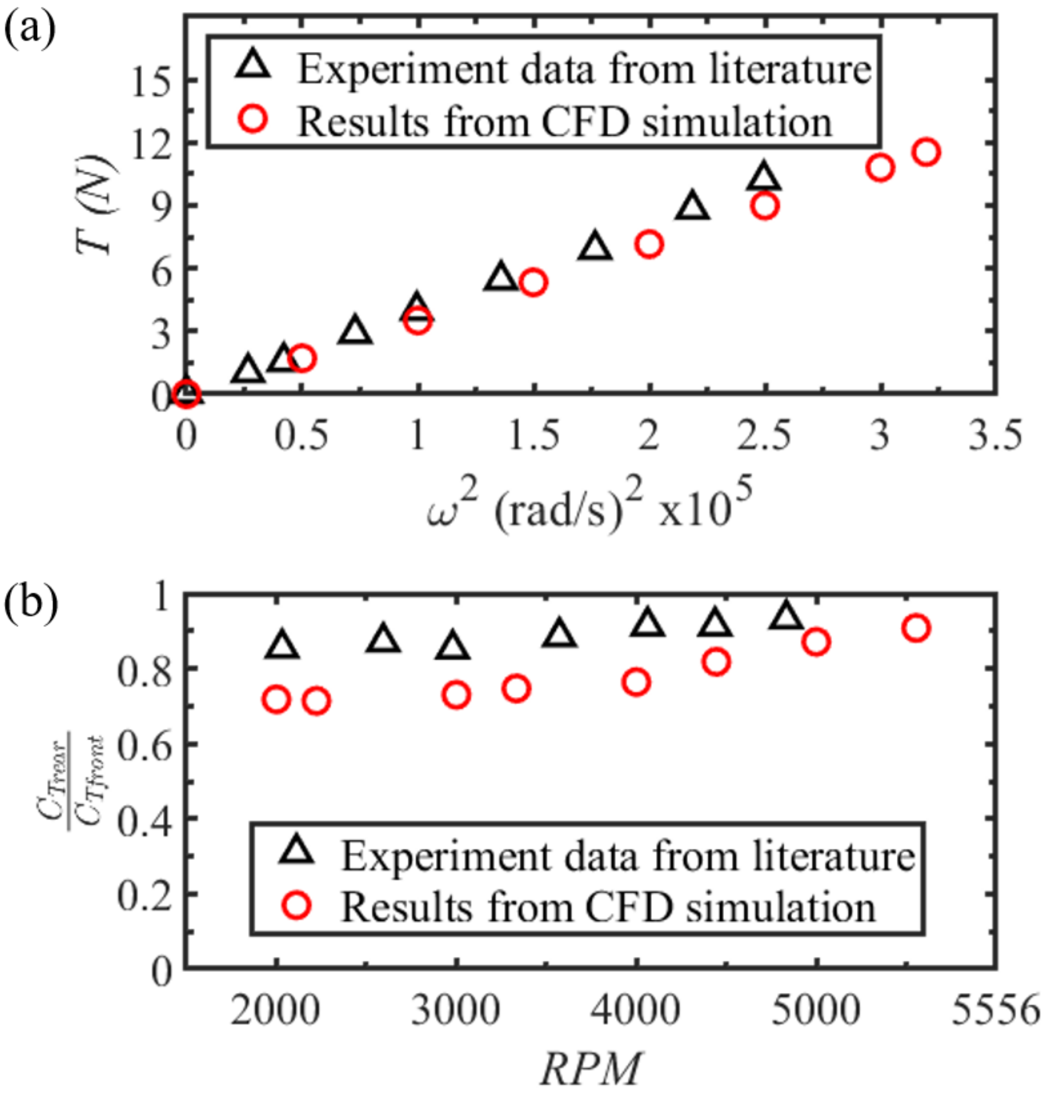

Figure 2-8 Comparisons with experiment data [34] in different situations. (a) Relationship in hover state; (b) interference effect of tandem rotor during forward flight ($\alpha = -5°$, $V = 6\ \mathrm{m \cdot s^{-1}}$, $l/\mathrm{R} = 2.83$).

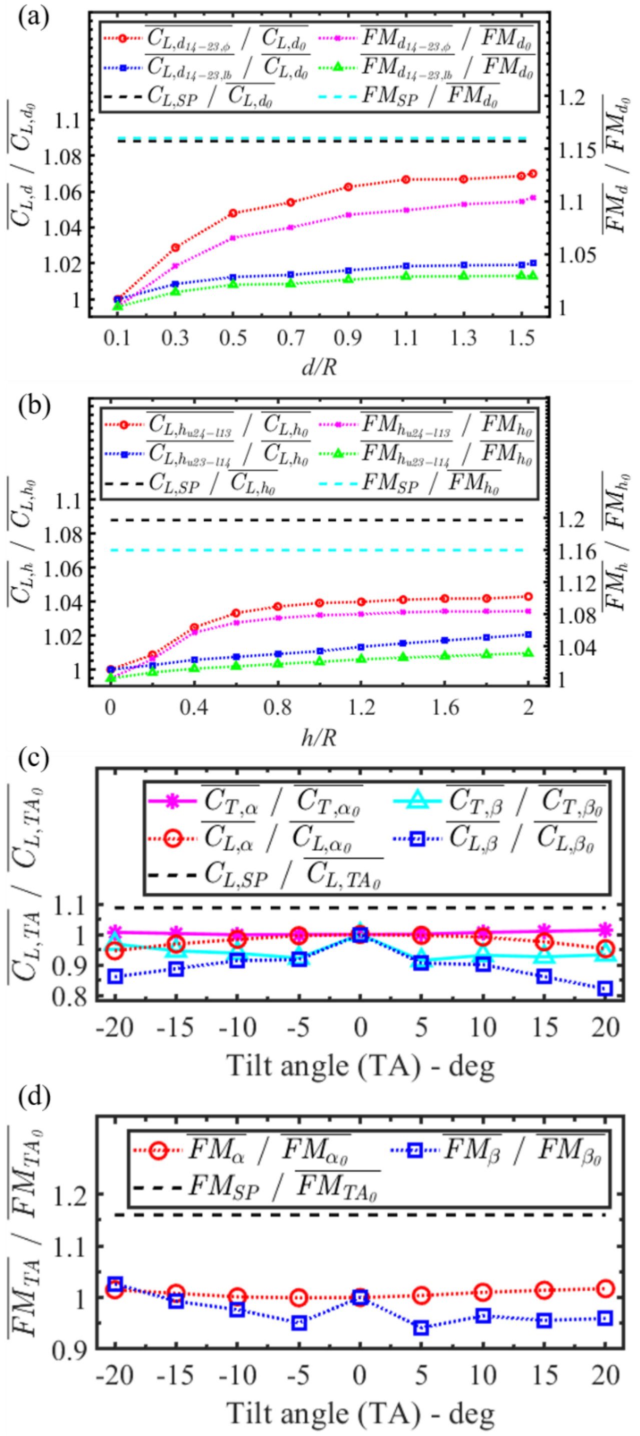

Figure 2-9 Single parameter effect on aerodynamic performances in different rotor-configuration. (a) Average lift coefficient ($\overline{C_{L,d}}$) and $\overline{FM_d}$ vs tip distance, $d_{14-23,\phi}$/R and $d_{14-23,lb}$/R; (b) average lift coefficient ($\overline{C_{L,h}}$) and $\overline{FM_h}$ vs height difference, $h_{u24-l13}$/R and $h_{u23-l14}$/R; (c) average lift coefficient ($\overline{C_{L,TA}}$), average thrust coefficient ($\overline{C_{T,TA}}$) and $\overline{FM_{TA}}$ vs tilt angles, α and β.

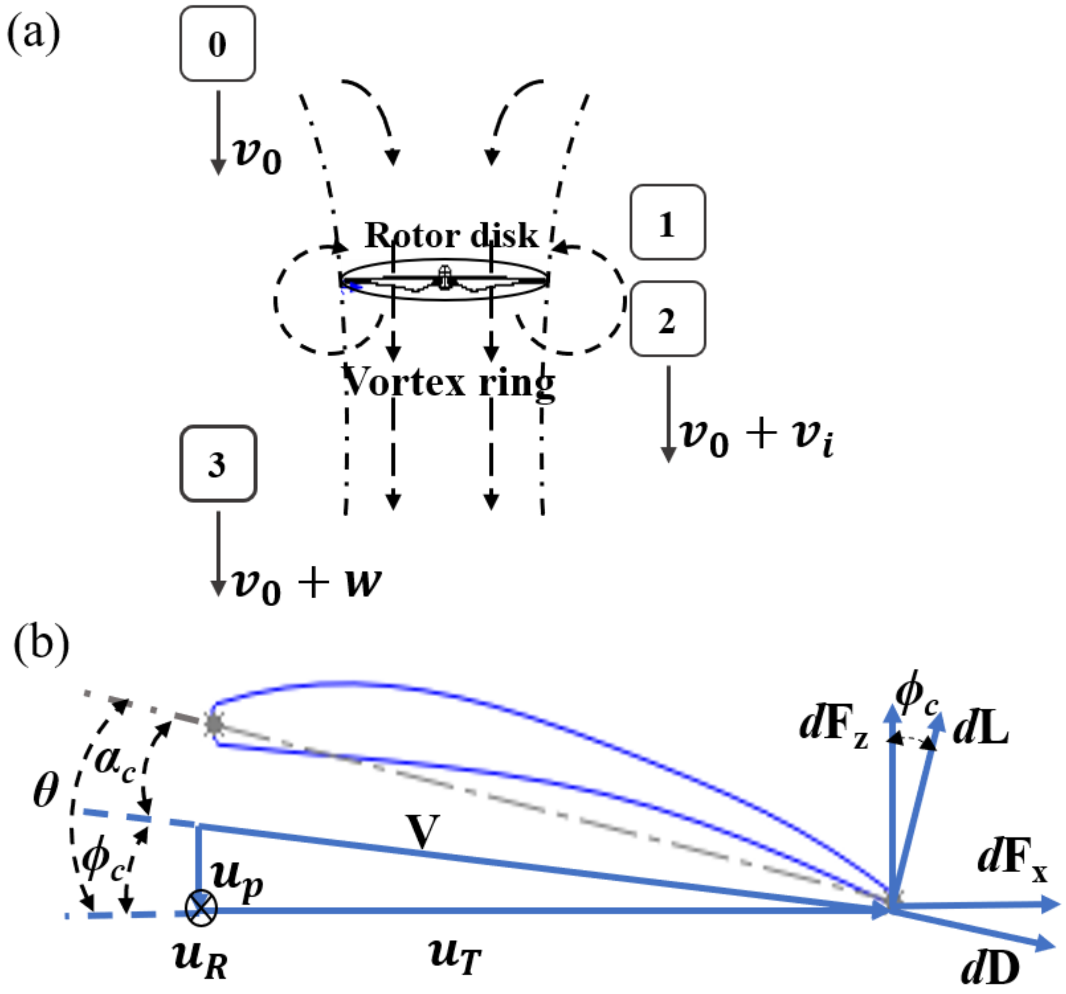

Figure 2-10 Illustration of momentum theory and blade element momentum theory. (a) Rotor disk and downwash [34,47] in hover state with thrust ($T = 2\rho A {v_i}^2$), power ($P = T \cdot v_i$), $v_0 = 0$, induced velocity (v_i), and far wake velocity ($w = 2v_i$); (b) definitions of angle of attack ($\alpha_c = \theta - \phi_c$), pitch angle ($\theta$), and inflow angle ($\phi_c$) at the section of 75%$R$.

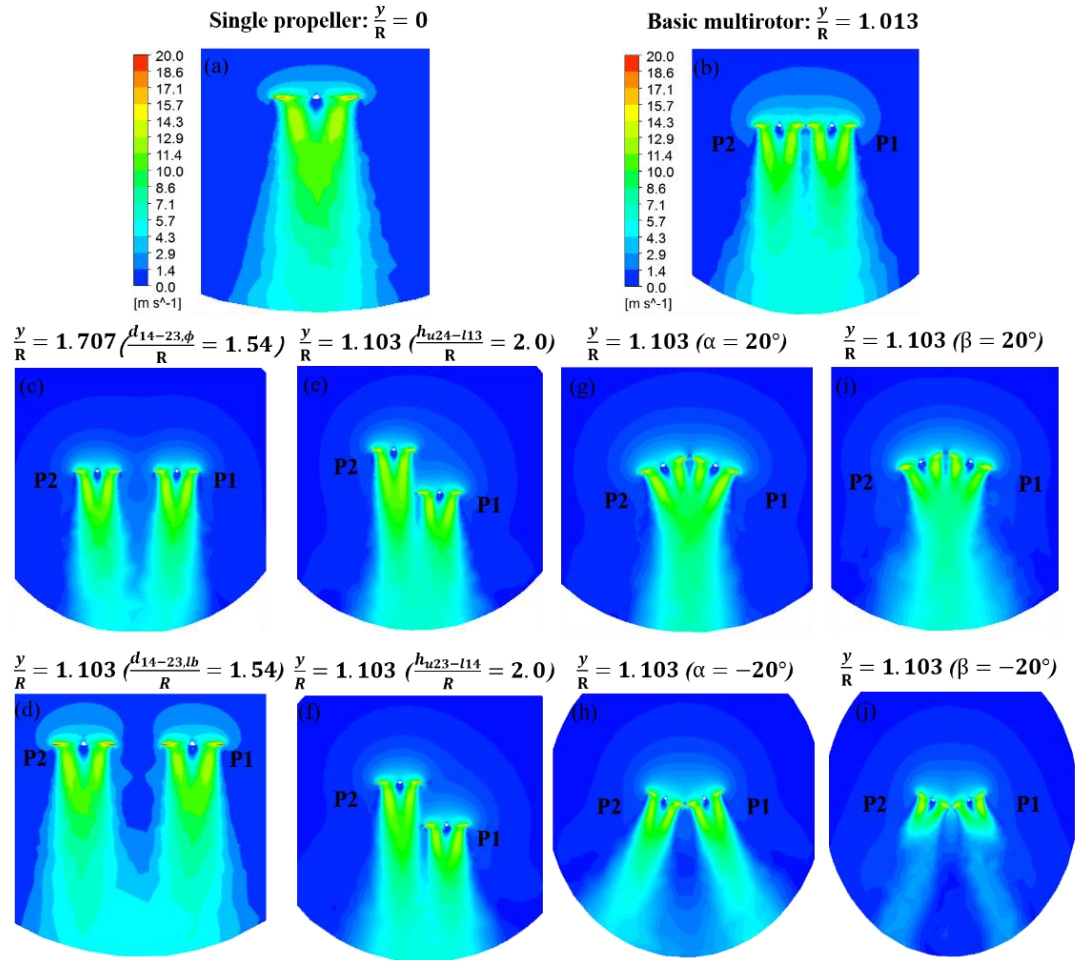
Single propeller: $\frac{y}{R} = 0$

Basic multirotor: $\frac{y}{R} = 1.013$

$\frac{y}{R} = 1.707$ ($\frac{d_{14-23,\phi}}{R} = 1.54$)

$\frac{y}{R} = 1.103$ ($\frac{h_{u24-l13}}{R} = 2.0$)

$\frac{y}{R} = 1.103$ ($\alpha = 20°$)

$\frac{y}{R} = 1.103$ ($\beta = 20°$)

$\frac{y}{R} = 1.103$ ($\frac{d_{14-23,lb}}{R} = 1.54$)

$\frac{y}{R} = 1.103$ ($\frac{h_{u23-l14}}{R} = 2.0$)

$\frac{y}{R} = 1.103$ ($\alpha = -20°$)

$\frac{y}{R} = 1.103$ ($\beta = -20°$)

Figure 2-11 Iso-speed contours about different rotor-configurations at cross-sections of y/R = 1.013 and 1.707 with propellers P1 & P2.

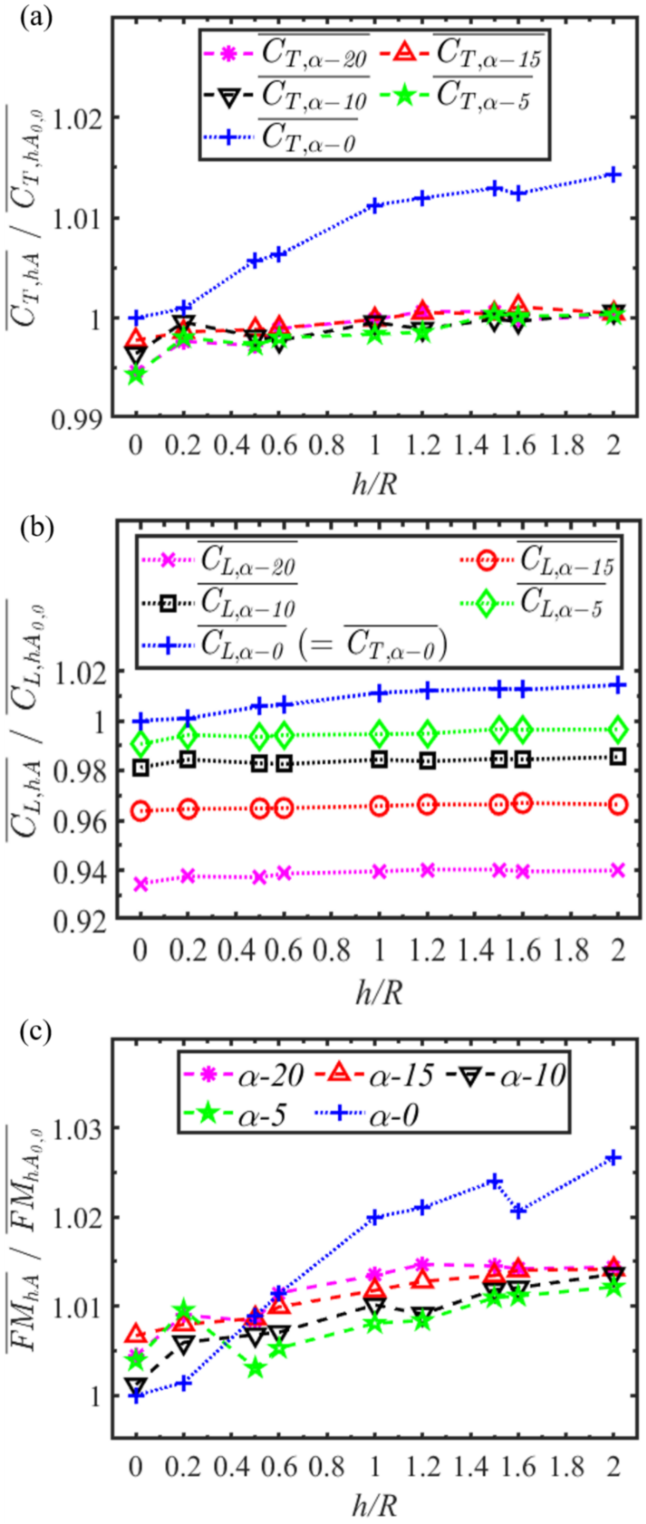

Figure 2-12 Average thrust coefficient ($\overline{C_{T,hA}}$), average lift coefficient ($\overline{C_{L,hA}}$) and $\overline{FM_{hA}}$ vs h and α regarding rotor-configuration.

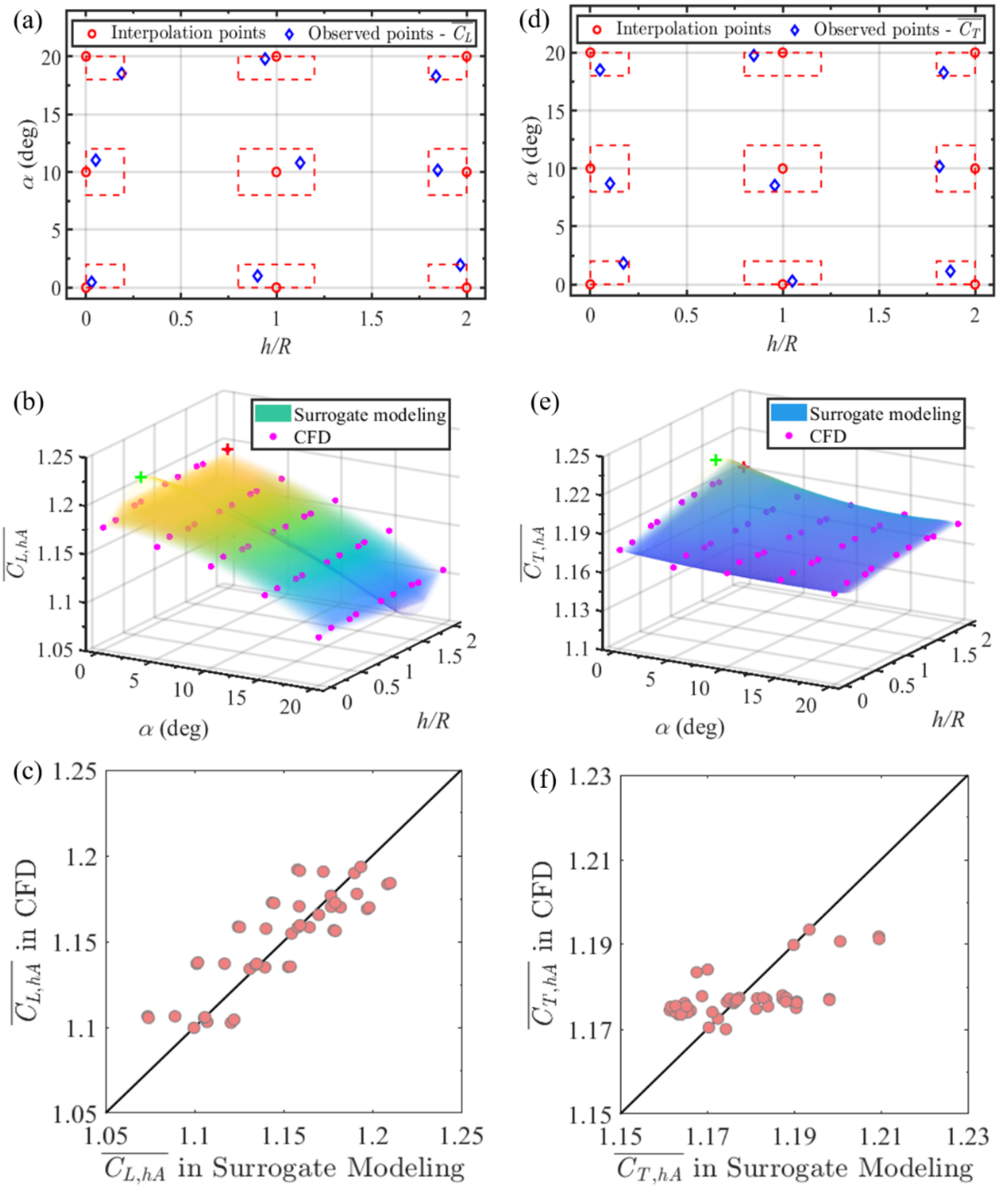

Figure 2-13 Interpolation, optimal observed points adopted in surrogate modeling, and comparisons between CFD and surrogate modeling with IMQ function regarding average lift coefficient ($\overline{C_{L,hA}}$), average thrust coefficient ($\overline{C_{T,hA}}$) for the rotor-configuration. (a-c) Results for $\overline{C_\mathrm{L}}$; (d-f) results for $\overline{C_T}$.

2.4 Conclusions

In this chapter we conducted a systematic CFD-based study for optimal aerodynamic performance of rotor-configuration in hovering quadrotor drone. Motivated by optimal combination of paired wings configuration and stroke-plane inclination in biological flights, we parameterized the rotor-configuration in terms of tip distance, height difference and tilt angle of propellers, and examined how aerodynamic interactions among propellers with various rotor-configurations impact lift force production and FM efficiency. We find that the tip distance effect impacts aerodynamic performance remarkedly, capable of achieving an optimal rotor-configuration with an increase rate of 7.0% in lift force while 10.4% in *FM* compared to the basic configuration. The height difference effect can also lead to significant improvement on aerodynamic performance: a proper optimal rotor-configuration enables an increase rate of 4.3% in lift force while 8.4% in *FM* compared to the basic configuration. Comparatively, the tile angle effect however is minor in hovering state because the inclination of propellers' stroke plane results in a reduction in vertical force, *i.e.*, the lift force and hence FM efficiency. Our results thus point to the importance of aerodynamic interactions among propellers in altering both aerodynamic force production and FM efficiency, and the tip distance effect with the propellers mounted in the same plane obviously plays the most important role. In addition, given that the increase rate of *FM* shows a slight variation with α type tilt angle, proper adjustment of tilt angle may benefit large torque production and hence enhancement in maneuverability rather than the improvement in lift force and FM efficiency, which will be investigated in our future studies.

We further developed a coupling method to explore the optimal aerodynamic performance of rotor-configuration over a broad parameter space by combining the CFD-based simulations and a novel surrogate model, which is validated capable of determining a proper optimal design of rotor-configuration effectively. As a result, we found that the optimal rotor-configuration can be designed with a large tip distance, and some height difference with zero tilt angle, which enables the maximization of aerodynamic interactions among propellers. In conclusion, we propose a biomimetic rotor-configuration design associated with multirotor copters for the sake of improvement in lift force production and FM efficiency. Optimal adjustment associated with tip distance and height difference can benefit most for the optimal aerodynamic performance in quadrotor drone. Moreover, how the current optimal rotor-configuration design works in multirotor copters with large propellers, and how it impacts flight stability and maneuverability remain unclear and will be our future task.

Reference:

[1] Cheng B, Deng X Y, Hedrick T L. The mechanics and control of pitching manoeuvres in a freely flying hawkmoth (Manduca sexta). *The Journal of Experimental Biology*, 2011, 214, 4092–106.

[2] Liu H, Ravi S, Kolomenskiy D, Tanaka H. Biomechanics and biomimetics in insect-inspired flight systems. *Philosophical Transactions of the Royal Society B: Biological Sciences*, 2016, 371.

[3] Liu H, Kolomenskiy D, Nakata T, Li G. Unsteady bio-fluid dynamics in flying and swimming. *Acta Mechanica Sinica/Lixue Xuebao*, 2016, 33, 663–684.

[4] Liu H, Nakata T, Gao N, Maeda M, Aono H, Shyy W. Micro air vehicle-motivated computational biomechanics in bio-flights: Aerodynamics, flight dynamics and maneuvering stability. *Acta Mechanica Sinica/Lixue Xuebao*, 2010, 26, 863–879.

[5] Tobalske B W, Warrick D R, Clark C J, Powers D R, Hedrick T L, Hyder G A, Biewener A A. Three-dimensional kinematics of hummingbird flight. *Journal of Experimental Biology*, 2007, 210, 2368–2382.

[6] Chen D, Kolomenskiy D, Nakata T, Liu H. Forewings match the formation of leading-edge vortices and dominate aerodynamic force production in revolving insect wings. *Bioinspiration & Biomimetics*, 2018, 13, 016009.

[7] Maeda M, Nakata T, Kitamura I, Tanaka H, Liu H. Quantifying the dynamic wing morphing of hovering hummingbird. *Royal Society Open Science*, 2017, 4, 170307.

[8] Nakata T, Liu H. Aerodynamic performance of a hovering hawKmoth with flexible wings: A computational approach. *Proceedings of the Royal Society B: Biological Sciences*, 2012, 279(1729), 722–731.

[9] Cheng B, Tobalske B W, Powers D R, Hedrick T L, Wethington S M, Chiu G T C, Deng X Y. Flight mechanics and control of escape manoeuvres in hummingbirds. I. Flight kinematics. *The Journal of Experimental Biology*, 2016, 219, 3518–3531.

[10] Altshuler D L, Quicazán-Rubio E M, Segre P S, Middleton K M. Wingbeat kinematics and motor control of yaw turns in Anna's hummingbirds (Calypte anna). *The Journal of Experimental Biology*, 2012, 215, 4070–4084.

[11] Liu H. Integrated modeling of insect flight: From morphology, kinematics to aerodynamics. *Journal of Computational Physics*, 2009, 228, 439–459.

[12] Nakata T, Liu H, Bomphrey R J. A CFD-informed quasi-steady model of flapping-wing aerodynamics. *The Journal of Fluid Mechanics*, 2015, 783, 323–343.

[13] Nakata T, Liu H. A fluid-structure interaction model of insect flight with flexible wings. *Journal of Computational Physics*, 2012, 231, 1822–1847.

[14] Yu X, Sun M. A computational study of the wing-wing and wing-body interactions of a model insect. *Acta Mechanica Sinica/Lixue Xuebao*, 2009, 25, 421–431.

[15] Aono H, Liang F Y, Liu H. Near- and far-field aerodynamics in insect hovering flight: An integrated computational study. *The Journal of Experimental Biology*, 2008, 211, 239–257.

[16] Lehmann F O, Sane S P, Dickinson M. The aerodynamic effects of wing-wing interaction in flapping insect wings. *The Journal of Experimental Biology*, 2005, 208, 3075–3092.

[17] Gao N, Aono H, Liu H. Perturbation analysis of 6DoF flight dynamics and passive dynamic stability of hovering fruit fly Drosophila melanogaster. *Journal of Theoretical Biology*, 2011, 270, 98–111.

[18] Gao N, Aono H, Liu H. A numerical analysis of dynamic flight stability of hawkmoth hovering. *Journal of Biomechanical Science and Engineering*, 2009, 4, 105–116.

[19] Floreano D, Wood R J. Science, technology and the future of small autonomous drones. *Nature*, 2015, 460–466.

[20] Hoffmann G M, Huang H, Waslander S L, Tomlin C J. Quadrotor helicopter flight dynamics and control: Theory and experiment. *AIAA Guidance, Navigation and Control Conference and Exhibit*, Hilton Head, South Carolina, 2007.

[21] N.Dief T, Yoshida S. Review: Modeling and Classical Controller Of Quad-rotor. *IRACST - International Journal of Computer Science and Information Technology & Security*, 2015, 5, 314–319.

[22] Winslow J, Benedict M, Hrishikeshavan V, Chopra I. Design, development, and flight testing of a high endurance micro quadrotor helicopter. *International Journal of Micro Air Vehicles*, 2016, 8, 155–169.

[23] Dai X H, Quan Q, Cai K Y. Design automation and optimization methodology for electric multicopter UAVs. *arXiv: 1908.06301v1 [eess.SY]*, 2019, 1–27.

[24] Mintchev S, Floreano D. Adaptive morphology: A Design Principle for Multimodal and Multifunctional Robots. *IEEE Robotics & Automation Magazine*, 2016, 23, 42-54.

[25] Efraim H, Shapiro A, Weiss G. Quadrotor with a Dihedral Angle: on the Effects of Tilting the Rotors Inwards. *The Journal of Intelligent and Robotic Systems*, 2015, 80, 313–324.

[26] Elfeky M, Elshafei M, Saif A W A, Al-Malki M F. Modeling and simulation of quadrotor UAV with tilting rotors. *International Journal of Control, Automation and Systems*, 2016, 14, 1047–1055.

[27] Junaid A B, Sanchez A D D C, Bosch J B, Vitzilaios N, Zweiri Y. Design and

implementation of a dual-axis tilting quadcopter. *Robotics*, 2018, 7, 1–20.

[28] Diógenes H B, dos Santos D A. Modelling, Design and Simulation of a Quadrotor with Tilting Rotors Actuated by a Memory Shape Wire. *Conference: Congresso Brasileiro de Engenharia Mecânica (CONEM)*, agosto de, Fortaleza-Ceará, 2016.

[29] Aleksandrov D, Penkov I. Optimal gap distance between rotors of mini quadrotor helicopter. *8th International DAAAM Baltic Conference*, Tallinn, Estonia, 2012.

[30] Shukla D, Komerath N. Multirotor drone aerodynamic interaction investigation. *Drones*, 2018, 2, 1–13.

[31] Yoon S, Lee H C, Pulliam T H. Computational Analysis of Multi-Rotor Flows. *54th AIAA Aerospace Science Meeting*, San Diego, California, USA, 2016.

[32] Theys B, Dimitriadis G, Hendrick P, De Schutter J. Influence of propeller configuration on propulsion system efficiency of multi-rotor Unmanned Aerial Vehicles. *2016 International Conference on Unmanned Aircraft Systems (ICUAS)*, Arlington, VA USA, 2016.

[33] Lei Y, Wang J L. Aerodynamic Performance of Quadrotor UAV with Non-Planar Rotors. *Applied Science*, 2019, 9, 2779.

[34] Nguyen H D, Liu Y, Mori K. Experimental Study for Aerodynamic Performance of Quadrotor Helicopter. *Transactions of the Japan Society for Aeronautical and Space Sciences*, 2018, 61, 29–39.

[35] Nguyen H D, Liu Y, Mori K. Unsteady aerodynamic parameter estimation for multirotor helicopters. *Transactions of the Japan Society for Aeronautical and Space Sciences*, 2019, 62, 32–40.

[36] Noda R, Nakata T, Ikeda T, Chen D, Yoshinaga Y, Ishibashi K, Rao C, Liu H. Development of bio-inspired low-noise propeller for a drone. *Journal of Robotics and Mechatronics*, 2018, 30, 337–343.

[37] Ikeda T, Tanaka H, Yoshimura R, Noda R, Fujii T, Liu H. A robust biomimetic blade design for micro wind turbines. *Renew Energy*, 2018, 125, 155–165.

[38] Ellington C P. The aerodynamics of hovering insect flight. V. A vortex theory. *Philosophical Transactions of the Royal Society of London. Series B, Biological Sciences*, 1984, 305, 115–144.

[39] Usherwood J R, Ellington C P. The aerodynamics of revolving wings I. Model hawkmoth wings. *The Journal of Experimental Biology*, 2002, 205, 1547–1564.

[40] Forrester A I J, Keane A J. Recent advances in surrogate-based optimization. *Progress in Aerospace Science*, 2009, 45, 50–79.

[41] Bouhlel M A, Hwang J T, Bartoli N, Lafage R, Morlier J, Martins J.R.R.A. A Python surrogate modeling framework with derivatives. *Advance in Engineering Software*, 2019,

135, 1–27.

[42] Lee H M, Hur N K, Kwon O J. Aerodynamic Design Optimization of UAV Rotor Blades using a Genetic Algorithm. *The 2015 World Congress on Aeronautics, Nano, Bio, Robotics, and Energy (ANBRE15)*, Incheon, Korea, 2015.

[43] Zhong H H, Zhang K S. *Surrogate-Based Optimization*. Real-World Applications of Genetic Algorithms, 2012.

[44] Fornberg B, Flyer N. Solving PDEs with radial basis functions. *Acta Numerica*, 2015, 24, 215–258.

[45] Bhatia G S, Arora G. Radial basis function methods for solving partial differential equations-A review. *Indian Journal of Science and Technology*, 2016, 9.

[46] Koushki M, Jabbari E, Ahmadinia M. Evaluating RBF methods for solving PDEs using Padua points distribution. *Alexandria Engineering Journal*, 2020, 59, 2999–3018.

[47] Bangura M, Melega M, Naldi R, Mahony R. Aerodynamics of Rotor Blades for Quadrotors. *arXiv: 1601.00733v1 [physics.flu-dyn]*, 2016.

Chapter 3 Effect of Ducted Multi-Propeller Configuration on Aerodynamic Performance in Quadrotor Drone

3.1 Introduction

The quadrotor drone has been utilized so extensively due to its great flight capability [1-5]. For sake of improve its aerodynamic performance, many researches have been performed relative to design of propeller and fuselage [6-12]. And based on the bioinspiration of flight ability performed by insects and birds [13-19], a biomimetic optimal non-ducted rotor-configuration (Figure 1-6) with a large rotor-to-rotor tip distance, some height difference and zero tilt angle that is verified to be capable of achieving optimal aerodynamic performance for the quadrotor drone (Figure 1-5) is proposed in section 2.3.3, which enables optimal aerodynamic interactions among propellers, leading to a marked improvement in lift force production with an increase rate of 9% compared to that of a basic non-ducted multi-propeller configuration (Figure 1-5), thus enhancing the FM efficiency. However, some designs should be proposed for the modification of rotor-configuration in the quadrotor drone because the obtained rotor-configuration leads to a larger frame of the quadrotor drone as illustrated in Figure 1-6 compared with the basic rotor-configuration as illustrated in Figure 1-5, which occupies a large space during the flight, resulting in the impairment of agility about the drone. To further improve the aerodynamic performance of the quadrotor drone while reduce its frame dimension, we chose the approach of employing the ducted-propeller design [20] and adopting the multirotor configuration adjustment [21] to optimize the aerodynamic performance of multirotor drones associated with the lift force production and FM efficiency. However, since the duct needs to be carefully shaped so as to avoid the propeller-duct interaction penalty, while being as light as possible to minimize the weight increase [22], the duct design applied to the rotor-configuration optimization of ducted multi-propeller should be explored in accordance with different propellers of multirotor copter, which comprises the definition of duct's cross-section and tip clearance between propeller tip and duct inwall.

With respect to the ducted-propeller application in UAVs and MAVs, the shroud (duct) designs with different blades, and shroud dimensions have been proposed and developed to evaluate the performance in hover and edgewise flow experimentally by Hrishikeshavan *et al.* [10–12]. The interference of ducted fans installed with a height difference was also investigated through numerical simulations solving Reynolds-averaged Navier-Stokes (RANS) equations with Shear Stress Transport (SST) turbulence model and experimental investigation in hovering regime by Arkhipov *et al.* [23] and Stremousov *et al.* [24]. The energy efficiency improvement and the thrust power increase of UAVs were studied by implementing shrouded rotors that have different leading-edge lip radius (LLR), diffuser length (DL) and diffuser angle (DA) with ANSYS CFX simulations and experiments by Chua *et al.* [25]. A ducted fan MAV was developed and optimized to improve the drone's maneuverability with experiments by Moaad *et al.* [26]. The influence on lift force was studied with propeller shrouding of different shroud diameters and shroud heights in mini unmanned quadcopter computationally and experimentally by Penkov *et al.* [27]. The rotor-duct aerodynamic interactions were investigated by means of stereo particle image velocimetry (SPIV) through aeroacoustics measurements on a rotor having removable protective duct over a range of hover conditions at low Reynolds numbers by Shukla *et al.* [28]. Recently, the aerodynamic characteristics of ducted single-propeller in various duct contours were examined as well as the aerodynamic characteristics of ducted propellers in a quadrotor drone were investigated under hovering condition with and without crosswind experimentally and numerically by Yonezawa *et al.* [29,30]. Until now, most studies have been focused on the aerodynamic optimization of ducts with some fixed propeller-configuration, aiming to improve lift force production and/or maneuverability of multirotor copters. It still remains poorly understood how the different configurations of ducted multi-propeller affect the aerodynamic performance of the multirotor copter associated with lift force production and FM efficiency in terms of tip distance and height difference adjustment, as well as which is the optimal ducted multi-propeller configuration with these two parameters.

In this chapter, we perform an integrated simulation-based study of CFD simulations and a surrogate model to investigate the effect of the ducted multi-propeller configuration on aerodynamic performance and to explore the optimal ducted multi-propeller configuration of a quadrotor drone. We first explore a high-performance and compact duct design in terms of aerodynamic performance and duct volume based on CFD results of ducted single-propeller models. The duct design obtained is then adopted to a quadrotor drone to examine the effect of the ducted multi-propeller configuration on aerodynamic performance associated with tip distance and height difference among various ducted propellers. Furthermore, an extensive analysis of the optimal ducted multi-propeller configuration is conducted through the combination of CFD simulations and a surrogate model to search for the optimized design in a broad-parameter space of the tip distance and height difference, which is verified to improve both lift force production and FM efficiency compared to those in the previous obtained optimal non-ducted rotor-configuration.

3.2 Materials and methods

3.2.1 Aerodynamic theory of a ducted propeller

Estimation of the aerodynamic lift force on an isolated propeller in a ducted-propeller model is derived from the momentum theory, the blade element theory, and the aerodynamic principle of a ducted propeller [9,31,32] (Figure 3-1). The duct is composed of a straight or tapered trailing edge and a rounded leading edge formed as the diffuser and inlet section, respectively. When the propellers rotated, the rotor operation generates a suction pressure gradient on the duct inlet surface, thus resulting in an additional lift force, which contributes to the total lift force production and hence enhances the FM efficiency [10–12].

3.2.2 Geometric model of ducted propeller

3.2.2.1 Ducted single-propeller geometry

The duct is generally composed of a straight diffuser section and an elliptic or pseudo-elliptic inlet (Figure 3-2), which is verified to enable a significant improvement in lift/thrust force production and power reduction particularly at low rotational speeds and/or with high disk-loading [10–12]. Therefore, in this study, the duct with an ellipse inlet is employed and the aerodynamic performance of ducted-propeller units is discussed extensively. To determine a high-performance duct design in the ducted single-propeller model in terms of the duct's cross-section and tip clearance, six parameters in *toto* are utilized, including the tip clearance (d_e) expressing the gap between propeller tip and duct inwall; the propeller height (h_p), *i.e.*, the height difference between the center of the inlet ellipse (point D) and the center of the propeller bottom (point P); the diffuser angle (α) denoting the inclination angle of the diffuser; the diffuser length (l_e); the height of ellipse inlet (h_e); and the radius of the ellipse inlet (r_e), with an original value of d_e = 0.001 m , h_p = 0, α = 0, l_e = 0.06 m (0.5R), h_e = 0.06 m (0.5R), and r_e = 0.02 m (0.167R) (Figure 3-2). Except that, the thickness of the duct model is fixed to be 0.0015 m. The 3D single-propeller model is identical to that in section 2.2.1. A systematic CFD-based analysis was conducted to examine the high-performance duct model in terms of the aerodynamic performance and the duct volume.

3.2.2.2 Ducted multi-propeller geometry

The ducted multi-propeller model is generated based on the duct model employed in section 3.2.2.1. Figure 1-5 and Figure 1-6 show the geometric models of a basic non-ducted multi-propeller configuration (Figure 1-5b) and a maximum non-ducted multi-propeller configuration (Figure 1-6) obtained in section 2.3.3, which is also the optimal configuration with a maximum rotor-to-rotor tip distance, verified to be capable of improving both lift force production and FM efficiency in the quadrotor drone of DJI phantom 3 advanced. Given the high-performance duct model as an initial input to the ducted multi-propeller configuration with the maximum rotor-to-rotor tip distance, the ducted maximum multi-propeller configuration (Figure 3-3a) is formed, and the ducted minimum multi-propeller configuration (Figure 3-3b) is generated through altering the rotor-to-rotor tip distance and height difference. Based on the analysis of lift force production and FM efficiency in a broad parameter space associated with the tip distance and height difference (as seen in sections 3.3.2 and 3.3.3), the effect and optimization of a ducted multi-propeller configuration on aerodynamic performance are investigated based on a combination of CFD simulations and a surrogate model over the design space.

3.2.3 CFD modeling

CFD-based simulations of ducted rotor-configuration models were also conducted with the commercial software ANSYS CFX 14.5 (ANSYS Inc) under the conditions of a rotational speed of 5400 rpm for all propeller models with ducts, which is identical to that utilized in non-ducted rotor-configuration models. The Reynolds number (R_e) of a single propeller is still 7.4×10^4, and the RANS modelling of turbulent flow with the SST turbulence model was still adopted with a 'high-resolution mode' for all the simulations of ducted single-propeller and ducted multi-propeller models [33,34]. Following the Refs. [33,34], we generated the inflation layer meshes with seven layers surrounding the propeller surfaces to ensure high resolution of the boundary layer adjacent to walls while being clustered at the wingtip, leading edge, and trailing edge. Approximately 26 million and 48 million meshes (see in sections 3.3.1 and 3.3.2) were successively generated for the ducted single-propeller and ducted multi-propeller, respectively. Furthermore, boundary conditions and grid systems are given in Figure 3-4. A "Frozen Rotor (FR)" approach was utilized at the interface between inner rotating and outer stationary regions of both ducted single-propeller and multi-propeller models to give the rotor an appointed constant rotating speed for the sake of 'freezing' the relative movements between the two frames, which thus ensures convergence to a stable state.

Besides, a ‘General Connection with No Frame Change/Mixing’ model was employed at the interface between intermediate stationary regions and coarse stationary regions of ducted multi-propeller models for connection. In addition, the wall boundary was used at the duct surfaces, and the open (free-stream boundary) condition with 0 Pa pressure was adopted at the outside boundary of the spherical surface, as illustrated in Table 3-1.

FM efficiency [33] is still adopted to evaluate the aerodynamic performance of the ducted single-propeller model and defined as:

$$FM_{D-SP} = \frac{P_{RF,D-SP}}{P_{CFD,D-SP}}, \tag{3-1}$$

where $P_{RF,D-SP}$ denotes the minimum power derived from the Rankin–Froude momentum theory for generating lift force based on numerical results. $P_{CFD,D-SP}$ is calculated from a product of the torque around rotational axis, Q, and the rotational angular velocity, ω, which are formulated as:

$$\begin{cases} P_{RF,D-SP} = L_{D-SP}\sqrt{\frac{L_{D-SP}}{2\rho A_{SP}}}, \\ P_{CFD,D-SP} = Q \cdot \omega \end{cases} \tag{3-2}$$

where L_{D-SP} expresses the lift force of the ducted single propeller ($L_{D-SP} = L_P + L_D$, L_P: Lift force on propeller; L_D: Lift force on duct). A_{SP} is the actuator disk’s area defined by the propeller’s radius, R, and ρ is the air density.

For the ducted multi-propeller models with various configurations of tip distance and height difference, Equations (3–1) and (3-2) can be further used in the evaluation of aerodynamic performance with some refinements, where the FM efficiency of a ducted multi-propeller model is defined as FM_{D-MP}, with the L_{D-SP} substituted for the ducted-multi-propeller-induced lift force, L_{D-MP} ($L_{D-MP} = L_{MP} + L_{MD}$, $L_{MP} = L_{P1} + L_{P2} + L_{P3} + L_{P4}$, $L_{MD} = L_{D1} + L_{D2} + L_{D3} + L_{D4}$), the A_{SP} by A_{MP} ($A_{MP} = 4A_{SP}$), and the $P_{CFD,D-SP}$ by $P_{CFD,D-MP}$ (P_{CFD} of ducted multi-propeller: $P_{CFD,D-MP} = Q_1 \cdot \omega_1 + Q_2 \cdot \omega_2 + Q_3 \cdot \omega_3 + Q_4 \cdot \omega_4$), respectively. Comparatively, regarding the ducted basic multi-propeller configuration model with one duct surrounding the outside, the L_{D-SP} will be replaced by the lift force, L_{D-BMP} (lift force of ducted basic multi-propeller: $L_{D-BMP} = L_{BMP} + L_{D-B} = L_{P1} + L_{P2} + L_{P3} + L_{P4} + L_{D-B}$, L_{D-B}: Lift force on duct surrounding outside).

3.2.4 Optimization of aerodynamic performance in ducted multi-propeller configuration

With respect to the optimization for ducted rotor-configuration, CFD-based simulations of 22 cases (see section 3.3.2) with various ducted multi-propeller configurations associated with different tip distances and height differences were conducted to examine the effect of ducted multi-propeller configurations on their aerodynamic performance. Furthermore, a surrogate model combined with a set of CFD-based cases (35 cases in total with additional 13 cases, see section 3.3.3) was employed to explore the optimal ducted multi-propeller configuration in terms of L_{D-MP} and FM_{D-MP} in a broad parametric space of tip distance and height difference.

The surrogate modeling with an alternative interpolation method of Radial basis functions (RBFs) model was verified to be a versatile while fast optimization method [35]. It is implemented in the three steps here: (1) specification of a design space based on CFD-based numerical experiments comprising 35 discrete points associated with two parameters (tip distance and height difference); (2) CFD simulations at the design points; and (3) construction of a surrogate model based on the CFD simulations to achieve a continuous output over the entire design space [36]. As a result, a continuous map as a continuous spatial surface of L_{D-MP} or FM_{D-MP} will be yielded in the parametric space.

In the RBFs approach, L_{D-MP}, or FM_{D-MP} is approximated as an unknown function of *f(x)* at an untried point x, which is formally derived from a linear combination of radial basis functions, defined as

$$f(x) = \sum_{i=1}^{n} w_i \varphi(r), \tag{3-3}$$

where w_i is the i-th weight coefficient, and $\varphi(r) = \varphi(\|x^i - x\|)$ is the basic function determined by the Euclidean distance between the prescribed observed point x^i and untried point x [37,38]. In order to determine the weight coefficient w_i, a series of interpolation points of x^j that have known results from CFD simulations were introduced to substitute the untried points of x, where all the interpolation points should satisfy:

$$f(x^j) = \sum_{i=1}^{n} w_i \varphi(r) = \sum_{i=1}^{n} w_i \varphi(\|x^i - x^j\|) = y^j, \text{j=1, 2, …, n.} \tag{3-4}$$

where x^j and y^j denotes the interpolation point, and the result at the corresponding interpolation point, respectively. Thus, with the known observed points and interpolation points, the weight coefficient w_i can be determined subsequently. For sake of determining the locations of interpolation points in the design space, DoE (Design of Experiments) method in terms of Uniform Design (UD) [36] was employed to maximize the amount of information obtained from a limited number of sample discrete points, *i.e.*, CFD simulation-based L_{D-MP}, or FM_{D-MP}. Consequently, nine interpolation points (n = 9) were employed based on the parametric space virtually based on the trial-and-error verification in section 2.2.3, which is verified to be effective enough to provide a reasonable approximation. Moreover, the optimal observed points were determined in the vicinity of interpolation points correspondingly by Random selection.

The IMQ (Inverse Multiquadric) function was still selected in a manner of trial-and-error from multiple options of basic function in RBFs model [37–38] and utilized at all untried and test points, corresponding to those based on CFD simulations, because it was confirmed capable of giving reasonable results on the approximation of L_{D-MP}, or FM_{D-MP} with least relative error, which is defined as

$$\varphi(r) = \frac{1}{\sqrt{r^2+c^2}}, 0 < c < 4. \tag{3-5}$$

The weight coefficient w_i was determined by adjusting the coefficient, c, in the basic function of $\varphi(r)$ through solving the Eq. (3-3) based on the information at interpolated and observed points. To estimate the numerical errors between surrogate modeling and CFD simulations, three variables ($\bar{e}$, R^2 and σ_e) were still introduced based on all the test points, in which an average relative error ($\bar{e}$) is defined as

$$\bar{e} = \frac{1}{n_t}\sum_{i=1}^{n_t} e^i = \frac{1}{n_t}\sum_{i=1}^{n_t} \left\| \frac{\widehat{y^i}-y^i}{y^i} \right\|, \tag{3-6}$$

where n_t is the number of test points (n_t = 35 for the ducted rotor-configuration optimization); y^i is the true value (came from the results of CFX calculations), and $\widehat{y^i}$ is the prediction of surrogate modeling at the i-th test point, respectively.

The R-squared (R^2) is defined as

$$R^2 = 1 - \frac{\sum_{i=1}^{n_t}(y^i-\widehat{y^i})^2}{\sum_{i=1}^{n_t}(y^i-\bar{y})^2}, \tag{3-7}$$

where $\bar{y}$ denotes the average of true value based on CFD simulations. Furthermore, the root mean squared error (σ_e) is defined as

$$\sigma_e = \sqrt{\frac{1}{n_t}\sum_{i=1}^{n_t}(e^i)^2}. \tag{3-8}$$

Convergence criteria have little difference compared with the optimization of non-ducted rotor-configuration, which are defined as $\bar{e} < 0.0025$, $R^2 > 0.945$, and $\sigma_e < 0.0025$ for the ducted rotor-configuration optimization because there is a difference about the number of test points between the non-ducted rotor-configuration results (n_t = 45) and ducted rotor-configuration results (n_t = 35) obtained from the CFD-based simulations. An inner iteration is designed to examine the optimal variables with the coefficient (c) varying over a predetermined parametric range (Equation (3-5)), which is conducted as described in flow chart of the optimization procedure (Figure 3-5).

Table 3-1 Numerical settings of CFD model for ducted rotor-configuration

	Ducted single-propeller model	**Ducted multi-propeller model**
Simulation type	Steady	Steady
Turbulence model	Shear stress transport (SST)	Shear stress transport (SST)
Open boundary	Free-outflow with 0 Pa pressure	Free-outflow with 0 Pa pressure
Wall boundary	No-slip, smooth wall	No-slip, smooth wall
Rotation region's domain interface	Frozen rotor	Frozen rotor
Intermediate stationary region's domain interface	–	General connection with no frame change/mixing
Rotational speed (rpm)	5400	5400
Mesh elements number ($\boldsymbol{N_m}$)	Approx. 26 million	Approx. 48 million

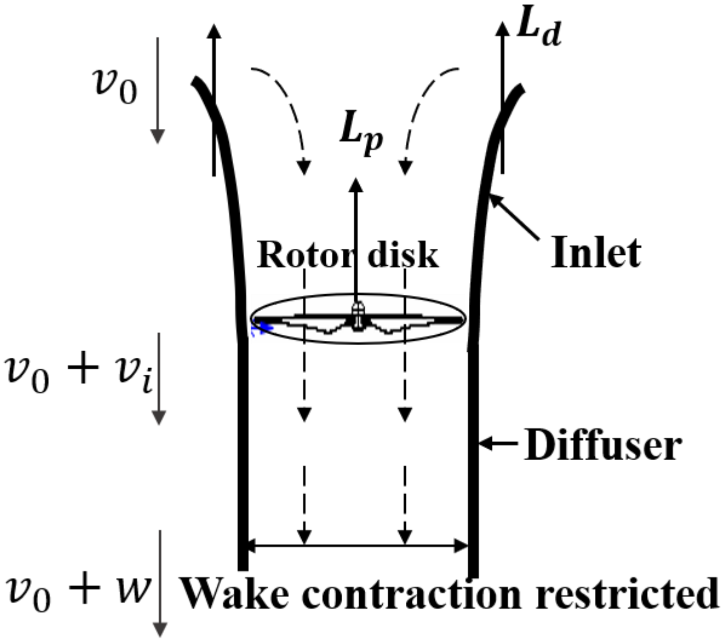

Figure 3-1 Schematic diagram of the ducted-propeller aerodynamic principle. Rotor disk and downwash in hovering state: Lift force generated by propeller ($L_p = 2\rho A {v_i}^2$), $v_0 = 0$, induced velocity (v_i), and far wake velocity ($w = 2v_i$), additional lift force generated by duct (L_d).

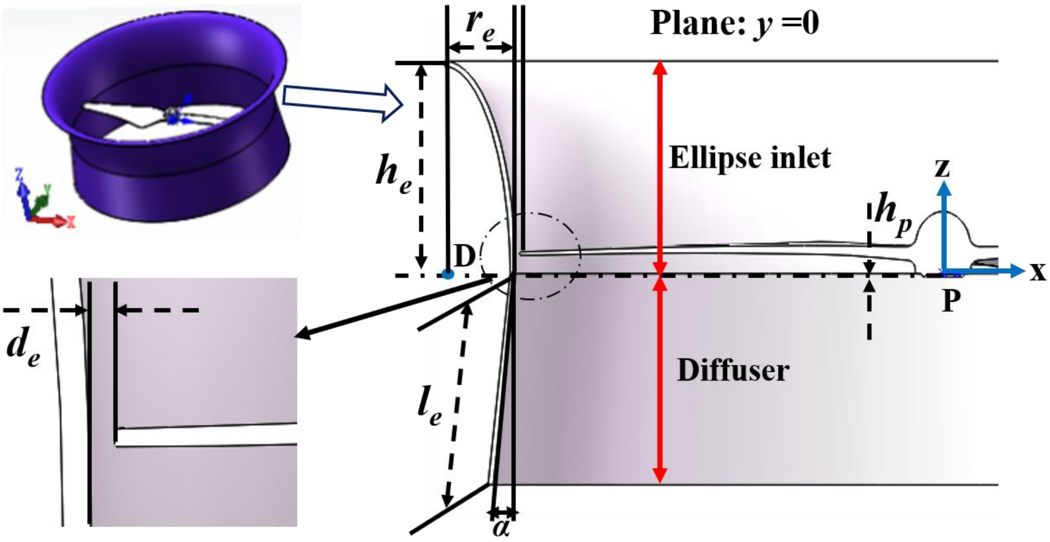

Figure 3-2 Morphological parameters of the ducted single propeller model. Tip clearance (d_e), propeller height (h_p: Being positive when point D is beyond point P and vice versa), diffuser angle (α: Being positive with inclination outward but negative with inclination inward), diffuser length (l_e), height of ellipse inlet (h_e), and radius of ellipse inlet (r_e).

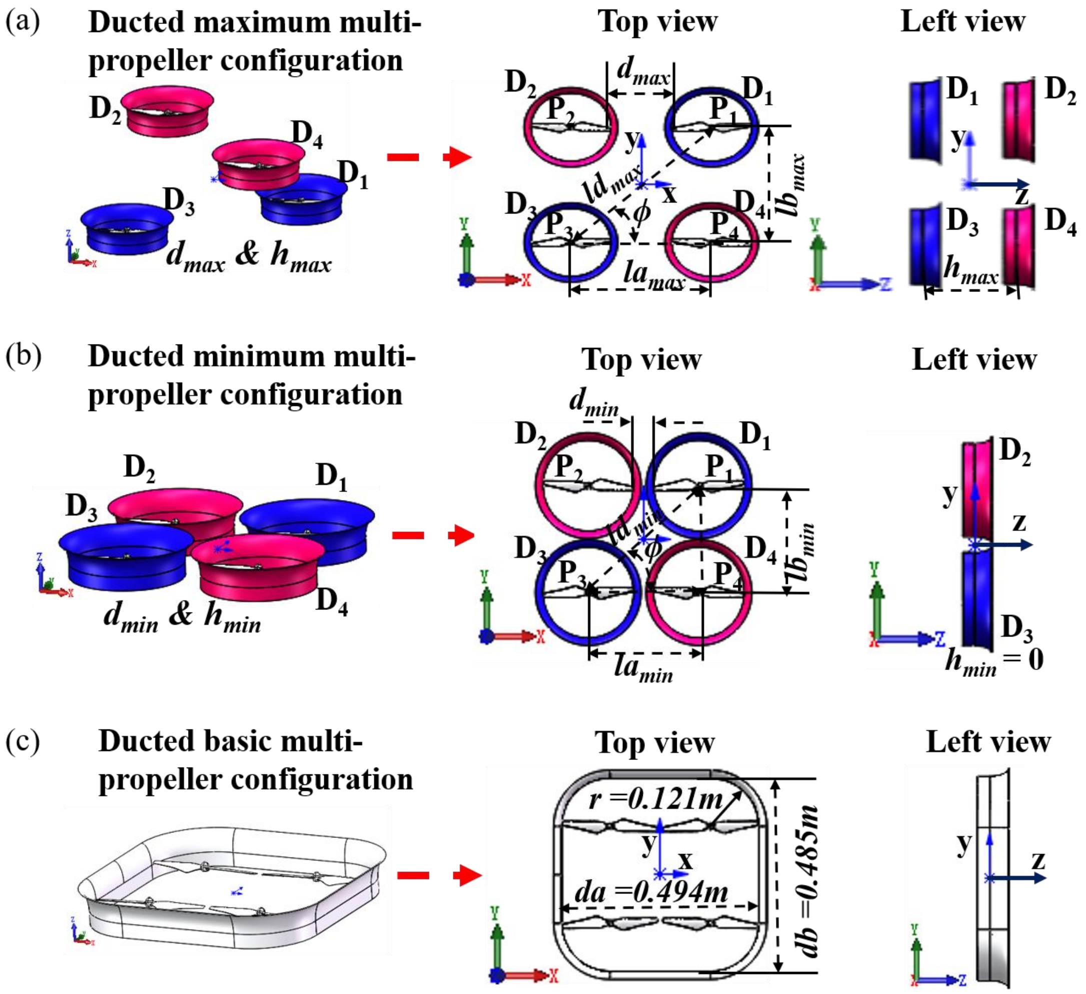

Figure 3-3 Definitions of various configurations of the ducted multi-propeller model regarding tip distance and height difference. (a) Ducted maximum multi-propeller configuration with $d_{max} \approx 0.185$ m, $h_{max} = 0.24$ m, $la_{max} \approx 0.425$ m, $lb_{max} \approx 0.410$ m, $ld_{max} = 0.59$ m at an inclination angle of $\emptyset \approx 44°$; (b) ducted minimum multi-propeller configuration with $d_{min} \approx 0.055$ m, $h_{min} = 0$, $la_{min} \approx 0.295$ m, $lb_{min} \approx 0.285$ m, $ld_{min} = 0.41$ m at an inclination angle of $\emptyset \approx 44°$; (c) ducted basic multi-propeller configuration with $da = 0.494$ m, $db = 0.485$ m, and $r = 0.121$ m.

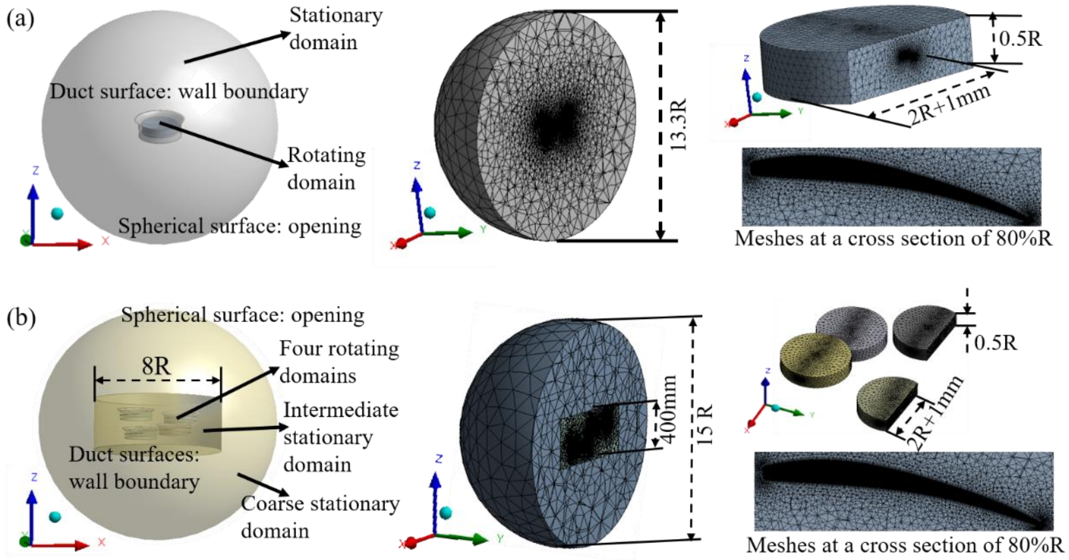

Figure 3-4 Mesh systems and boundary conditions for the ducted rotor-configuration in CFD simulations. (a) Ducted single-propeller model; (b) ducted multi-propeller model.

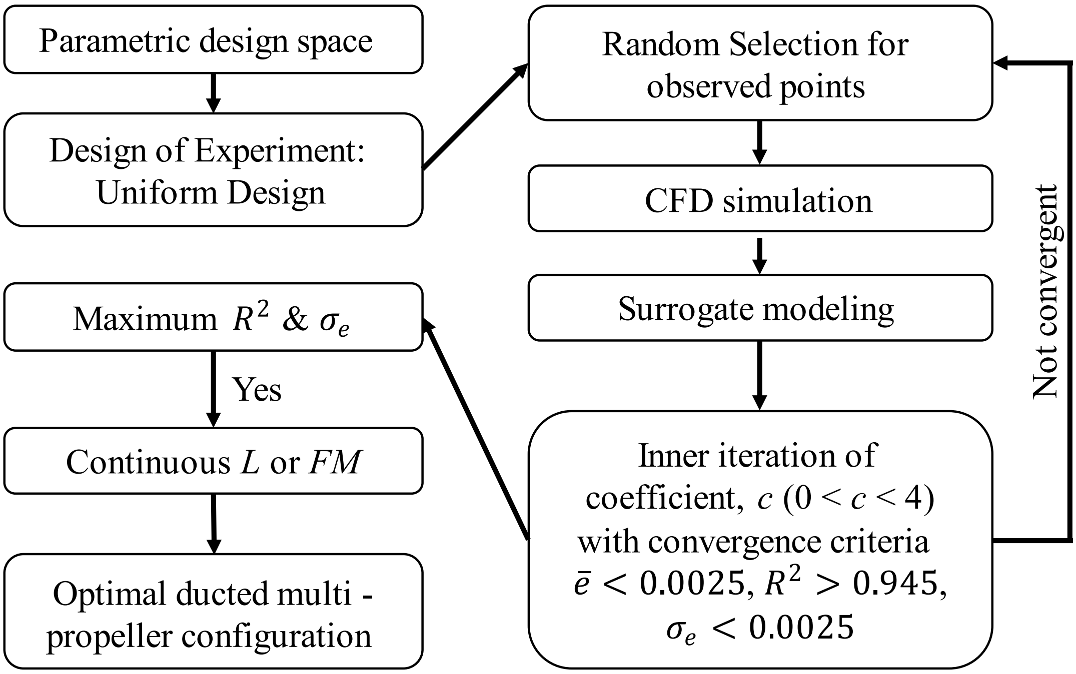

Figure 3-5 Flow chart of CFD-and surrogate model-based optimization analysis for ducted rotor-configuration.

3.3 Results and discussions

3.3.1 High-performance duct design in ducted single-propeller model

3.3.1.1 Verification and validation

Verification was carried out via self-consistency on mesh independency. The minimum grid spacing adjacent to the wall (propeller) surface, δ_m, is controlled by $\delta_m \approx 0.1l/\sqrt{R_e}$, where $R_e = 7.4\times10^4$, $l = 0.0162$ m (chord length at 75%R) [34], resulting in the minimum grid spacing of 0.015 mm. We composed a baseline case of the ducted single-propeller model (D-SP-1), employed the basic duct (Table 3-2) with approximately 26 million meshes, and two other cases of 39 million meshes (D-SP-2) and 19 million meshes (D-SP-3), which were compared in terms of computed lift forces and FMs, as shown in Figure 3-6. A marginal difference in both lift forces and FMs is found among the three cases. Thus, we employed the mesh setting of D-SP-1 in all the other CFD simulations of ducted single-propeller models with the consideration of computer time and numerical accuracy. Besides, the criterion of numerical convergence was set to be that either the maximum residual of pressure is less than 5×10^{-5} or the maximum iteration steps is more than 3000.

The CFD simulations were further validated via comparison of the lift force generated by the propeller with EXP data [27] under the same conditions, in terms of different diameters of the cylindrical shroud surrounding the propeller, from 270 mm to 310 mm with an interval of 10 mm, and a fixed shroud height of 60 mm (with the propeller having a radius of 127 mm and a rotational velocity of 5000 rpm). As shown in Figure 3-7, the CFD results are consistent with EXP results, sharing a similar trend that the propeller-induced lift force increases linearly with an increasing gap, while being lower than that of the non-ducted propeller accompanying a notable difference, which is caused by the different propeller morphology in the models of CFDs and EXPs. Moreover, it is worth noting that a propeller–duct aerodynamic interaction exists, which may significantly affect the aero-dynamic performance of the ducted-propeller associated with lift force production and FM efficiency.

3.3.1.2 High-performance ducted design

A high-performance duct design for the single-propeller model was first explored in terms of lift force (L_{D-SP}) and FM efficiency (FM_{D-SP}) based on a variety of CFD simulations through adjusting one parameter while keeping others fixed, regarding the six parameters shown in Figure 3-2. With consideration of the limitation about duct weight, the duct volume that is proportional to duct weight was taken as an additional parameter and should be reduced as much as possible, simultaneously.

Figure 3-8 shows the correlations between aerodynamic performances (L_{D-SP} and FM_{D-SP}) and the variation of tip clearance (d_e), height difference (h_p), and diffuser angle (α). While lift force and FM efficiency show significant dependency upon tip clearance (Figure 3-8a), some maxima in L_{D-SP,d_e} and FM_{D-SP,d_e} are found at d_e = 0.001 m with other parameters fixed at h_p = 0, α = 0, h_e = 0.06 m, l_e = 0.06 m, r_e = 0.02 m, resulting in a marked increase rate of 25.1% in lift force and an increase rate of 39.1% in FM efficiency compared to those of the non-ducted single-propeller model (L_{SP} and FM_{SP}). The height difference dependency of L_{D-SP,h_p} or FM_{D-SP,h_p} (Figure 3-8b) is moderate, with their maxima around h_p = 0 accompanying other parameters fixed at d_e = 0.001 m, α = 0, h_e = 0.06 m, l_e = 0.06 m, and r_e = 0.02 m. The diffuser angle seems to affect $L_{D-SP,\alpha}$ and $FM_{D-SP,\alpha}$ (Figure 3-8c) significantly, leading to the maxima at α = 0 with other parameters fixed at d_e = 0.001 m, h_p = 0, h_e = 0.06 m, l_e = 0.06 m, and r_e = 0.02 m. It is worth noting that the variation of these three parameters hardly changes the duct volume, thus the duct volume is not taken into account for these three parameters in the current case.

Figure 3-9a shows the variations of L_{D-SP} and FM_{D-SP} in various combinations of the dimensionless diffuser length (l_e/R) and dimensionless height of ellipse inlet (h_e/R) while keeping other parameters fixed at d_e = 0.001 m, h_p = 0, α = 0, and r_e = 0.02 m. Since the duct volume varies with different combinations of l_e/R and h_e/R, we further draw a comparison between the increase rates associated with lift force (Ra_L: L_{case-i}/L_{case-1}) and duct volume (Ra_V: V_{case-i}/V_{case-1}) in Figure 3-9b among the four cases of different l_e/R and h_e/R that have large values in L_{D-SP} and FM_{D-SP} as shown in Figure 3-9a. Obviously, the duct model with $h_e/R = 0.375$ and $l_e/R = 0.25$ (h_e = 0.045 m, l_e = 0.03 m) is a high-performance duct design capable of achieving the best aerodynamic performance with a minimal duct weight based on the difference between the increase rates of lift force and duct volume (D_{Ra}: $Ra_L - Ra_V$) (Figure 3-9b). Moreover, the ducted single-propeller model with an ellipse inlet height of h_e = 0.045 m and a diffuser length of l_e = 0.03 m shows a marked improvement on aerodynamic performance with an increase rate of 24.5% in L_{D-SP} and 38.1% in FM_{D-SP} compared to L_{SP} and FM_{SP}. With respect to the r_e effect on aerodynamic performance (L_{D-SP,r_e} and FM_{D-SP,r_e}) (Figure 3-10a), while a monotonic increase is observed with increasing r_e with other parameters fixed at d_e = 0.001 m, h_p = 0, α

= 0, h_e = 0.045 m, and l_e = 0.03 m, it also results in the increase of duct volume based on the Ra_{V,r_e} $(V_{r_e,case-i}/V_{r_e,case-1})$ (Figure 3-10b). Thus, with consideration of the factors of both lift force and duct weight, we propose that the duct model with r_e = 0.02 m can be a high-performance duct design, which noticeably leads to the peak of D_{Ra,r_e} $(Ra_{L,r_e} - Ra_{V,r_e},\ Ra_{L,r_e} = L_{r_e,case-i}/L_{r_e,case-1})$.

Our results indicate that the duct can alter the propeller-induced tip vortex in a manner of duct–propeller interaction, resulting in an enhancement of lift force production in a very small value of tip clearance, which can generate an additional lift force because the pressure difference between the inner and outer surfaces of the duct can induce a suction pressure gradient on the inlet surface (Figure 3-1). However, such propeller–duct aerodynamic interactions will be weakened with increasing tip clearance (d_e), substantially approaching the lift force production of a non-ducted single propeller model (L_{SP}). Besides, the variations of other parameters can also alter the propeller-induced tip vortices or wake contraction (Figure 3-1) due to the duct–propeller interaction, and thus affect the aerodynamic lift force production and FM efficiency. These results are supported by the visualized flow fields and pressure distributions (Figure 3-11) of the non-ducted single propeller model and the high-performance ducted single-propeller model, where the downwash in the ducted-propeller model is weakened compared to that in the non-ducted model (Figure 3-11a), which results in reducing the propeller-induced lift force, whereas the pressure gradient on the inlet surface augments the lift force production by the duct. Thus, the duct leads to improving the total lift force production in the ducted-propeller model. Obviously, the aerodynamic interaction between the propeller and duct plays a crucial role in dominating the tip vortex, the downwash, and the wake topology, exhibiting distinguished features at the tip-gap between the propeller and duct. Thus, the duct enables a significant suppression of the tip vortex while forming a highly contracted yet intense downward jet below the propeller, leading to the enhancement of aerodynamic performance.

Thus, the high-performance duct design in the ducted single-propeller model is defined with a combination of d_e = 0.001 m, h_p = 0, α = 0, h_e = 0.045 m $(h_e/R = 0.375)$, l_e = 0.03 m $(l_e/R = 0.25)$, and r_e = 0.02 m $(r_e/R = 0.167)$ (Table 3-2), which enables a marked improvement in aerodynamic performance with an increase rate of 24.5% in lift force production (3.873N) and an increase rate of 38.1% in FM efficiency (0.884) compared to that in the non-ducted single propeller model. This duct model is subsequently employed in all the ducted multi-propeller models for investigating the configuration effect on aerodynamic performance.

3.3.2 Effect of ducted multi-propeller configuration

In section 2.3.3, we carried out an extensive study on the effect of a non-ducted multi-propeller configuration on aerodynamic performance in a quadrotor drone, where a combination of tip distance, d = 0.185 m (d/R = 1.54) and height difference, h = 0.24 m (h/R = 2.0) identical to the maximum multi-propeller configuration in Figure 1-6 was found capable of achieving the optimal aerodynamic performance. The optimal configuration achieved the greatest increase rate of 9% in lift force compared with the basic non-ducted multi-propeller configuration under a hovering state. Here, with a series of CFD-based simulations, we intend to examine the effect of a ducted multi-propeller configuration on aerodynamic performance in the quadrotor drone. We employ the high-performance duct model obtained in section 3.3.1 and conduct a systematic parameter study through adjusting the tip distance ($0.46 \leq d/R \leq 1.54$) and height difference ($0 \leq h/R \leq 2.0$) over a broad range between the maximum multi-propeller configuration and the minimum multi-propeller configuration as depicted in Figure 3-3, where the ducted maximum multi-propeller configuration has a combination of d = 0.185 m (d/R = 1.54) and h = 0.24 m (h/R = 2.0) while the minimum one consists of d = 0.055 m (d/R = 0.46) and h = 0 m (h/R = 0) that is confirmed to be capable of avoiding the ducted multi-propeller interference. In the end, the CFD-based simulations corresponding to 22 randomly selected combinations as summarized in Table 3-3 are performed.

The modeling validity was first investigated in terms of mesh-dependency associated with the ducted basic multi-propeller configuration (D-BMP), the ducted maximum multi-propeller configuration with d/R = 1.54 and h/R = 2.0 (D-MMP), and the ducted sub-maximum multi-propeller configuration with d/R = 1.54 and h/R = 0 (D-SMP) as illustrated in Figure 3-12. We confirmed that a grid system with 48 million meshes could ensure a good balance between sufficient numerical accuracy and computation time and thus was used for all the CFD-based ducted multi-propeller simulations. Furthermore, we found that the ducted multi-propeller models in all the multi-propeller configurations show better aerodynamic performance than the non-ducted multi-propeller models with increase rates of lift force and FM efficiency of 7.0% and 9.7% in D-BMP, 15.5% and 24.0% in D-MMP, and 17.7% and 28.0% in D-SMP, respectively. This is also consistent with previous work [29,30].

The effect of ducted multi-propeller configurations was investigated by analyzing the aerodynamic performance associated with lift force (L_{D-MP}) and FM efficiency (FM_{D-MP}) through adjusting the height difference and tip distance. The height-difference effect was examined as illustrated in Figure 3-13a through decreasing the dimensionless height difference (h/R) with the tip distance fixed. The L_{D-MP} obviously displays some optimal peaks with an increase rate of 1.7% at h/R = 0.5 with a fixed tip distance at d_{max}, and 0.4% at h/R = 1.5 with a fixed tip distance at d_{min}, compared to that in the ducted maximum multi-propeller configuration, resulting in the increase rates of 3.9% and 1.7% in FM_{D-MP} at the same points, respectively. This indicates that the L_{D-MP} and FM_{D-MP} can be improved at h/R within a range of 0.5 to 1.5 with the tip distance fixed, particularly when the tip distance is fixed at a larger value. This is probably because the aerodynamic interactions between the lower and upper ducted propellers can enhance the lift force production owing to the increase in induced velocity in the ducted propellers positioned lower when h/R varies from 0.5 to 1.5. On the other hand, the tip-distance effect of ducted multi-propeller configurations seems to be small at various dimensionless tip distances (d/R) with the height difference fixed (Figure 3-13b): The L_{D-MP} and FM_{D-MP} show a marginal variation. This indicates that the tip-distance-induced aerodynamic interaction merely has effect in impairing aerodynamic performance within a narrow range of d/R from 0.82 to 0.46 but is negligible over a range of d/R from 1.54 to 0.82.

These results are supported by the visualized flow structures of different ducted multi-propeller configurations at cross-sections of y/R = 1.708 (y = 0.205 m) and 1.183 (y = 0.142 m), the planes in which the centers of propellers P1 and P2 are located as illustrated in Figures 3-14 and 3-15, as well as the pressure distributions of different ducted multi-propeller configurations on the suction side as shown in Figure 3-16. The interaction between the upper and lower positioned ducted-propellers at the appropriate height difference is effective and enables one to improve the induced velocity of lower propellers (h/R = 0.5 in Figure 3-14) as well as the pressure gradient on the duct inlet surface (h/R = 0.5 in Figures 3-15 and 3-16) with the tip distance fixed. This is beneficial to improve the lift force production, whereas this interaction weakens at h/R = 0 and 2.0 due to the lack of height difference and the too-large distance of the height difference. The interaction among ducted propellers counteracts each other and impairs the downwash-jet because of the interference among them when the tip distance is small with the height difference fixed (Figure 3-14), which is harmful to the wake velocity and pressure gradient on propeller and duct surfaces (Figures 3-15 and 3-16). Hence, this suppresses the lift force production on the propeller and duct, whereas this interaction is negligible when the tip distance is large because of the downwash-jet separation and interference avoidance owing to the large distance of ducted propellers. In other words, the aerodynamic performance of the ducted multi-propeller can be improved with an appropriate height difference and retained by decreasing the tip distance to a minimal value, which is useful to explore the ducted optimal multi-propeller configuration.

3.3.3 Optimization of ducted multi-propeller configuration

Optimization of the ducted multi-propeller configuration was finally explored based on the L_{D-MP} obtained from various configurations through combining a novel surrogate model with a set of CFD-based simulations. Considering that FM_{D-MP} shares a similar variation trend with L_{D-MP}, we thus limited our approach merely to the lift force optimization. As a consequence, the objective function associated with the optimization procedure is defined as:

$$\begin{cases} Max\ L_{D-MP} \\ s.t.\ 0 \leq h/R \leq 2.0, 0.46 \leq d/R \leq 1.54 \end{cases} \quad (3\text{-}9)$$

In addition to the CFD-based results of the 22 cases of various multi-propeller configurations conducted in section 3.3.2, we further performed an additional 13 cases of CFD simulations to ensure a sufficiently smooth spatial surface of the objective function and hence, an accurate estimation of L_{D-MP}, which are summarized in Table 3-4 and eventually constituted the design space consisting of 35 cases of CFD simulations in total in this process.

As shown in Figure 3-17, other than the lift force obtained merely in some discrete points by the CFD simulations because the high fidelity CFD simulation is computationally expensive, the surrogate model method combined with finite CFD-based results is capable of predicting the lift force at each point consecutively and quickly (continuous spatial surface/function) while exploring the optimal lift force accurately and comprehensively in a broad parametric space. The interpolation points and optimal observed points selected in the surrogate modeling are shown in Figure 3-17a, where the boundary of the observed points is limited to the vicinity of the interpolation points marked with the red dashed frame in the manner of random selection to determine the optimal observed points. The surrogate model-based results utilizing the RBFs model method with the IMQ function are shown in Figures 3-17b and 3-17c, where the blue cross marker "+" denotes the maximum L_{D-MP} of the surrogate model-based results, while the red cross marker "+" represents the maximum L_{D-MP} of the CFD-based results. Figure 3-17c also exhibits the good fit of the lift force attained from the surrogate model- and CFD-based results, which thus validates the surrogate model-based simulation simultaneously. The comparison among the results as summarized in Table 3-5 further indicates that an optimal ducted multi-propeller configuration for aerodynamic performance is achieved with d/R = 0.925 and h/R = 0.92, which is almost identical to the configuration obtained from the CFD-based results with a configuration of d/R

= 1.0 and h/R = 1.0. Moreover, the surrogate model-based result displays that the L_{D-MP} of the ducted optimal multi-propeller configuration can achieve an improvement with an increase rate of 2.1% compared to that of the ducted maximum multi-propeller configuration, and a further increase rate of 17.7% compared to that of the ducted basic multi-propeller configuration. Our results thus point out an optimal and compact ducted multi-propeller configuration design with a minimal tip distance and an appropriate height difference with respect to quadrotor drones, which is capable of markedly improving the aerodynamic performance compared with the ducted maximum multi-propeller configuration, resulting from the least interference among adjacent ducted-propellers and the maximum positive interaction among upper and lower ducted-propellers.

Table 3-2 Morphology parameters in the basic duct model and the high-performance duct model

	d_e (m)	h_p (m)	α (°)	h_e/R	l_e/R	r_e/R
Basic duct	0.001	0	0	0.5	0.5	0.167
High-performance duct	0.001	0	0	0.375	0.25	0.167

Table 3-3 Parameters of *h/R* and *d/R* for 22 CFD simulations in various ducted multi-propeller configurations

h/R	***d/R***							
h/R = 2.0	1.54	1.40	1.18	1.00	0.82	0.68	0.53	0.46
h/R = 1.5	1.54	–	–	–	–	–	–	0.46
h/R = 1.0	1.54	–	–	–	–	–	–	0.46
h/R = 0.5	1.54	–	–	–	–	–	–	0.46
h/R = 0.0	1.54	1.40	1.18	1.00	0.82	0.68	0.53	0.46

Table 3-4. Additional 13 cases of CFD simulations in surrogate model-based optimization procedure regarding ducted rotor-configuration

h/R	***d/R***							
h/R = 1.5	–	–	1.18	–	–	0.68	–	–
h/R = 1.0	–	1.40	–	1.00	0.82	–	0.53	–
h/R = 0.6	1.54	1.40	–	–	–	–	0.53	0.46
h/R = 0.5	–	–	1.18	–	0.82	0.68	–	–

Table 3-5 Lift forces of ducted optimal multi-propeller (optimal L_{D-MP}) based on CFD simulation and surrogate modeling

	Surrogate modeling	**CFD simulation**
Optimal $\boldsymbol{L_{D-MP}}$	14.611 N	14.605 N
Dimensionless value of d/R & h/R at optimal $\boldsymbol{L_{D-MP}}$	d/R = 0.925 (d = 0.111m), h/R = 0.92 (h = 0.110m)	d/R = 1.0 (d = 0.120m), h/R = 1.0 (h = 0.120m)
Increase rate of optimal $\boldsymbol{L_{D-MP}}$ compared to $\boldsymbol{L_{D-MMP}}$	1.95%	1.90%
Increase rate of Optimal $\boldsymbol{L_{D-MP}}$ compared to $\boldsymbol{L_{BMP}}$	17.79%	17.74%
Remarks	Optimal c =3.3; R^2 = 0.9465, $\bar{e}$ = 0.0015, σ_e = 0.0022.	

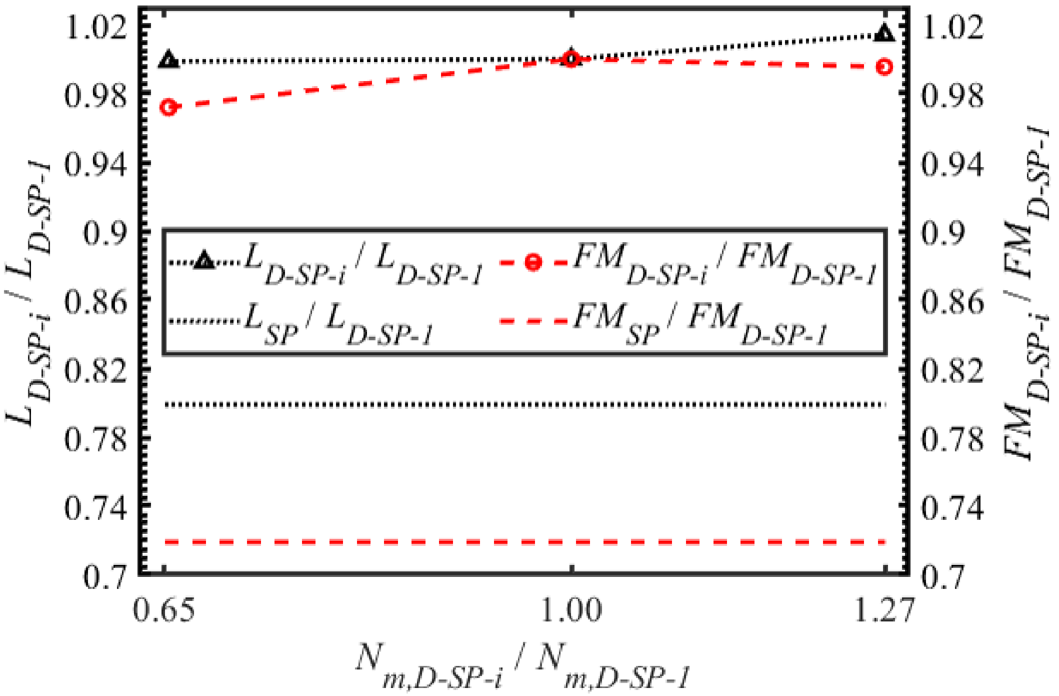

Figure 3-6 Comparison of lift forces and FMs among three grid systems in the ducted single-propeller model (N_m: Mesh number; L_{SP} = 3.11N, FM_{SP} = 0.64 [33]).

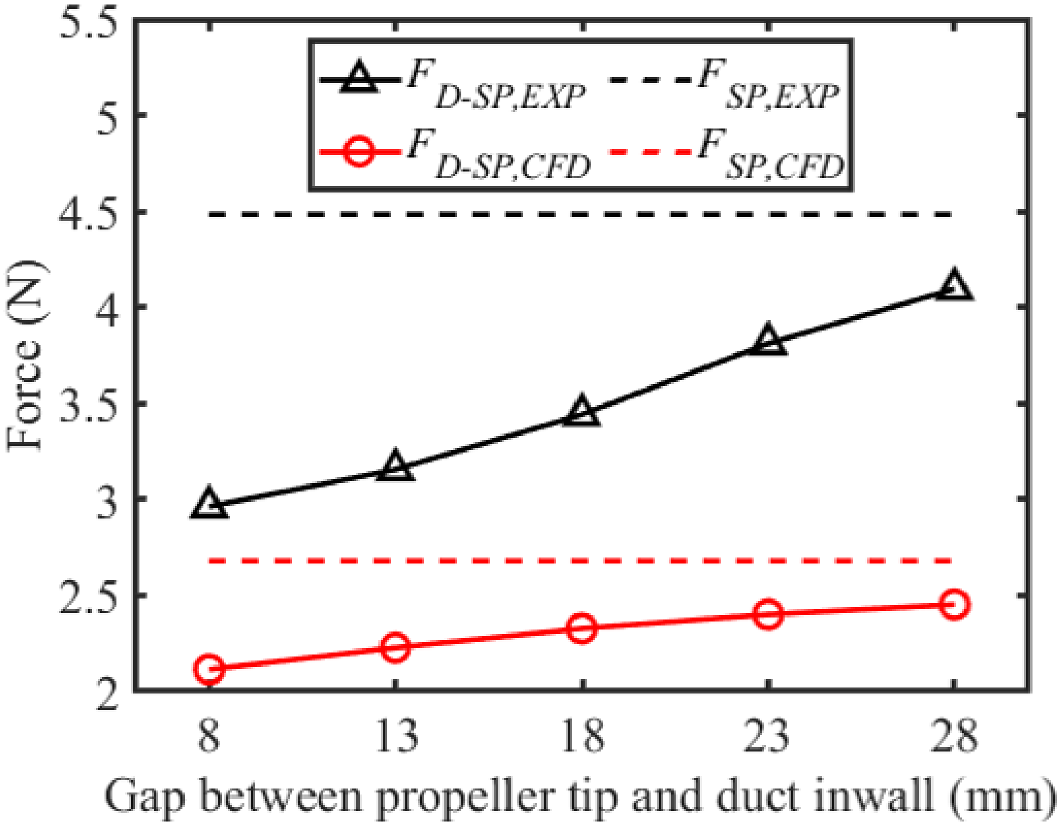

Figure 3-7 Comparison of lift forces between CFD and EXP [27] in the ducted single-propeller model. $F_{D-SP,EXP}$ and $F_{D-SP,CFD}$, lift force generated by propeller in the ducted single-propeller model (EXP and CFD); $F_{SP,EXP}$ and $F_{SP,CFD}$, lift force generated by propeller in the non-ducted single-propeller model (EXP and CFD).

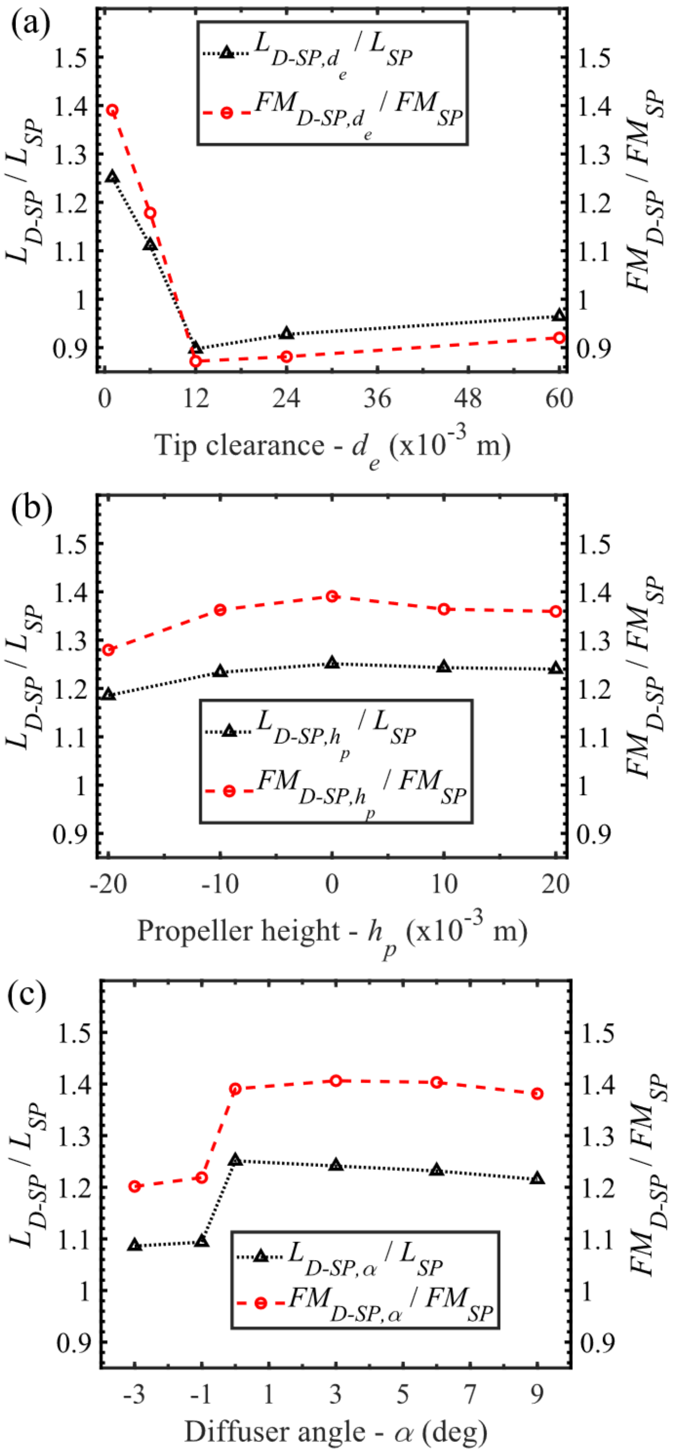

Figure 3-8 Lift force and FM efficiency vs. (a) tip clearance (d_e) (L_{D-SP,d_e} and FM_{D-SP,d_e}), (b) height difference (h_p) (L_{D-SP,h_p} and FM_{D-SP,h_p}), and (c) diffuser angle (α) ($L_{D-SP,\alpha}$ and $FM_{D-SP,\alpha}$) in the ducted single-propeller model. L_{SP} and FM_{SP} denote the lift force and FM efficiency in the non-ducted single-propeller model, respectively.

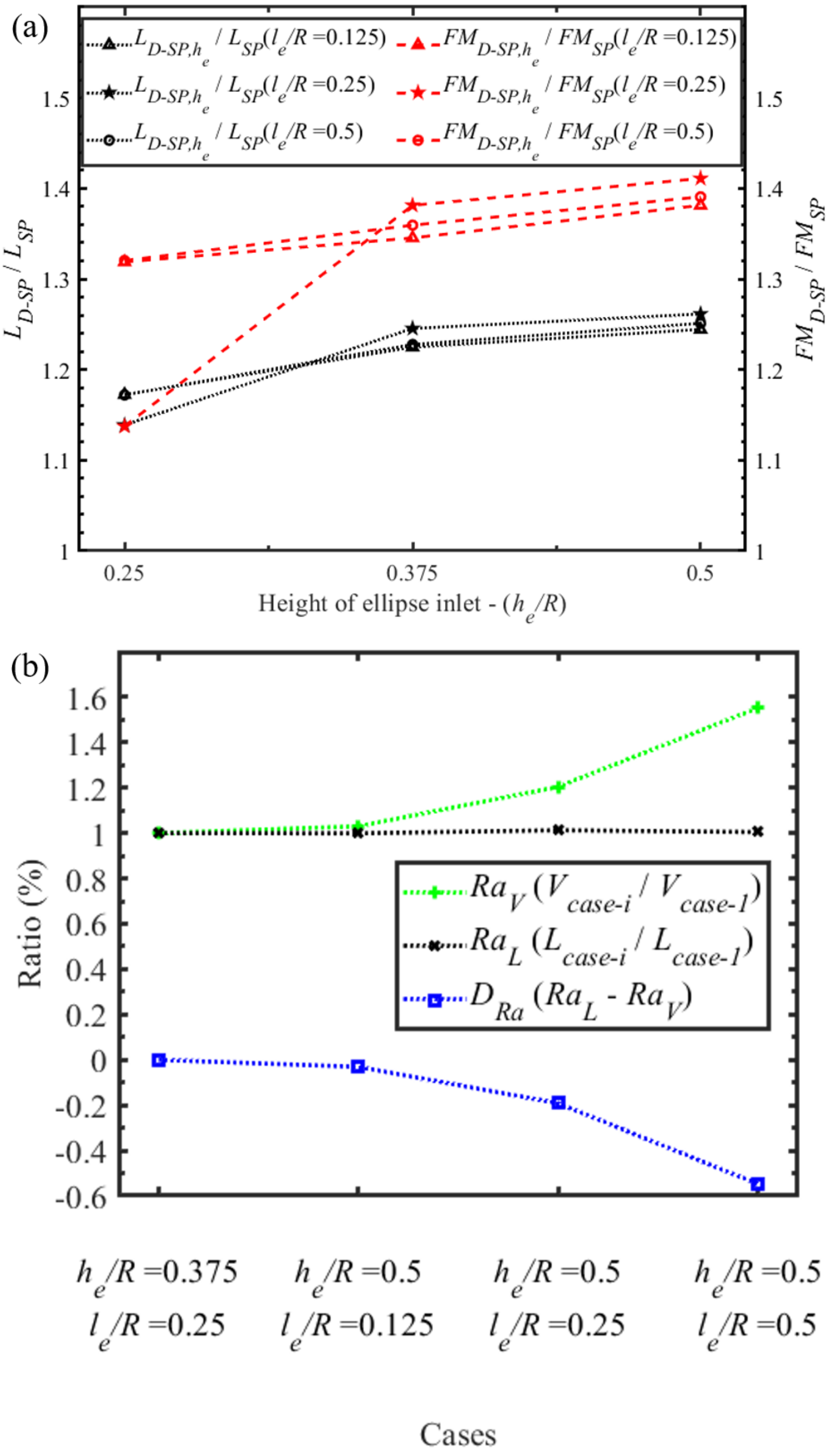

Figure 3-9 (a) Lift force and FM efficiency (L_{D-SP,h_e} and FM_{D-SP,h_e}) vs. h_e/R with l_e/R fixed in different values in the ducted single-propeller model; (b) increase rates of duct volume and lift force vs. h_e/R and l_e/R.

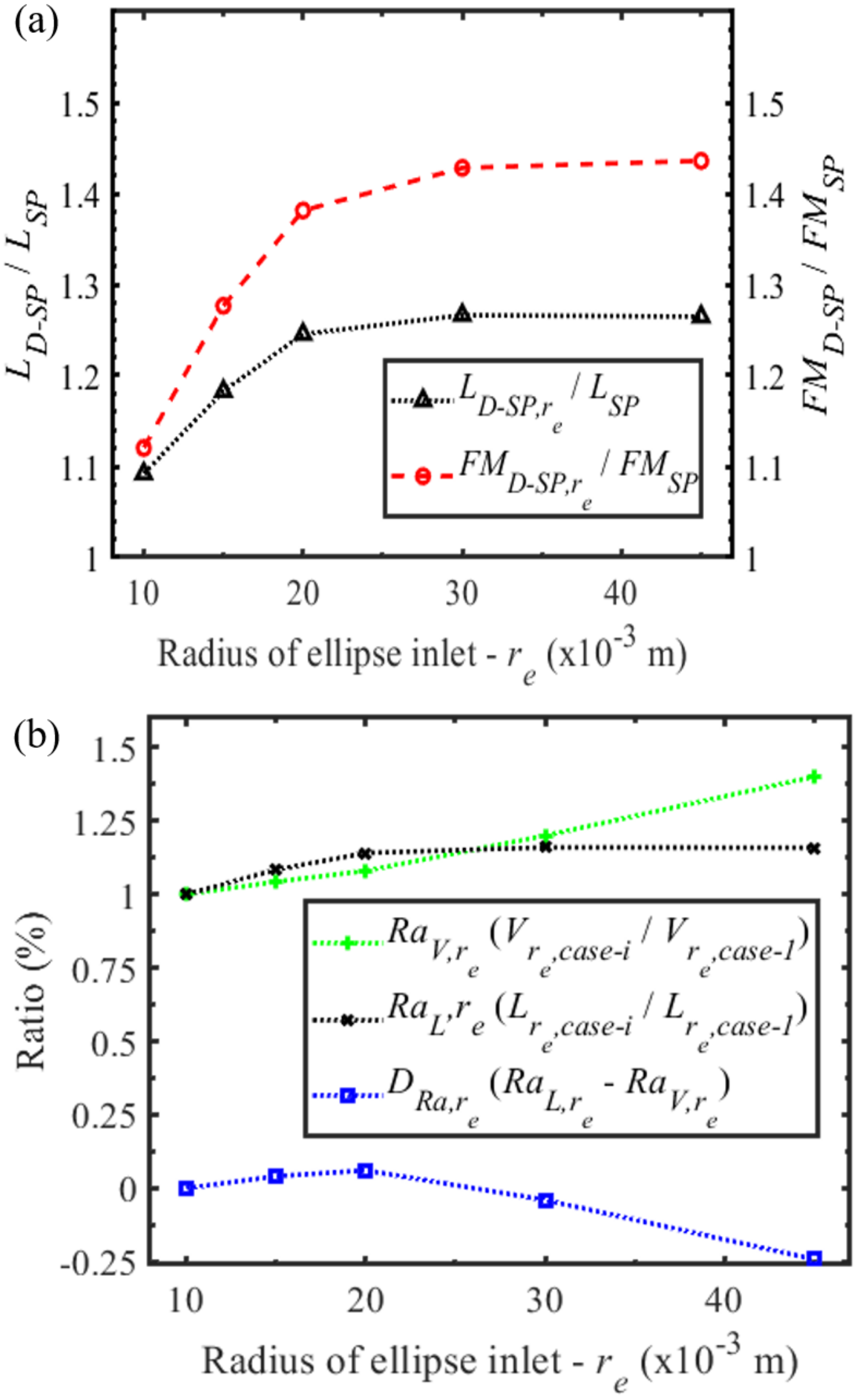

Figure 3-10 (a) Lift force and FM efficiency (L_{D-SP,r_e} and FM_{D-SP,r_e}) vs. r_e in the ducted single-propeller model; (b) increase rates of duct volume and lift force vs. r_e.

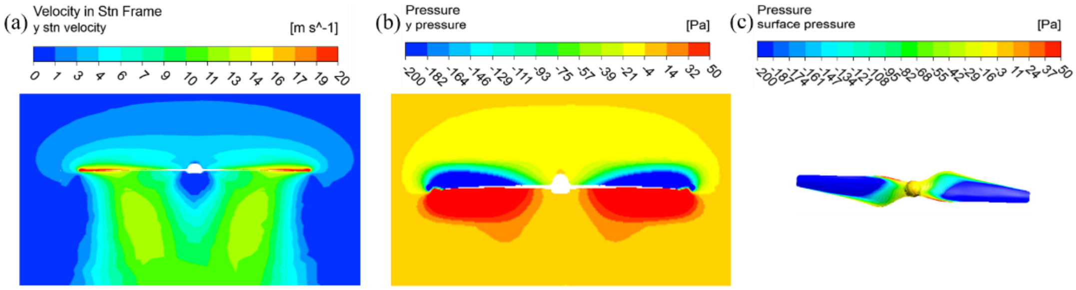

Non-ducted propeller **Non-ducted propeller** **Non-ducted propeller**

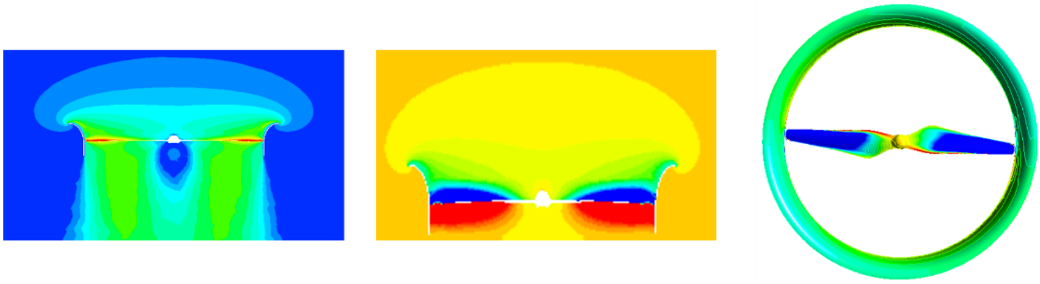

High-performance ducted-propeller **High-performance ducted-propeller** **High-performance ducted-propeller**

Figure 3-11 Comparison of flow structures and pressure distributions between the non-ducted and high-performance ducted single propeller model. (a) Iso-speed contours and (b) pressure contours at the cross-section of $y = 0$ m, and (c) pressure contours at the suction side.

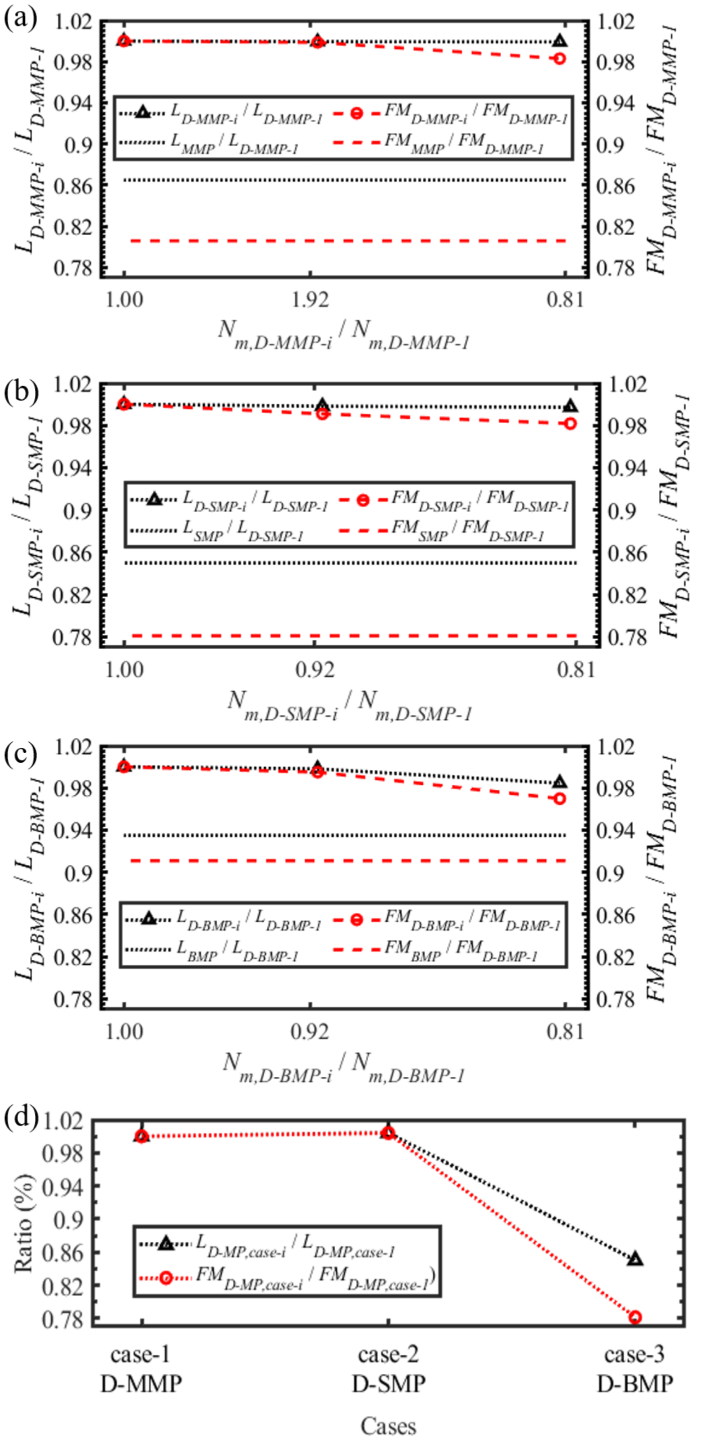

Figure 3-12 Grid sensitivity and ratio on aerodynamic performances in different ducted multi-propeller configurations. (a) D-MMP configuration (N_m , number of meshes); (b) D-SMP configuration; (c) D-BMP configuration; (d) ratio of aerodynamic performances in different ducted multirotor configurations compared to that in D-MMP configuration.

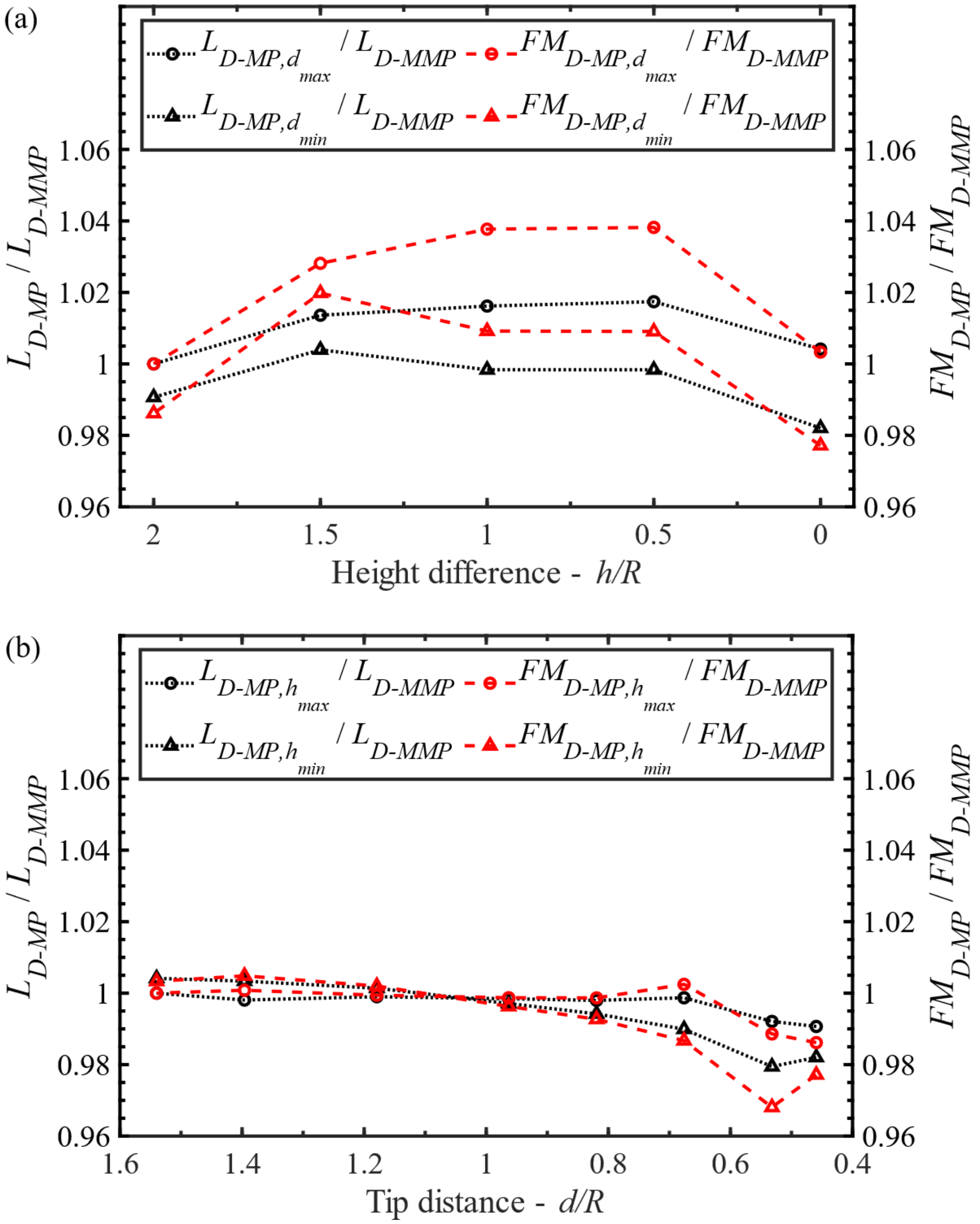

Figure 3-13 (a) Lift force and FM efficiency vs. h/R in various ducted multi-propeller configurations: $L_{D-MP,d_{max}}$ and $FM_{D-MP,d_{max}}$ with d_{max} fixed and $L_{D-MP,d_{min}}$ and $FM_{D-MP,d_{min}}$ with d_{min} fixed. (b) Lift force and FM efficiency vs. d/R in various ducted multi-propeller configurations: $L_{D-MP,h_{max}}$ and $FM_{D-MP,h_{max}}$ with h_{max} fixed and $L_{D-MP,h_{min}}$ and $FM_{D-MP,h_{min}}$ with h_{min} fixed.

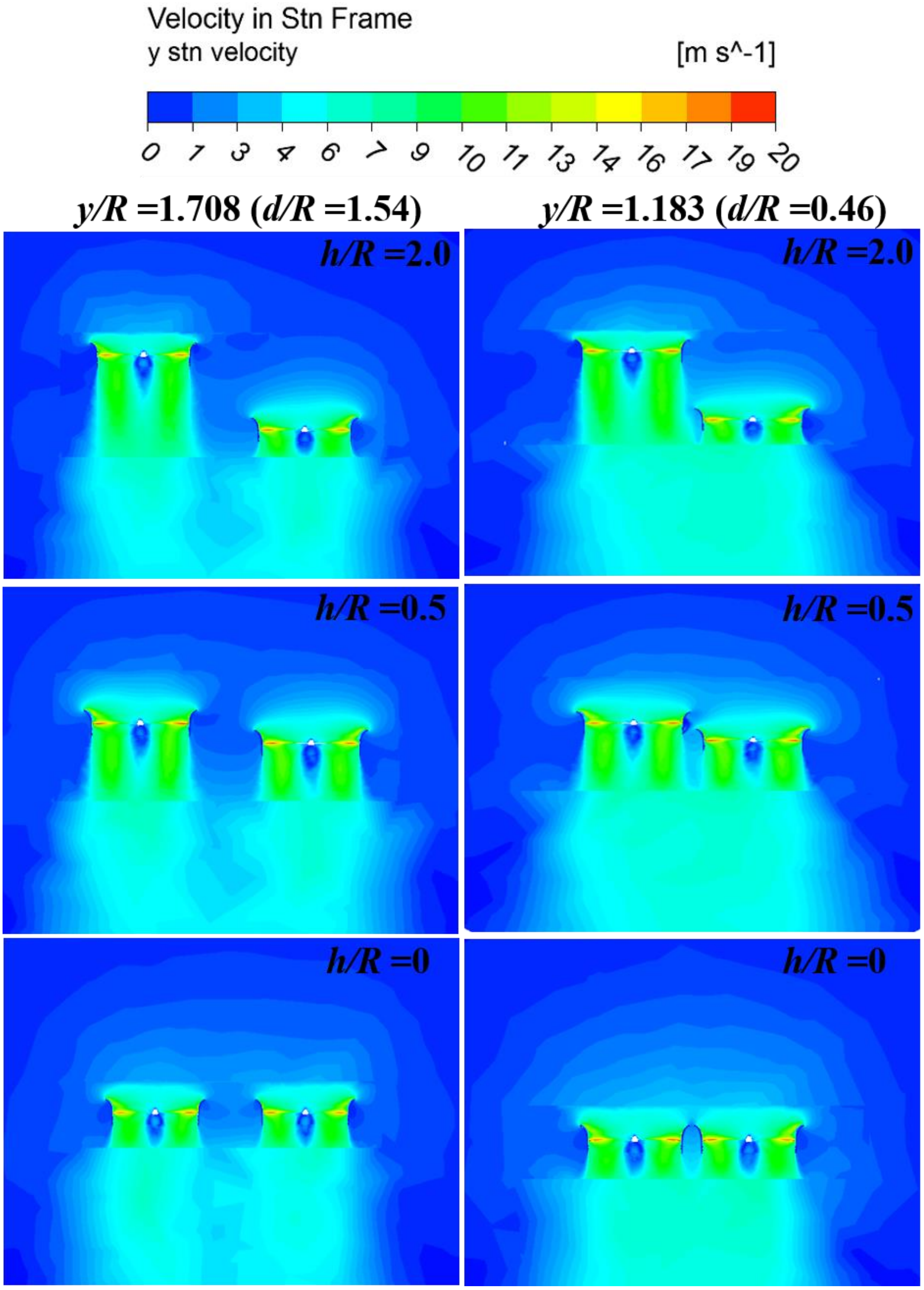

Figure 3-14 Iso-speed contours in various ducted multi-propeller configurations at cross-sections of y/R = 1.708 and 1.183.

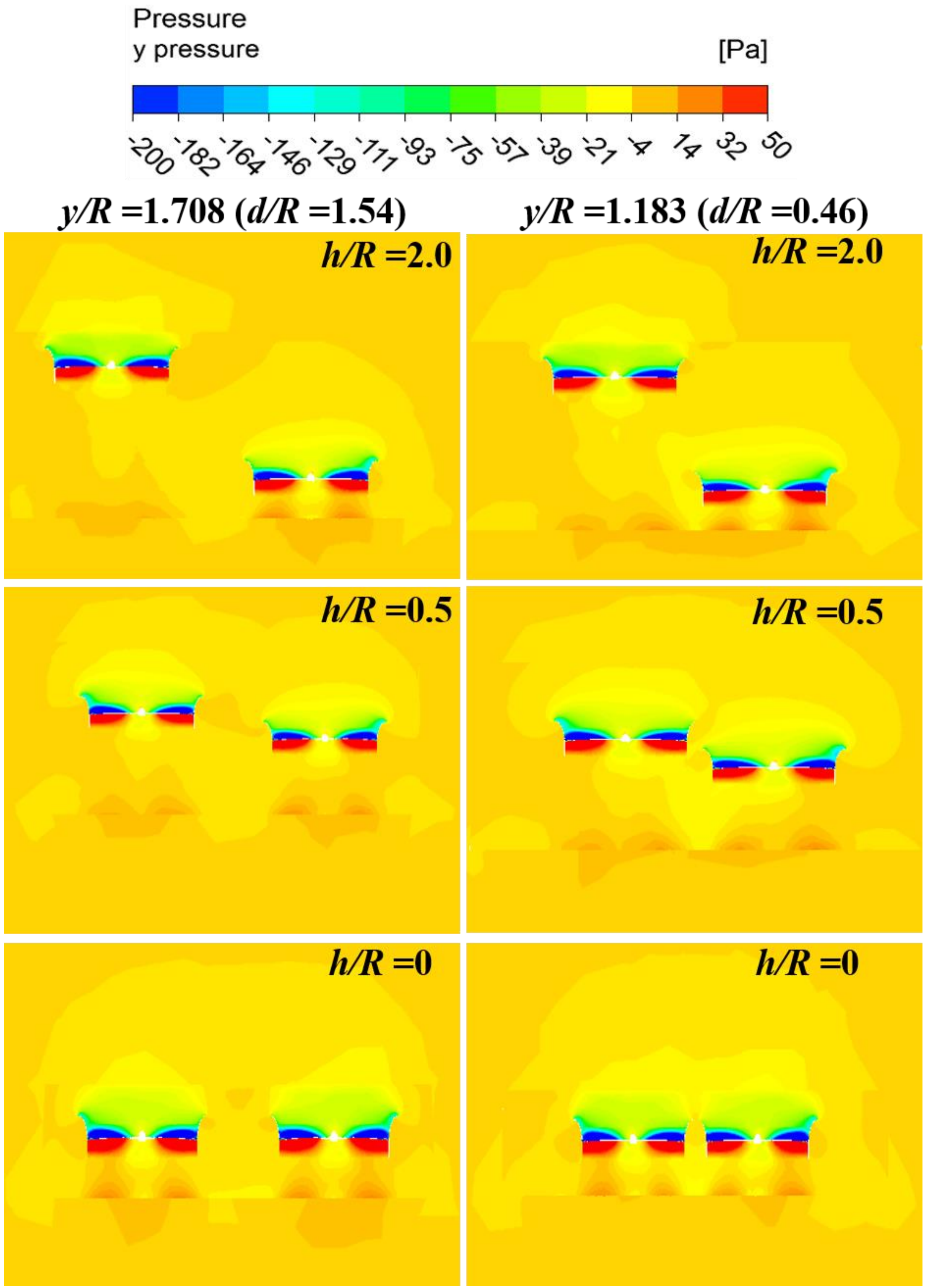

Figure 3-15 Pressure contours in various ducted multi-propeller configurations at cross-sections of y/R = 1.708 and 1.183.

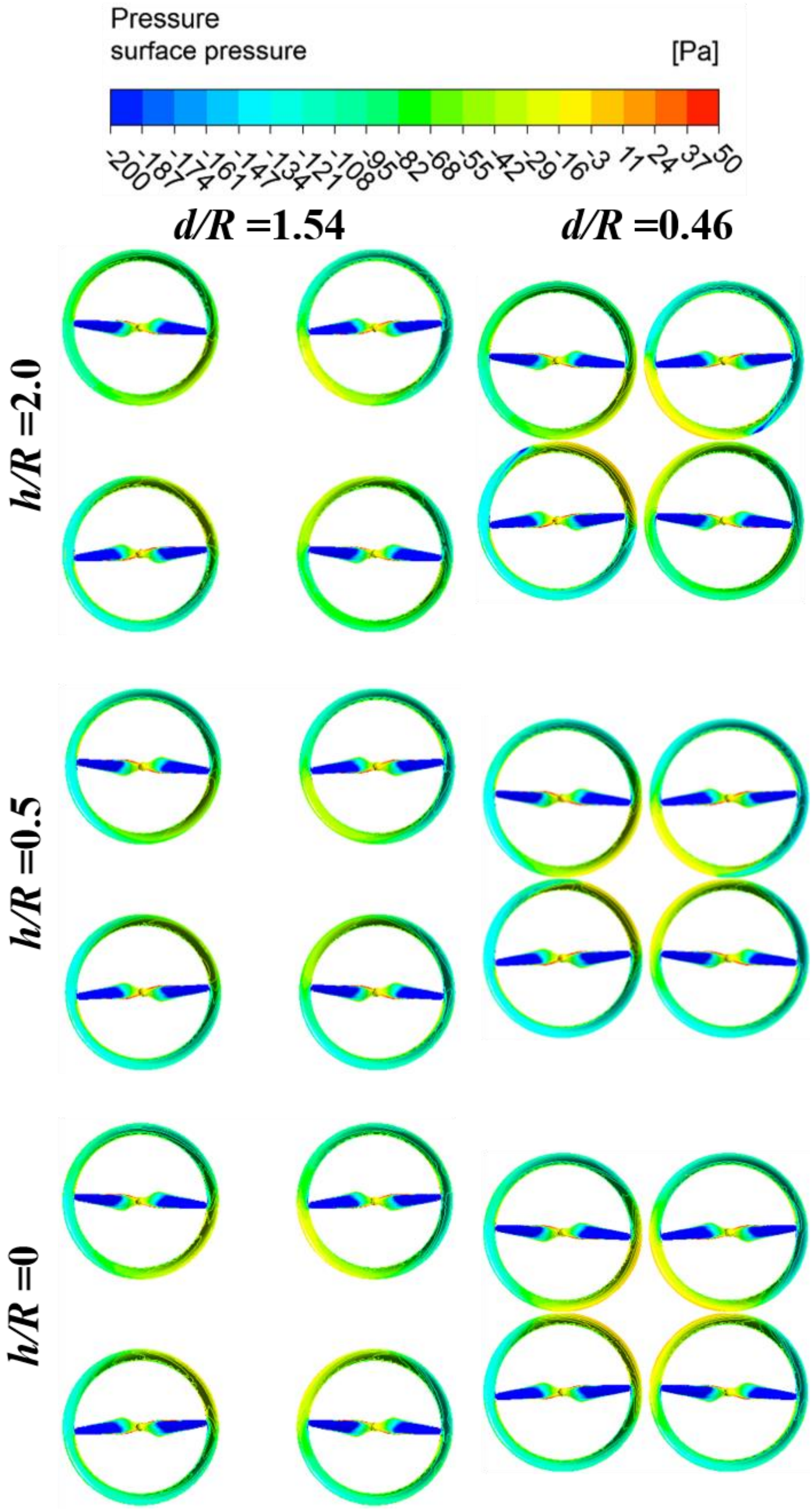

Figure 3-16 Pressure distributions at the suction side in various ducted multi-propeller configurations.

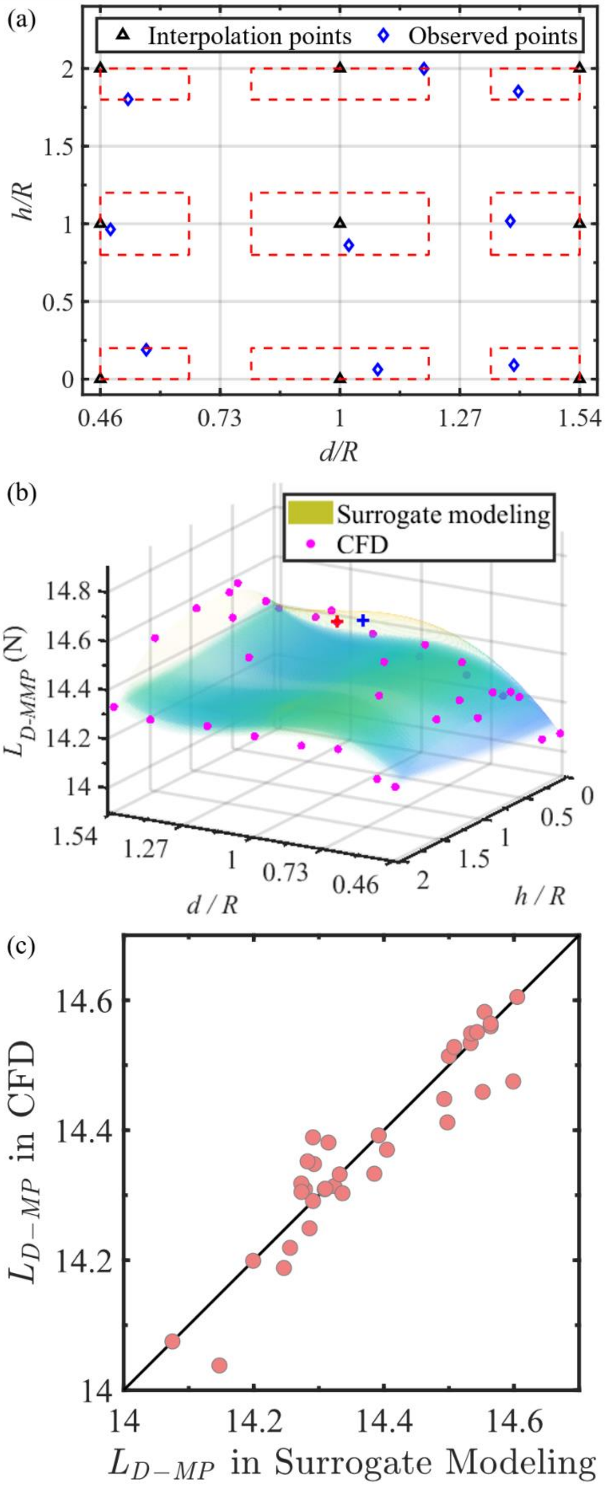

Figure 3-17 Surrogate model-based results for ducted rotor-configuration: (a) interpolation points and observed points, (b-c) comparison of CFD-based results and surrogating model-based results.

3.4 Conclusions

In this chapter, in order to refine the performance of quadrotor drone with the optimal rotor-configuration but large frame, we further conceived a ducted-propeller design for the modification. Thus, we have conducted a systematic analysis of the effect of the ducted multi-propeller configuration on lift force production and FM efficiency while exploring an optimal design of ducted multi-propeller configuration through a combination of CFD-based simulations and a surrogate model. Our main findings are summarized as follows:

A high-performance ducted single-propeller design was found, capable of achieving an increase rate of 24.5% in lift force production and 38.1% in FM efficiency compared to the original non-ducted single-propeller model. The ducted multi-propeller configuration model equipped with the high-performance duct design enables a marked improvement in both lift force production and FM efficiency with increase rates of 15.5% and 24.0% in the maximum configuration, 17.7% and 28.0% in the sub-maximum configuration, and even 7.0% and 9.7% in the basic configuration. Our results demonstrate that ducted propellers can significantly improve both lift force production and FM efficiency of multirotor copters compared to non-ducted multirotor copters.

The aerodynamic interaction among ducted multi-propellers shows notable dependency upon two key parameters, the tip distance and height difference between propellers, and thus can be optimized in terms of the ducted multi-propeller configuration. The tip distance has a marginal impact on aerodynamic performances over a range of 0.185 m (d/R = 1.54) to 0.098 m (d/R = 0.82) but impairs the aerodynamic performance within a narrow range (0.82 $\geq d/R \geq$ 0.46) with height difference fixed; adjustment of the height difference with tip distance fixed can also improve aerodynamic performance over a certain range of h/R from 1.5 to 0.5.

Through combining CFD-based simulations and a surrogate model to determine the effect of the ducted multi-propeller configuration on aerodynamic performance in the quadrotor drone, we found an optimal design of the ducted multi-propeller configuration under the conditions of a minimal tip distance and a specific height difference, which is capable of enabling the maximization of the aerodynamic interaction while reducing the multirotor frame, resulting in an increase rate of about 2% in lift force production and 4% in FM efficiency compared to the original ducted multi-propeller configuration. What's more, a ducted rotor-configuration experiment has also been conducted to validate the results obtained from numerical simulations exclusively. Based on the experiment on ducted rotor-configurations with the 3D printing high-performance ducts, its results fit well with the results from simulations, which certifies the correctness and practicability of the findings of optimal ducted rotor-configuration.

In conclusion, inspired by a biomimetic design of multi-rotor configuration obtained in section 2.3.3, for the sake of improvement in lift force production and FM efficiency, we demonstrate that some optimal adjustment associated with tip distance and height difference can also benefit the aerodynamic performance of the ducted multi-propeller configuration associated with a multirotor drone. How the current optimal ducted multi-propeller configuration design works in multirotor copters with larger and/or smaller propellers, and how it impacts flight stability and maneuverability, remain unclear and will be our future task.

Reference

[1] Roldan, J.J.; Del Cerro, J.; Barrientos, A. A proposal of methodology for multi-UAV mission modeling. *In Proceedings of the 23rd Mediterranean Conference on Control and Automation (MED)*, Torremolinos, Spain, 16–19 June 2015; pp. 1–7.

[2] Bousbaine, A.; Wu, M.H.; Poyi, G.T. Modelling and simulation of a quad-rotor helicopter. *In Proceedings of the 6th IET International Conference on Power Electronics, Machines and Drives (PEMD 2012)*, Bristol, UK, 27–29 March 2012.

[3] Roldan, J.J.; Sanz, D.; Del Cerro, J.; Barrientos, A. Lift Failure Detection and Management System for Quadrotors. In *ROBOT2013: First Iberian Robotics Conference*; Springer: Cham, Switzerland, 2014; Volume 252, pp. 103–114.

[4] Otsuka, H.; Nagatani, K. Thrust Loss Saving Overlapping Rotor Arrangement on Small Multirotor Unmanned Aerial Vehicles. *In Proceedings of the 2016 IEEE International Conference on Robotics and Automation (ICRA)*, Stockholm, Sweden, 16–21 May 2016.

[5] Ampatis, C.; Papadopoulos, E. Parametric design and optimization of multi-rotor aerial vehicles. *Proc.-IEEE Int. Conf. Robot Autom*. 2014, *30*, 6266–6271.

[6] Hoffmann, G.M.; Huang, H.; Waslander, S.L.; and Tomlin, C.J. Quadrotor helicopter flight dynamics and control: Theory and experiment. *AIAA Guid. Navig. Control. Conf.* 2007, *2007*, 1670–1689.

[7] Theys, B.; Dimitriadis, G.; Hendrick, P.; and De Schutter, J. Influence of propeller configuration on propulsion system efficiency of multi-rotor Unmanned Aerial Vehicles. *In Proceedings of the 2016 International Conference on Unmanned Aircraft Systems (ICUAS)*, Arlington, VA, USA, 7–10 June 2016; pp. 195–201.

[8] Shukla, D.; Komerath, N. Multirotor drone aerodynamic interaction investigation.

Drones 2018, *2*, 1–13.

[9] Yao, L.; Wang, J.L. Aerodynamic Performance of Quadrotor UAV with Non-Planar Rotors. *Appl. Sci.* 2019, *9*, 2779.

[10] Hrishikeshavan, V.; Black, J.; Chopra, I. Design and performance of a quad-shrouded rotor micro air vehicle. *J. Aircr*. 2014, *51*, 779–791.

[11] Hrishikeshavan, V.; Black, J.; Chopra, I. Design and testing of a quad shrouded rotor micro air vehicle in hover. *In Proceedings of the 53rd AIAA/ASME/ASCE/AHS/ASC Structures, Structural Dynamics and Materials Conference*, Honolulu, HI, USA, 23–26 April 2012.

[12] Hrishikeshavan, V.; Black, J.; Chopra, I. Development of a quad shrouded rotor micro air vehicle and performance evaluation in edgewise flow. *Annu. Forum. Proc.-AHS* 2012, *1*, 665–684.

[13] Liu, H.; Ravi, S.; Kolomenskiy, D.; and Tanaka, H. Biomechanics and biomimetics in insect-inspired flight systems. *Philos. Trans. R. Soc. B Biol. Sci*. 2016, *371*, 20150390.

[14] Liu, H.; Nakata, T.; Gao, N.; Maeda, M.; Aono, H.; Shyy, W. Micro air vehicle-motivated computational biomechanics in bio-flights: Aerodynamics, flight dynamics and maneuvering stability. *Acta Mech. Sin Xuebao* 2010, *26*, 863–879.

[15] Cheng. B.; Deng, X.; Hedrick, T.L. The mechanics and control of pitching manoeuvres in a freely flying hawkmoth (Manduca sexta). *J. Exp. Biol*. 2011, *214*, 4092–4106.

[16] Altshuler, D.L.; Quicazán-Rubio, E.M.; Segre, P.S.; and Middleton, K.M. Wingbeat kinematics and motor control of yaw turns in Anna's hummingbirds (Calypte anna). *J. Exp. Biol*. 2012, *215*, 4070–4084.

[17] Maeda, M.; Nakata, T.; Kitamura, I.; Tanaka, H.; Liu, H. Quantifying the dynamic wing morphing of hovering hummingbird. *R. Soc. Open Sci*. 2017, *4*, 170307.

[18] Cheng, B.; Tobalske, B.W.; Powers, D.R.; Hedrick, T.L.; Wethington, S.M.; Chiu, G.; Deng, X. Flight mechanics and control of escape manoeuvres in hummingbirds. I. Flight kinematics. *J. Exp. Biol*. 2016, *219*, 3518–3531.

[19] Liu H, Wang X, Nakata T, Yoshida K. Aerodynamics and flight stability of a prototype flapping micro air vehicle. *2012 ICME Int Conf Complex Med Eng C, 2012 Proc*. 2012:657–62. https://doi.org/10.1109/ICCME.2012.6275676.

[20] Kuantama, E.; Tarca, R. Quadcopter thrust optimization with ducted-propeller. *MATEC Web Conf.* 2017, *126*, 1–4.

[21] Vogel, C.R.; Willden, R.H.J. Improving Tidal Turbine Performance Through Multi-Rotor Fence Configurations. *J. Mar. Sci. Appl*. 2019, *18*, 17–25.

[22] Lu, Z.; Liu, Y.; Debiasi, M.; and Khoo, B.C. Acoustic characteristics of a multi-rotor

MAV and its noise reduction technology. *In Proceedings of the 45th International Congress and Exposition of Noise Control Engineering*, Hamburg, Germany, 21–24 August 2016; pp. 725–735.

[23] Arkhipov, M.; Serokhvostov, S.; Stremousov, K. Numerical and Experimental Investigation of Ducted Fans Interference for Multirotor Copter-type Aerial Vehicle. *In Proceedings of the 7th European Conference for Aeronautics and Aerospace Science (EUCASS)*, Milan, Italy, 3–7 July 2017.

[24] Stremousov, K.; Arkhipov, M. Study of ducted fans interference for copter type multirotor UAV/RPAS. *In Proceedings of the International Micro Air Vehicle Conference and Flight Competition (IMAV)*, Toulouse, France, 18 September 2017; pp. 17–22.

[25] Chua, J.C.; Loveranes, A.; MacAndog, L.A.; Reyes, R.M.; Augusto, G.L.; Lim, L.A.G. Design of a shrouded rotor with optimal thrust and energy efficiency in unmanned aerial vehicles. *In Proceedings of the 2018 IEEE 10th International Conference on Humanoid, Nanotechnology, Information Technology, Communication and Control, Environment and Management (HNICEM)*, Baguio City, Philippines, 29 November–2 December 2018.

[26] Moaad, Y.; Alaaeddine, J.; Jawad, K.; Tarik, B.K.; Lekman, B.; Hamza, J.; Patrick, H. Design and optimization of a ducted fan VTOL MAV controlled by Electric Ducted Fans. *In Proceedings of the 8th European Conference for Aeronautics and Space Sciences,* Madrid, Spain, 1-4 July 2019; pp. 1–14.

[27] Penkov, I.; Aleksandrov, D. Propeller shrouding influence on lift force of mini unmanned quadcopter. *Int. J. Automot Mech. Eng*. 2017, *14*, 4486–4495.

[28] Shukla, D.; Komerath, N. Rotor–duct aerodynamic and acoustic interactions at low Reynolds number. *Exp. Fluids* 2019, *60*, 1–14. http://dx.doi.org/10.1007/s00348-018-2668-z.

[29] Yonezawa, K.; Sugiyama, K.; Tanabe, Y.; Sunada, S. Development of a Ducted Rotor for Multicopters. *In Proceedings of the 6th Asian/Austrailian Rotorcraft Forum/Heli Japan*, Ishikawa, Japan, 7–9 November 2017.

[30] Yonezawa, K.; Matsumoto, H.; Sugiyama, K.; Tanabe, Y.; Tokutake, H.; Sunada, S. Aerodynamic Characteristics of a Quad-Rotor-Drone with Ducted Rotors. *In Proceedings of the 8th Asian/Austrailian Rotorcraft Forum*, Ankara, Turkey 30 October–2 November 2019.

[31] Bangura, M.; Melega, M.; Naldi, R.; Mahony, R. Aerodynamics of Rotor Blades for Quadrotors. *Fluid Dyn*. 2016. Available online: http://arxiv.org/abs/1601.00733 (arXiv: 1601 00733v1 [physics.flu-dyn], accessed on January 2016).

[32] Nguyen, D.H.; Liu, Y.; Mori, K. Experimental Study for Aerodynamic Performance

of Quadrotor Helicopter. *Trans. Jpn. Soc. Aeronaut Space Sci*. 2018, *61*, 29–39.

[33] Noda, R.; Nakata, T.; Ikeda, T.; Chen, D.; Yoshinaga, Y.; Ishibashi, K.; Rao, C.; Liu, H. Development of bio-inspired low-noise propeller for a drone. *J. Robot Mechatron.* 2018, *30*, 337–343.

[34] Ikeda, T.; Tanaka, H.; Yoshimura, R.; Noda, R.; Fujii, T.; Liu, H. A robust biomimetic blade design for micro wind turbines. *Renew Energy* 2018, *125*, 155–165. https://doi.org/10.1016/j.renene.2018.02.093.

[35] Pagliuca, G.; Kipouros, T.; Savill, M.A. Surrogate modelling for wing planform multidisciplinary optimisation using model-based engineering. *Int. J. Aerosp Eng*. 2019, *2019*, 4327481.

[36] Han, Z.; Zhang, K. Surrogate-Based Optimization. In *Real-World Applications of Genetic Algorithms*; IntechOpen: London, UK, 2012; doi:10.5772/36125.

[37] Bhatia, G.S.; Arora, G. Radial basis function methods for solving partial differential equations-A review. *Indian J. Sci. Technol*. 2016, *9*, 1–18.

[38] Koushki, M.; Jabbari, E.; Ahmadinia, M. Evaluating RBF methods for solving PDEs using Padua points distribution. *Alex. Eng. J.* 2020, *59*, 2999–3018. https://doi.org/10.1016/j.aej.2020.04.047.

Chapter 4 Experiment Validation

4.1 Experiment facility

In order to validate the results of CFD-based simulation, the measurements of lift force and torque generated by each propeller in different rotor-configurations without and with ducts are conducted experimentally. The experiment facility is comprised of the transmitter for starting up the propellers rotation, the power support, the measurement system of rotor-configuration, as well as the PC for interface of rotating speed, lift force and torque, as illustrated in Figure 4-1 (TAYA Engineering CO.,LTD.). The propellers adopted are from the quadrotor drone of DJI phantom 4 (Figure 4-1), which are purchased commercially, almost having identical characteristics with the propellers came from the quadrotor drone of DJI phantom 3 advanced. The propellers are equipped in a base platform elevating from the ground with a distance of 1 m (about 4D, D is the diameter of propeller) that can realize the height difference between the two pairs of propellers (Figure 4-1), which the quadrotor drone is considered out of ground effect in this height for the rotating propellers [1]. The motors (S-Motor Phantom4 DJI) are fixed on the motor mount plates in connection with the isolated 6-axis force sensors (S-LoadCell SFS016XS300R6 Leptrino) by the motor load cell joints and load cell mount bricks as illustrated in Figure 4-2. These components are supported by the motor angle set components that can adjust the tilt angle of propellers in the experiment, which are connected with the arm pipes by the arm-end motor mounts (as illustrated in Figure 4-2), resulting that it is available to adjust the tip distance among the propellers. In addition, a global sensor (6-axis sensor of PFS030YA151R6 Reptrino) for examining the total lift force and torque of multi propellers is installed under the base platform (as illustrated in Figure 4-2). As to the experiment of ducted rotor-configuration, the high-performance duct obtained in section 3.3.1 is firstly fabricated with plastic material (Nylon) in a thickness of 2 mm as shown in Figure 4-3. With a metal fitting and six rods, it can be assembled with connection of the motor, which generates a ducted-propeller in the experiment (as depicted in Figure 4-3).

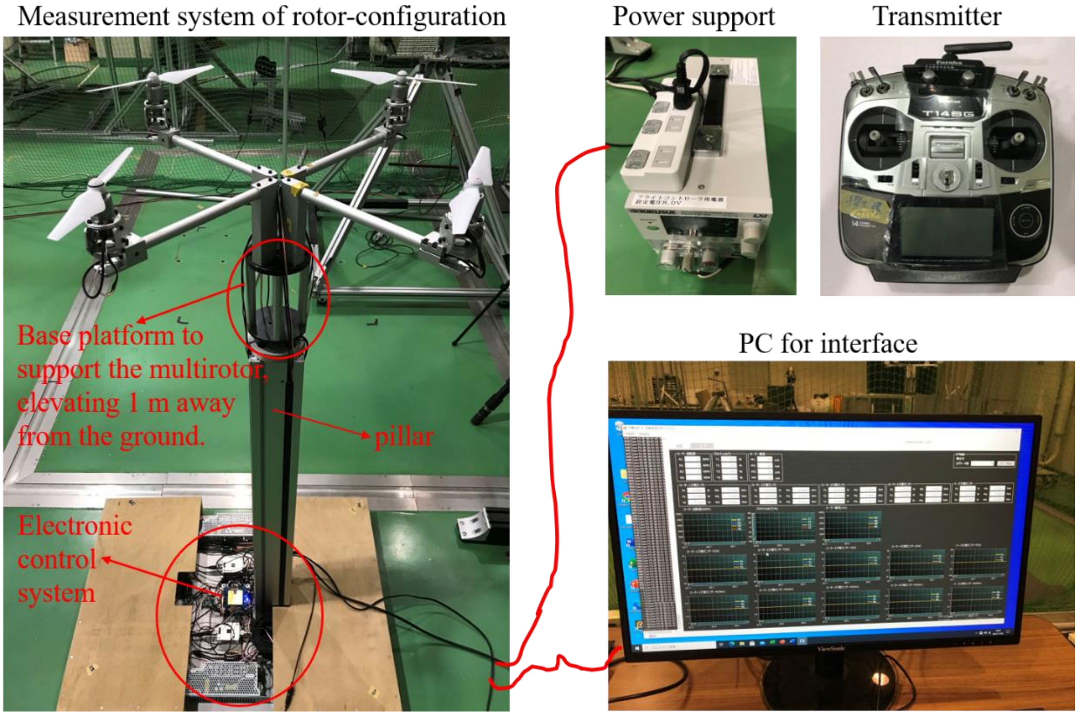

Figure 4-1 Illustration of the experiment facility.

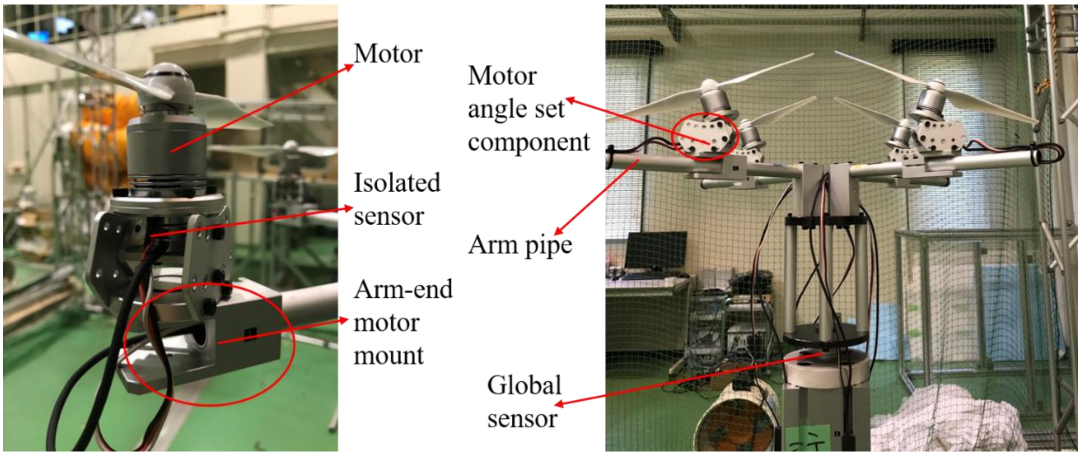

Figure 4-2 Illustration of the setting of components in the experiment for different rotor-configurations.

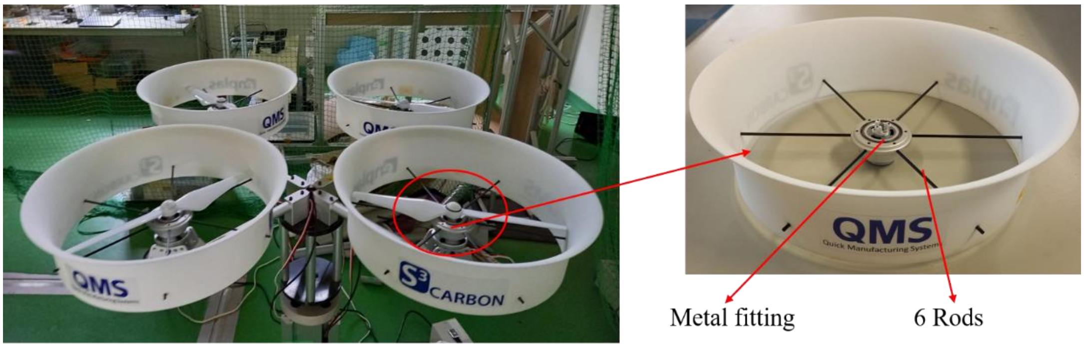

Figure 4-3 Illustration of the ducted rotor-configuration in the experiment.

4.2 Experiment cases

As depicted in Figure 4-1, the experiment procedure consists of the following steps in sequence: (1) as to the rotor-configuration case, set the non-ducted multi-propeller configuration with adjusting the parameters associated with tip distance, height difference and tilt angle. As to the ducted rotor-configuration case, set the ducted multi-propeller configuration with adjusting the parameters associated with tip distance and height difference; (2) check the operation of experiment apparatus, and define the rotation speed of propellers to be 5400 rpm. (3) input the power from the power support, start up the propellers rotation from the remote control by the transmitter, and collect the data of lift force and torque with the interval of 10 s after the propellers rotation is stable. (4) deal with the collected data and compare them with the results from CFD-based simulation. After one case is finished, the configuration related with tip distance, height difference and tilt angle should be adjusted for a new case, and conducted again in accordance with the experiment procedure.

In order to compare with the results of CFD-based simulation and examine the effects of non-ducted rotor-configuration and ducted rotor-configuration on aerodynamic performance, some discrete cases of non-ducted multi-propeller configurations regarding single parameter variation associated with tip distance, height difference and tilt angle are conducted firstly in the experiment, which is listed in Table 4-1; the discrete cases of non-ducted multi-propeller configurations about the variation of parameters mixture associated with height difference and tilt angle at a basic of fixed maximal tip distance are carried out secondly in the experiment, which is listed in Table 4-2; and ultimately the discrete cases of ducted multi-propeller configurations with respect to the variation of tip distance and height difference are performed in the experiment, which is listed in the Table 4-3.

Table 4-1 Cases of various rotor-configurations regarding the variations of single parameter in the experiment

$\boldsymbol{i = d_{14-23,\phi}/R}$	0.4	0.52	0.7	0.81	1.0	1.3	1.54
$\boldsymbol{i = h_{u24-l13}/R}$	0.2	0.6	1.0	1.2	2.0		
$\boldsymbol{i = h_{u23-l14}/R}$	0.2	0.6	1.0	1.2	2.0		
$\boldsymbol{\alpha}$	$-20°$	$-10°$	$10°$	$20°$			

Table 4-2 Cases of various rotor-configurations regarding the variations of parameters mixture in the experiment

Tilt angle ($\boldsymbol{\alpha}$)	**Height difference ($\boldsymbol{h/R}$)**		
$\mathbf{0}°$	0	1.0	2.0
$\mathbf{10}°$	0	1.0	2.0
$\mathbf{20}°$	0	1.0	2.0

Table 4-3 Cases of different ducted rotor-configurations in the experiment

Height difference ($\boldsymbol{h/R}$)	**Tip distance ($\boldsymbol{d/R}$)**				
2.0	1.54	1.18	0.97	0.82	0.46
1.2	1.54				0.46
1.0	1.54				0.46
0.6	1.54				0.46
0.2	1.54				0.46
0	1.54	1.18	0.97	0.82	0.46

4.3 Experiment results

4.3.1 Experiment results of non-ducted rotor-configuration

The calibration of the isolated sensor and global sensor was firstly conducted by the measurement of some fixed weights with hanging cross the isolated sensors, which it can be run for both the isolated sensor and global sensor. On the other hand, the measurement of fixed weight is performed with only putting the weight on the base platform of the experiment facilities, which leads to the operation of global sensor exclusively. The results of calibration are illustrated in Figures 4-4 and 4-5, which shows that it is available for the measurement of isolated sensor and global sensor due to the approximability to the weight theoretically.

Sequentially, the measurement about thrust of single propeller in different settings of rotation speed was carried out and compared with the results from the CFD-based simulations as depicted in Figure 4-6, where it shows that the thrust (T) of single propeller increases in a nearly linear manner with increasing the square of angular velocity (ω^2), with the results of experiment and simulation being consistent with each other even if there is a difference probably caused by the device vibration, as well as in accordance with the conclusion in previous studies [2-5].

Due to the limitation of experimental apparatus, the effects of tip distance, height difference and tilt angle on aerodynamic performances ($\overline{C_L}$ and $\overline{FM}$) of different quadrotor configurations in the experiment are conducted in terms of the parameters of $d_{14-23,\emptyset}$, $h_{u24-l13}$, $h_{u23-l14}$, α and the mixture of height difference ($h_{u24-l13}$) and tilt angle (α), which are depicted in Figures 4-7 to 4-10, with the average FM efficiency defined as [6]

$$\begin{cases}\overline{FM_{EXP}} = \dfrac{\overline{P_{RF}}}{\overline{P_{EXP}}}, \\ \overline{P_{EXP}} = \overline{Q_{EXP}} \cdot \omega\end{cases} \qquad (4\text{-}1)$$

where the parameters are similar to that in section 2.2.3. Comparing with the CFD-based simulation results, the results obtained from experiment are also illustrated in Figures 4-7 to 4-10, where the results from numerical simulations are in accordance with that from experiment. Figure 4-7 shows that the $\overline{C_L}$ increases with increasing the dimensionless parameter $d_{14-23,\phi}/\mathrm{R}$, realizing a maximum increase rate about 9% based on the measurement of global sensor but about 3.5% according to the measurement of isolated sensor compared to that of basic quadrotor configuration. A maximum increase rate about 3.5% of $\overline{FM}$ was observed sharing the same trend compared to that of basic configuration. Figure 4-8 shows that the parameter of $h_{u24-l13}$ exhibits a better aerodynamic performance than the parameter of $h_{u23-l14}$, being significant with a maximum increase rate of $\overline{C_L}$ about 2.8% from the isolated sensor measurement, correspondingly with a maximum increase rate of $\overline{FM}$ about 3.1% compared to that of basic configuration, while it is about 5% regarding the maximum increase rate of $\overline{C_L}$ according to the global sensor measurement. The tilt angle of α provides a slight improvement on $\overline{C_T}$ with a maximum increase rate about 3% based on the measurement of either the isolated sensor or the global sensor, accompanying a maximum increase rate of $\overline{FM}$ about 3% too during the angle variation as illustrated in Figure 4-9. The optimal rotor-configuration based on the limited discrete cases is also assigned at the configuration with maximum height difference and zero tilt angle on a basis of the fixed maximum tip distance as shown in Figure 4-10. All the results from experiment further certificate the reliability of the findings through numerical simulations.

4.3.2 Experiment results of ducted rotor-configuration

The duct is fabricated based on the high-performance duct model obtained in section 3.3.1 and employed in the experiment of ducted rotor-configuration. The effects on aerodynamic performance of different ducted multi-propeller configurations (Figure 4-11) in the quadrotor drone are investigated through some discrete cases adopted in the experiment, with the results illustrated in Figures 4-12 and 4-13, where the numerical simulation results are consistent with the experiment results. Figure 4-12 shows that the tip distance change largely impairs the aerodynamic performance associated with lift force production and FM efficiency at small values ($^{d}/_{R}$ = 0.97 ~ 0.46). Figure 4-13 indicates that the aerodynamic performance will be improved during a certain range ($^{h}/_{R}$ = 1.2 ~ 0.2) in terms of adjusting the height difference, while it shows a slight fluctuation of decreasing FM efficiency between $^{h}/_{R}$ = 0 and $^{h}/_{R}$ = 2.0 with adjusting the height difference when the tip distance is fixed at the maximum value. Although there is a little difference regarding the FM efficiency in the height difference adjustment at fixed d_{max}, it has a very small influence on the increase rate of aerodynamic performance compared to that in the maximum multi-propeller configuration, which manifests that the experiment results on ducted rotor-configuration are in accordance with the findings obtained from the numerical simulations.

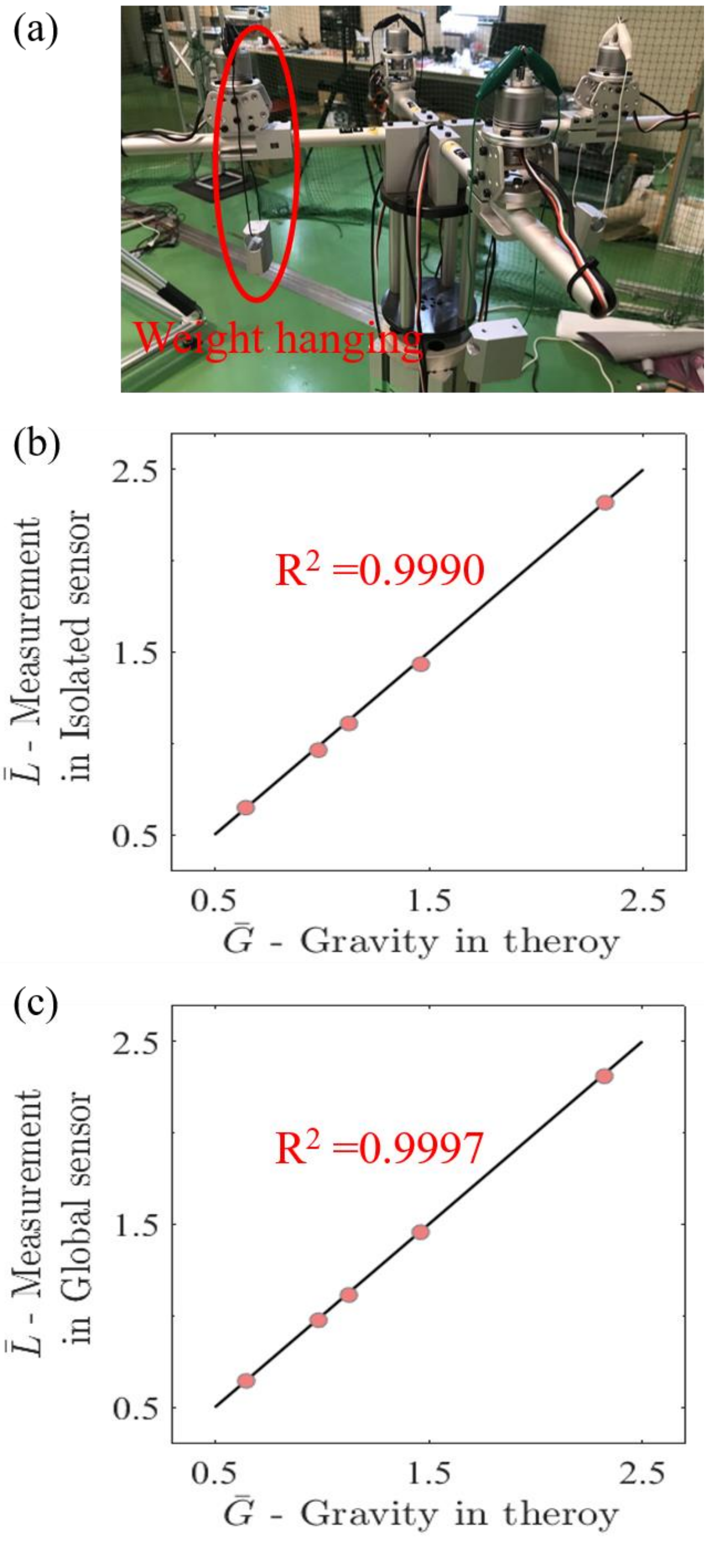

Figure 4-4 Calibration of the isolated sensor in the experiment.

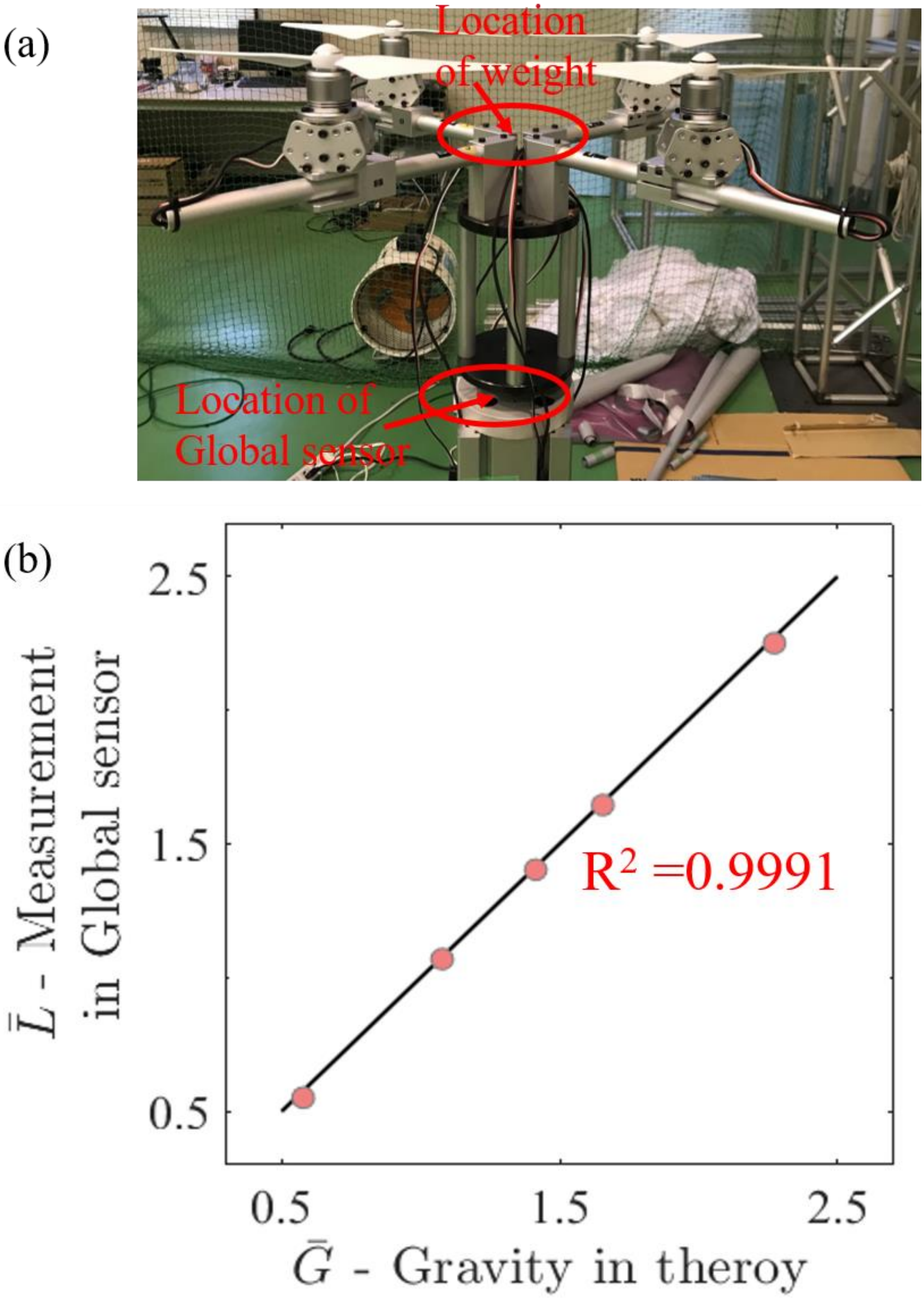

Figure 4-5 Calibration of the global sensor in the experiment.

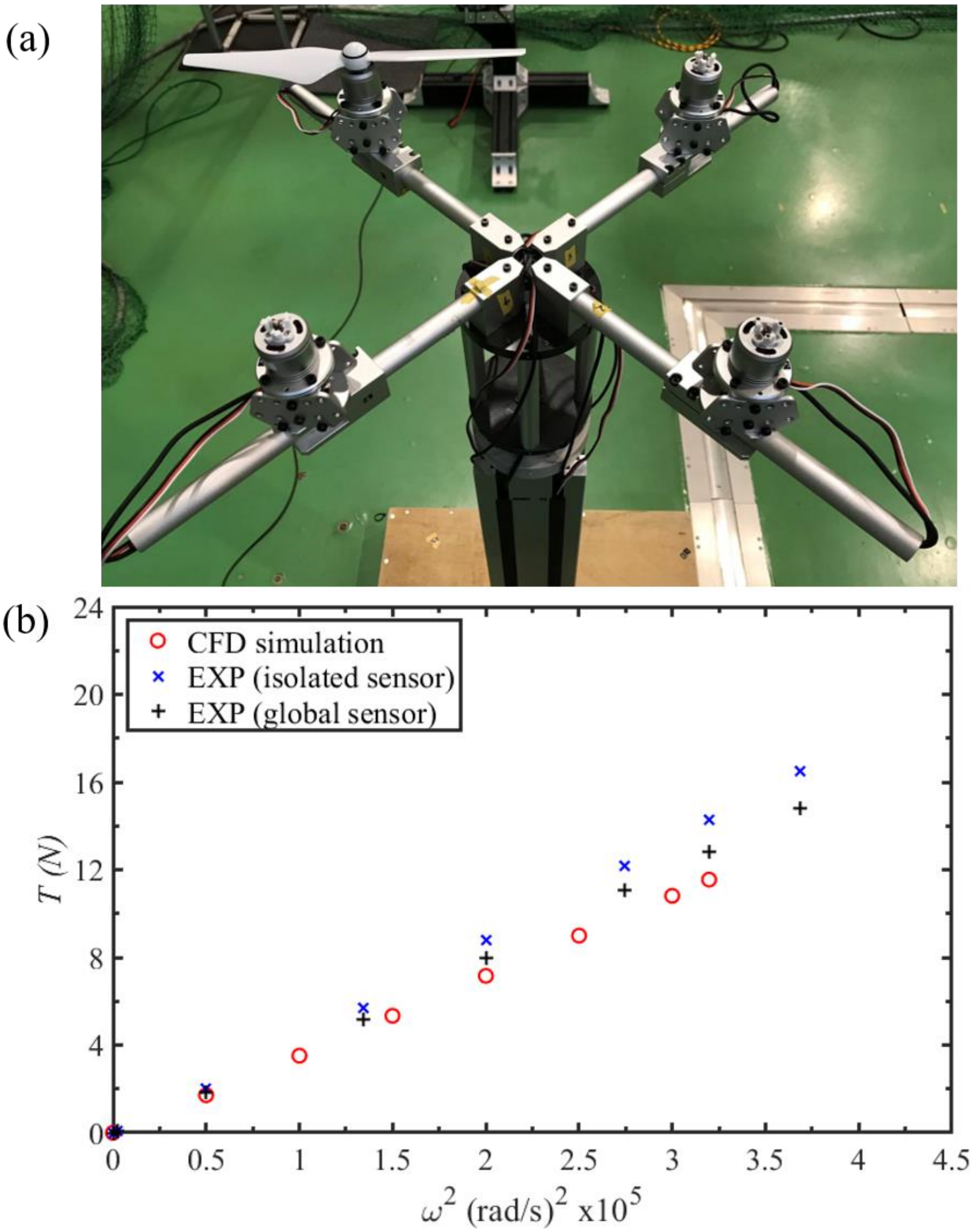

Figure 4-6 Illustration of the thrust of single propeller in the experiment.

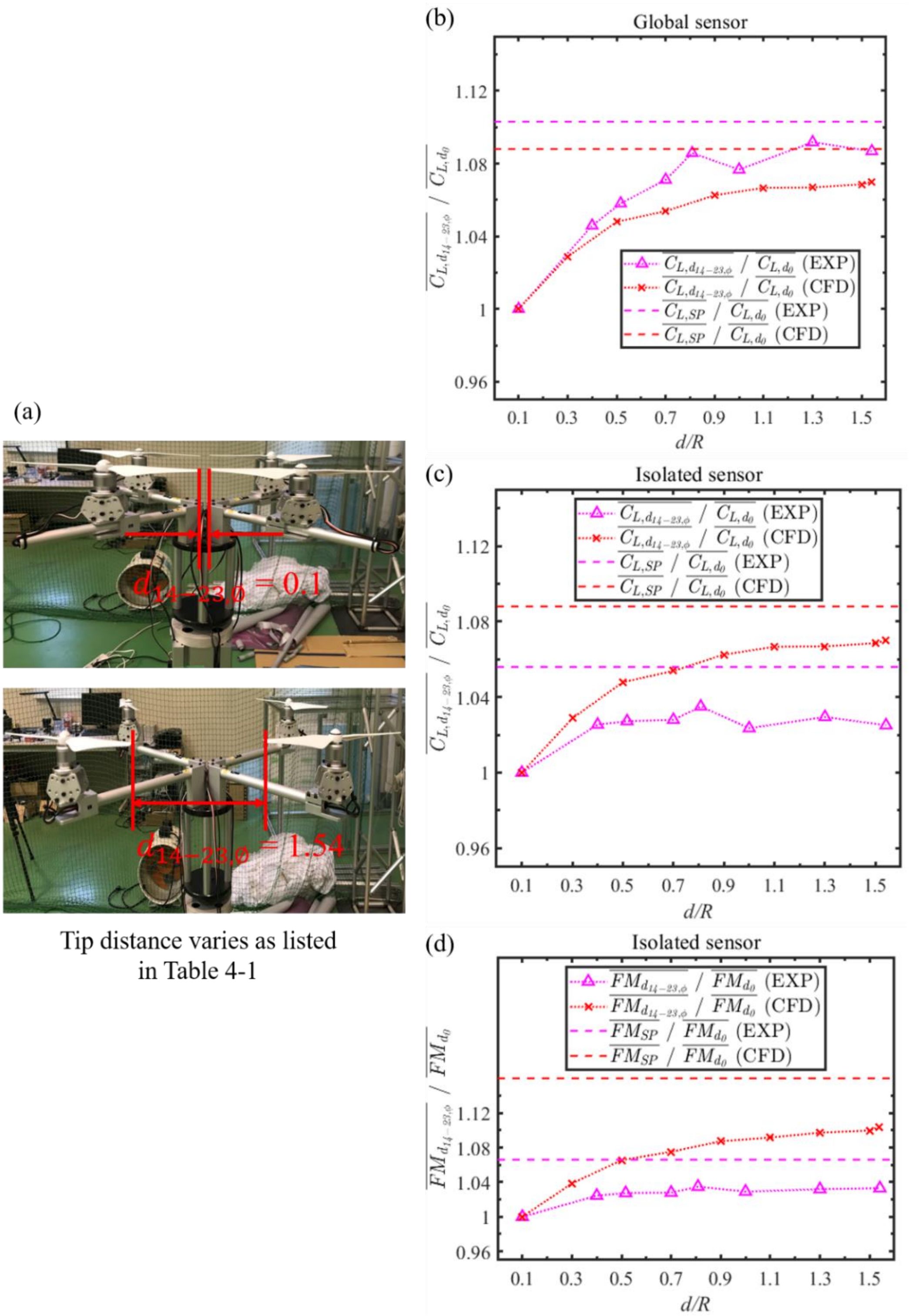

Tip distance varies as listed
in Table 4-1

Figure 4-7 Aerodynamic performance ($\overline{C_L}$ and $\overline{FM}$) vs tip distance of $d_{14-23,\emptyset}$ in the experiment.

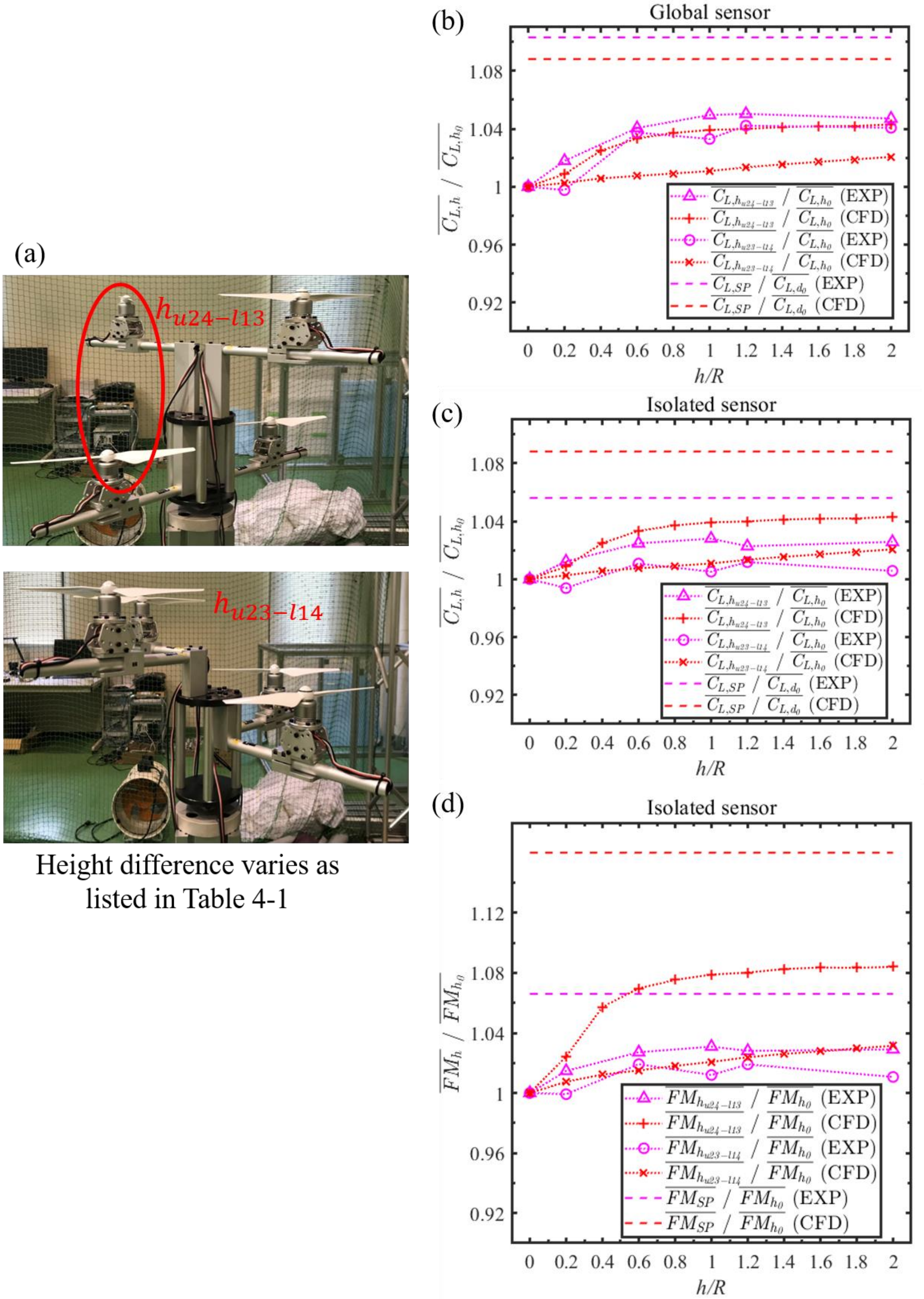

Height difference varies as listed in Table 4-1

Figure 4-8 Aerodynamic performance ($\overline{C_L}$ and $\overline{FM}$) vs height difference of $h_{u24-l13}$ and $h_{u23-l14}$ in the experiment.

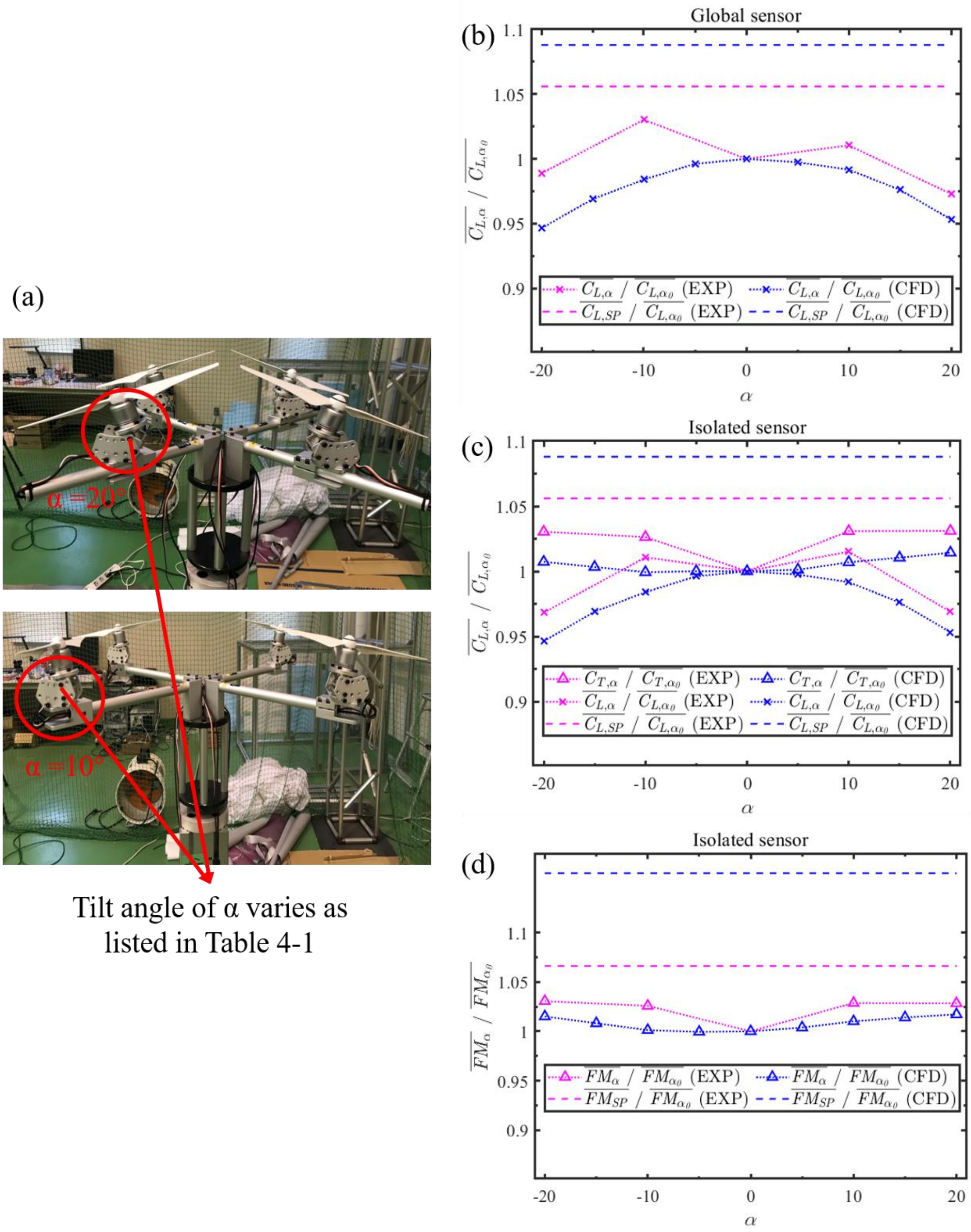

Figure 4-9 Aerodynamic performance ($\overline{C_L}$ and $\overline{FM}$) vs tilt angle of α in the experiment.

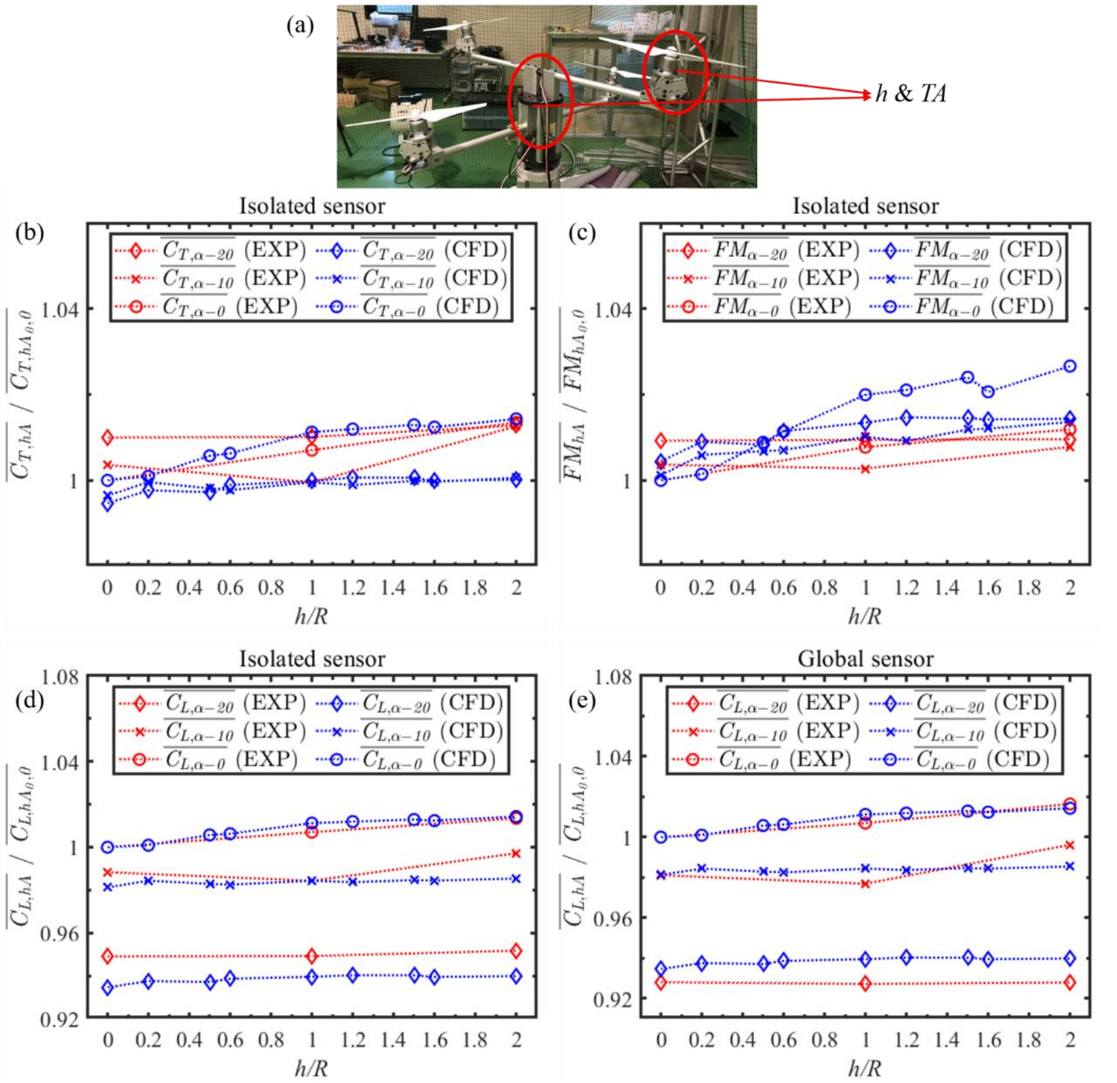

Figure 4-10 Aerodynamic performance ($\overline{C_L}$ and $\overline{FM}$) vs different rotor-configurations with height difference (h of $h_{u24-l13}$) and tilt angle (TA of a) in the experiment.

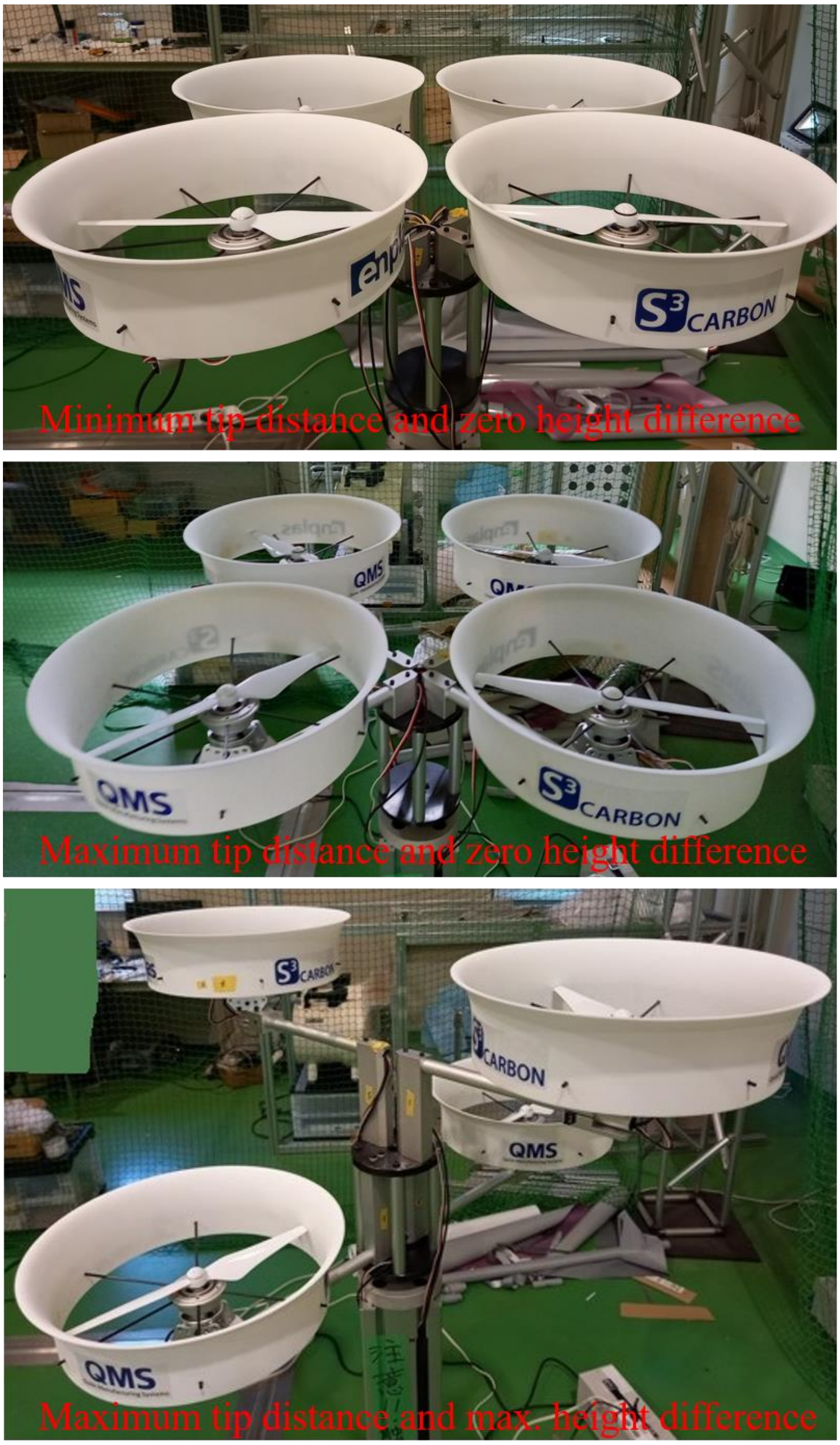

Figure 4-11 Illustration of different cases regarding ducted rotor-configurations in the experiment.

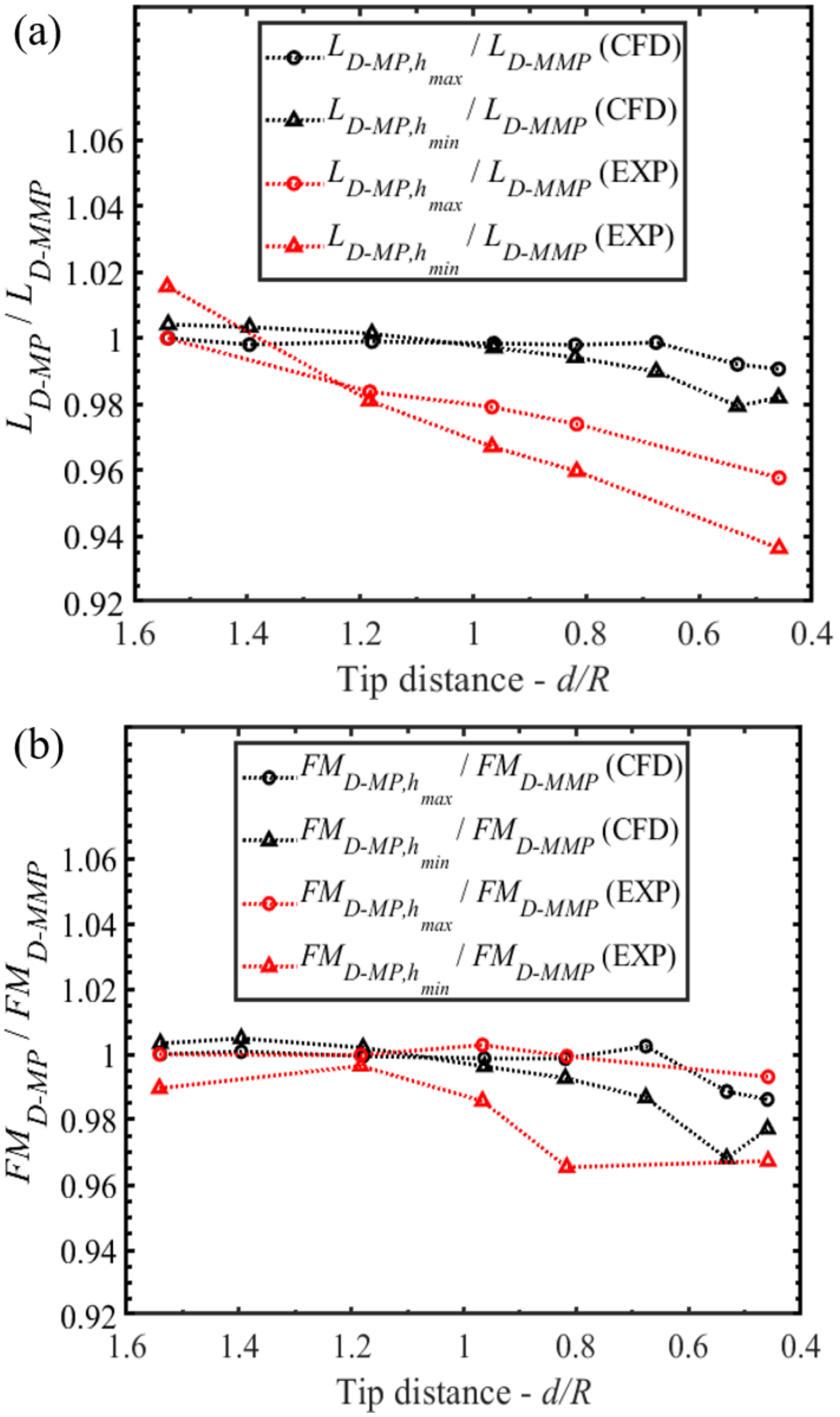

Figure 4-12 Lift force and FM efficiency vs. d/R in various ducted multirotor configurations: $L_{D-MP,h_{max}}$ and $FM_{D-MP,h_{max}}$ with h_{max} fixed and $L_{D-MP,h_{min}}$ and $FM_{D-MP,h_{min}}$ with h_{min} fixed in the experiment.

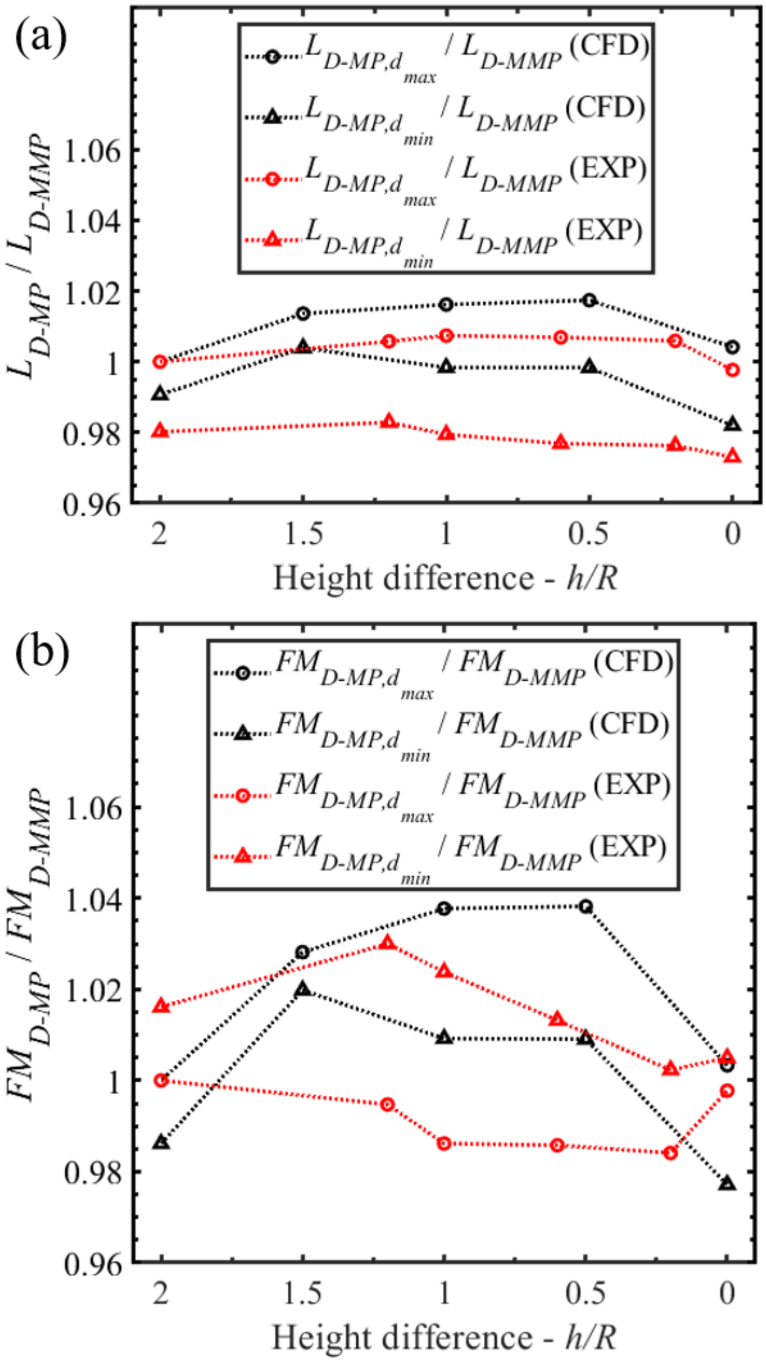

Figure 4-13 Lift force and FM efficiency vs. h/R in various ducted multirotor configurations: $L_{D-MP,d_{max}}$ and $FM_{D-MP,d_{max}}$ with d_{max} fixed and $L_{D-MP,d_{min}}$ and $FM_{D-MP,d_{min}}$ with d_{min} fixed in the experiment.

4.4 Conclusions

The experiment results complied with the findings obtained from the numerical simulations proves the credibility of the multi-propeller configuration design relative to the optimal rotor-configuration and the optimal ducted rotor-configuration, which manifests that it is valuable and practical to explore the optimal non-ducted/ducted rotor-configuration for improving the aerodynamic performance by analyzing the interactions among different propellers. Eventually, the aerodynamic performance of non-ducted multi-propeller can be improved with a large tip distance, some height difference and zero tilt angle, while the aerodynamic performance of ducted multi-propeller can be improved with an appropriate height difference and a minimal tip distance, which provides a potential optimal design for non-ducted/ducted quadrotor drone.

Reference

[1] Tanabe Y, Sugawara H, Sunada S, Yonezawa K, Tokutake H. Quadrotor drone hovering in ground effect. *J Robot Mechatronics,* 2021, 33, 339–347. https://doi.org/10.20965/jrm.2021.p0339.

[2] Aleksandrov D, Penkov I. Optimal gap distance between rotors of mini quadrotor helicopter. *8th International DAAAM Baltic Conference*, Tallinn, Estonia, 2012.

[3] Shukla D, Komerath N. Multirotor drone aerodynamic interaction investigation. *Drones*, 2018, 2, 1–13.

[4] Yoon S, Lee H C, Pulliam T H. Computational Analysis of Multi-Rotor Flows. *54th AIAA Aerospace Science Meeting*, San Diego, California, USA, 2016.

[5] Lei Y, Wang J L. Aerodynamic Performance of Quadrotor UAV with Non-Planar Rotors. *Applied Science*, 2019, 9, 2779.

[6] Noda R, Nakata T, Ikeda T, Chen D, Yoshinaga Y, Ishibashi K, Rao C, Liu H. Development of bio-inspired low-noise propeller for a drone. *Journal of Robotics and Mechatronics*, 2018, 30, 337–343.

Chapter 5 Conclusions and Perspectives

5.1 Conclusions of biomimetic rotor-configuration design

Due to the extensive applications in different fields and the great interests drawn from the academic and industrial fields, it is significant to further improve the aerodynamic performance of current quadrotor drones, which aims to realize the longer endurance of flight, the less cost of power, the high efficiency of whole system and so on in quadrotor drone. Motived by the bioinspiration from the exquisite flight performance of insects and birds, we proposed the biomimetic rotor-configuration designs associated with adjustment of tip distance, height difference and tilt angle of propellers according to the consideration of the six-degree of freedom of the rotor system. We concluded that the optimal non-ducted rotor-configuration is a configuration having large tip distance, some height difference with zero tilt angle, which optimized the lift force production and FM efficiency compared with those in basic configuration. In order to further reduce the dimension of drone frame while maintain the high aerodynamic performance, we explored the optimal ducted-rotor configuration with employing a high-performance duct. In conclusion, we found that the optimal ducted-rotor configuration is a configuration having a minimal tip distance and an appropriate height difference, which optimized the aerodynamic performance associated with lift force production and FM efficiency compared with those in the former obtained optimal rotor-configuration with ducts. The reason of realizing the optimal configuration comes from the least interference of downwash among adjacent propellers and maximum positive interaction among upper and lower propellers with additional lift caused by a suction pressure gradient on the duct inlet surface in those configurations. Furthermore, during the analyses of non-ducted configuration, it is found that the tip distance-induced interactions could most alter lift force production and hence lead to remarked improvement in FM efficiency, and the height difference also plays a key role in the aerodynamic performance improvement, while the tilt angle effect is less important. Whereas, as to the ducted configuration, it is indicated that the tip distance-induced interactions have a noticeable effect in impairing the lift force production and FM efficiency but are limited to small tip distances, while the height difference-induced interactions have an impact on enhancing the aerodynamic performance over a certain range. Owing to the experiment validation, these conclusions are convincing and reliable for the optimal design in quadrotor drone. Beyond the improvement of aerodynamic performance with the biomimetic rotor-configuration design, it also has an influence on the ground effect, aero-acoustic, and maneuverability of the biomimetic rotor-configuration design because of the variation of aerodynamic induce velocity and aerodynamic pressure in the rotor system caused by the different rotor-configurations when the quadrotor drone flied in low-altitude, close to obstacles, through narrow channel, and ran in take-off and landing, which is potential and significant for the flight performance improvement of quadrotor drone system.

5.2 Ground effect of biomimetic rotor-configuration design

As the outwash from the quadrotor was mainly determined by the direction relative to the quad-rotor layout [1], it is reasonable to consider that the biomimetic rotor-configuration design can affect the ground effect of quadrotor drone. Owing to that we have obtained an optimal multirotor configuration in chapter 2, we can compare the rotor performance of basic multirotor configuration and optimal multirotor configuration with ground effect in hover, where the distance of the rotor bottom away from the ground to examine the ground effect on quadrotor drone is set to be 0.25D, 0.5D, 0.75D, 1D, 2D, 3D (D is the diameter of propeller came from the quadrotor drone of DJI phantom 3 advanced) [1], accompanying with the configurations out of ground effect as illustrated in Figure 5-1. Furthermore, the rotor performance of thrust coefficient, torque coefficient and figure of merit (*FM*) will be adopted in the investigation for ground effect of quadrotor drone [1], which are defined as

$$C_T = \frac{T}{\rho \pi R^2 U^2}, \tag{5-1}$$

where T is the thrust of a single rotor in quadrotor drone, which is calculated by the average thrust of quad rotors, ρ is the air density, R is the radius of propeller, and U is velocity of wingtip, respectively.

$$C_Q = \frac{Q}{\rho \pi R^3 U^2}, \tag{5-2}$$

where Q the torque generated by a single rotor in quadrotor drone, which is identical to the average torque of quad rotors. And

$$FM = \frac{(C_T)^{\frac{3}{2}}/\sqrt{2}}{C_Q}. \tag{5-3}$$

In addition, the tilt angle design also impacts the outwash from the quadrotor, which may also have an influence on ground effect. Considering that it only has little lift force loss when the tilt angle varied from zero to +10° in chapter 2, we will also utilize the tilt angle design of α =+5° and α =+10° in the basic multirotor configuration and optimal multirotor configuration to examine the ground effect of different configurations with tilt angle by use of the distance between the rotor bottom and the ground to be 0.25D, 0.5D, 0.75D, 1D, 2D, 3D (Figure 5-1), accompanying with the configurations out of ground effect. What's more, as the duct design also has influence on the outwash from the quadrotor, the optimal ducted multirotor configuration as well as this configuration removing the ducts will also be studied to examine their influence on the ground effect of quadrotor drone. Based on the results of rotor-configuration with tilt angle, the inclination of ducted-propeller will be a potential choice for the investigation of examining the influence of rotor-configuration on ground effect of quadrotor drone. Eventually, the findings of rotor-configuration on ground effect will provide a perspective in low-altitude flight performance in the design of quadrotor drone.

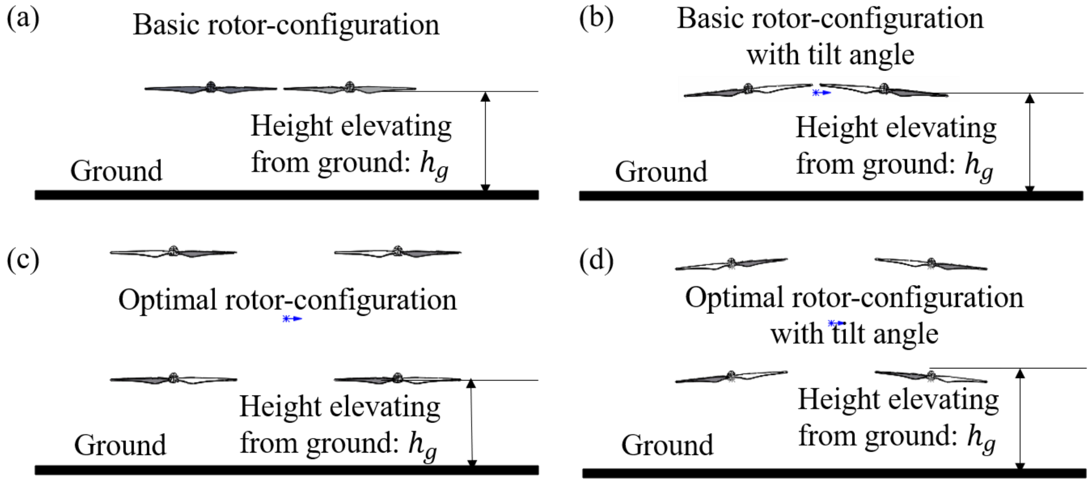

Figure 5-1 Illustration of propeller height elevating from ground for the investigation of ground effect in quadrotor drone.

5.3 Aero-acoustic performance of biomimetic rotor-configuration design

The two main causes of aircraft noise generation come from engine and airframe [2]. Airfoil self-noise is generated from the interaction between the airfoil blade and the turbulence produced in its own boundary layer and near wake [3]. If the structures of quadrotor drone is capable of controlling the vortex shedding mode, it would be feasible to the airfoil noise reduction, such as the biomimetic rotor-configuration design associated with tip distance, height difference, and tilt angle with or without ducted-propeller. Therefore, the aero-acoustic effect of varying the rotor-configuration with or without ducts over the sound pressure level at the receiver location will be analyzed in the future for the research of aero-acoustic performance of biomimetic rotor-configuration design. Moreover, the large eddy simulation (LES) turbulence modelling and the aero-acoustic analogy model of Ffowcs-Williams and Hawkings in Ansys Fluent environment will be adopted to evaluate the acoustics level at the designated receiver location of sphere surface in different radius, where the biomimetic rotor-configuration designs to be examined are the basic configuration with and without ducts, and the optimal rotor-configuration with and without ducts, as illustrated in Figure 5-2. Further it can also be investigated with the ducted propeller design in different configurations in examining the aero-acoustic performance of biomimetic rotor-configuration designs. Thus, the results of biomimetic rotor-configuration design on aero-acoustic performance will be obtained for contributing to the design of multirotor drone, which is promising to reduce the noise of quadrotor drone in the flight.

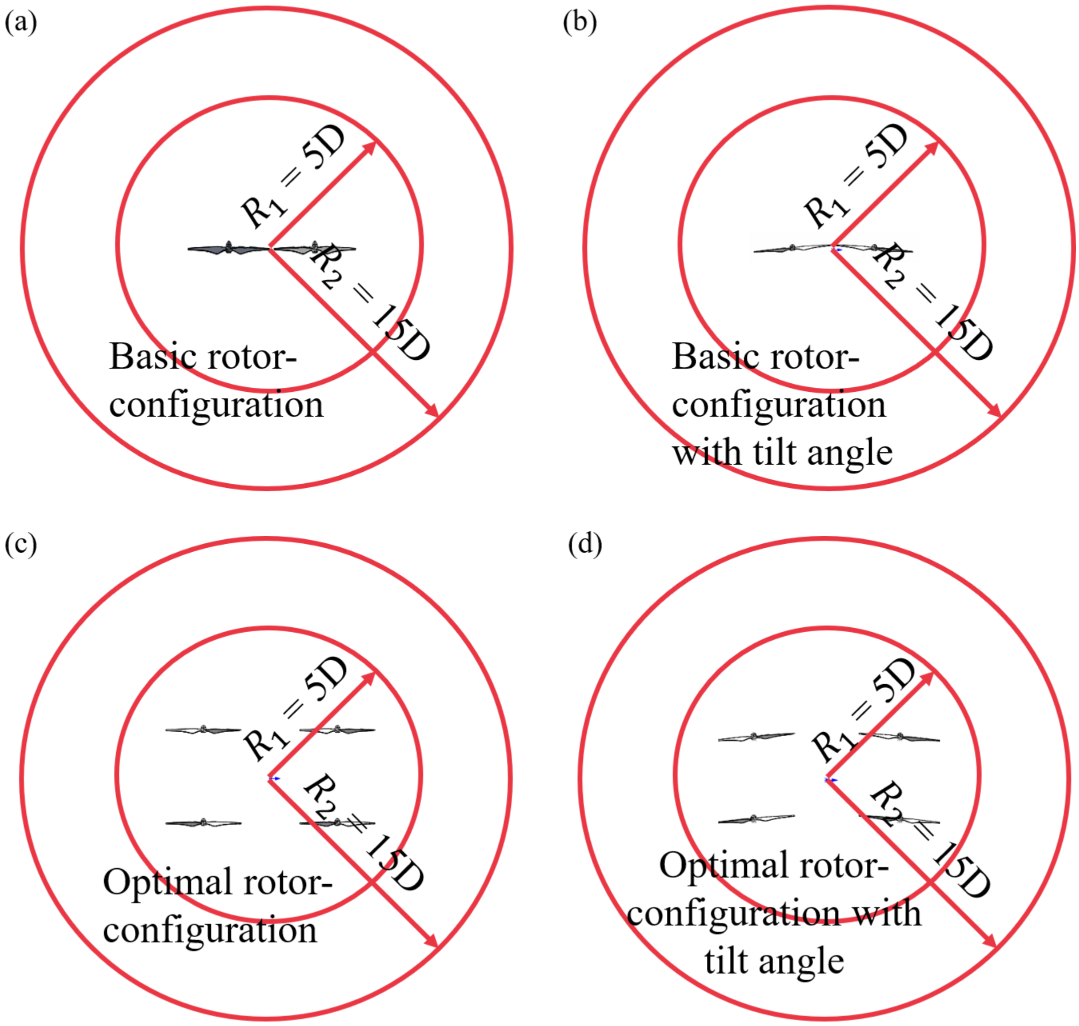

Figure 5-2 Illustration of rotor-configurations for the investigation of aero-acoustic in quadrotor drone.

5.4 Effect on maneuverability of biomimetic rotor-configuration design

The aerodynamic performance variation is also relative to the maneuverability of quadrotor drone [4,5], resulting from the power output during flight. As the biomimetic rotor-configuration associated with tip distance, height difference and tilt angle can improve the aerodynamic performance of drone, as well induce the moment change of drone caused by the variation of lift force or the arm of lift force, it will bring about the influence on maneuverability of drone. Furthermore, we conceive a design of overlapping propellers in different height difference in order to reduce the frame of optimal rotor-configuration obtained in chapter 2. However, it has a total lift force loss in the situation of propellers overlapping investigated by the experiment (as illustrated in Figure 5-3), although it probably affects the maneuverability because of the variation of the lift force, the arm of lift force and the power output regarding the quadrotor drone, we will abandon this design because of the lift force loss. Thus, for the biomimetic rotor-configuration designs on maneuverability of quadrotor drone, we will examine the flight characteristics of basic and optimal rotor-configurations with and without tilt angle in the situations with and without wind, as illustrated in Figure 5-4. What’s more, the duct has an effect on the moment of quadrotor drone in windy or edgewise flow situation, which may also impact on the maneuverability of quadrotor drone. Thus, the ducted-rotor configuration will also be investigated on the maneuverability of quadrotor drone in the future. In addition, although there were some researches that investigated the modeling, design and simulation of the flight control with tilt rotors in quadrotor drones, they were mainly conducted with a fixed angle of tilt rotor in the researches [6-10]. How does the time-varying stroke-plane realized by tilt angle affect the maneuverability of quadrotor drone was still poorly understood until now. Thus, it also has a significant potential to manipulate the quadrotor drone by adjusting the tilt angle time-varyingly to realize a fast response or feedback in the attitude and altitude control compared to the traditional control strategy of just adjusting the rotation speed during the maneuverability of quadrotor drone. Therefore, considering these factors and the prerequisite that the aerodynamic capabilities of required adjustments with respect to these biomimetic rotor-configuration designs have been investigated, it has a great perspective for investigating the effect on maneuverability of biomimetic rotor-configuration designs and developing a drone with creative assembly structure and the agile maneuverability in the future.

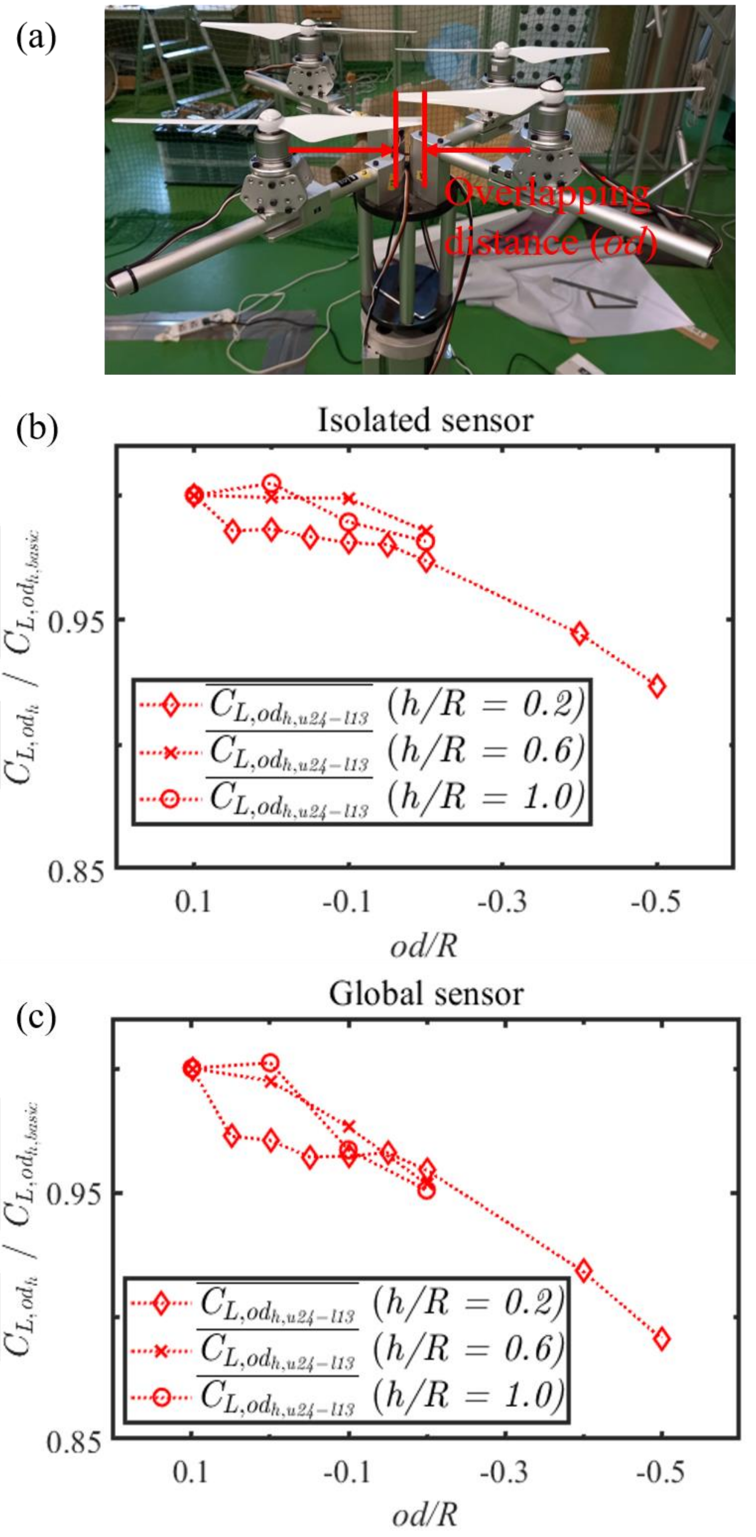

Figure 5-3 Illustration of the aerodynamic effect of overlapping propellers in different height difference ($h_{u24-l13}$) from the experiment.

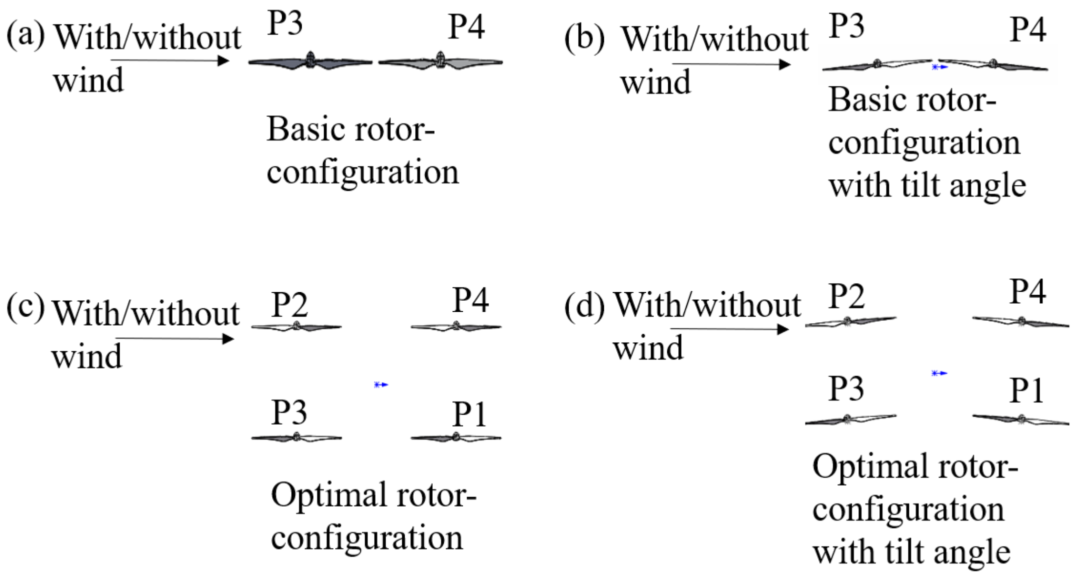

Figure 5-4 Illustration of rotor-configurations for the investigation of maneuverability in quadrotor drone.

Reference

[1] Tanabe Y, Sugawara H, Sunada S, Yonezawa K, Tokutake H. Quadrotor drone hovering in ground effect. *J Robot Mechatronics,* 2021, 33, 339–347. https://doi.org/10.20965/jrm.2021.p0339.

[2] Aamir MA, Zaheer SQ. Aeroacoustics analysis of 2D UAV wing at different flap deflections and incorporation of bio inspired aeroacoustics reduction techniques. *Proc. 2018 15th Int. Bhurban Conf. Appl. Sci. Technol. IBCAST 2018*, vol. 2018- Janua, 2018, 593–599. https://doi.org/10.1109/IBCAST.2018.8312285.

[3] Wang J, Zhang C, Wu Z, Wharton J, Ren L. Numerical study on reduction of aerodynamic noise around an airfoil with biomimetic structures. *J Sound Vib,* 2017, 394, 46–58. https://doi.org/10.1016/j.jsv.2016.11.021.

[4] Simone MCDE, Giovanni V, Ii P, Corso F, Napoli UI, Giovanni V, et al. Influence of Aerodynamics on Quadrotor Dynamics. 2015, 111–118. https://doi.org/10.13140/RG.2.1.5099.3128.

[5] Perozzi G. A toolbox for quadrotors: from aerodynamic science to control theory. To cite this version: HAL Id: hal-01696344 A toolbox for quadrotors: from aerodynamic science to control theory. 2018, 1–25.

[6] Ryll M, Bülthoff HH, Giordano PR. Modeling and control of a quadrotor UAV with tilting propellers. *Proc. - IEEE Int. Conf. Robot. Autom.*, 2012, 4606–4613. https://doi.org/10.1109/ICRA.2012.6225129.

[7] Ryll M, Bulthoff HH, Giordano PR. First flight tests for a quadrotor UAV with tilting propellers. *Proc. - IEEE Int. Conf. Robot. Autom.*, 2013, 295–302. https://doi.org/10.1109/ICRA.2013.6630591.

[8] Ferrarese G, Giulietti F, Avanzini G. Modeling and simulation of a quad-tilt rotor aircraft. *IFAC Proc. Vol.,* vol. 2, IFAC, 2013, 64–70. https://doi.org/10.3182/20131120-3-FR-4045.00037.

[9] Fukuda T, Sakaguchi A, Takimoto T, Ushio T. Modeling and Stabilization of the Novel Quadrotor with Tilting Propeller. 2016, 173–176.

[10] Henrique Bezerra Diógenes, Davi Antônio dos Santos. Modelling, Design and Simulation of a Quadrotor with Tilting Rotors Actuated by a Memory Shape Wire. *An. do IX Congr. Nac. Eng*. Mecânica, 2016. https://doi.org/10.20906/cps/con-2016-0452.

List of Abbreviations

FM	Figure of merit
UAV	Unmanned Aerial Vehicle
MAV	Micro Aerial Vehicle
VTOL	Vertical Take-Off and Landing
CFD	Computational Fluid Dynamics
EXP	Experiment
RANS	Reynolds Averaged Navier-Stokes
SST	Shear Stress Transport
RBF	Radial Basis Function
DoE	Design of Experiment
UD	Uniform Design
IMQ	Inverse Multiquadric
SP	Non-ducted Single Propeller
MP	Non-ducted Multi-propeller
BMP	Non-ducted Basic Multi-propeller
LTMP	Large Tip Multi-propeller
MMP	Non-ducted Maximum Multi-propeller
D-SP	Ducted Single Propeller
D-MP	Ducted Multi-propeller
D-MMP	Ducted Maximum Multi-propeller
D-SMP	Ducted Sub-maximum Multi-propeller
D-BMP	Ducted basic Multi-propeller
TA	Tilt Angle
LEV	Leading-edge Vortex
TV	Wing Tip Vortex
TEV	Trailing-edge Vortex

Published papers for thesis

[1] Y. Li, K. Yonezawa, R. Xu, H. Liu, A Biomimetic Rotor-Configuration Design for Optimal Aerodynamic Performance in Quadrotor drone. *Journal of Bionic Engineering*. 18: 824-839 (2021). https://doi.org/10.1007/s42235-021-0069-0.

[2] Y. Li, K. Yonezawa, H. Liu, Effect of ducted-rotor configuration on aerodynamic performance in quadrotor drone. *Drones*. 5(3), 101 (2021). https://doi.org/10.3390/drones5030101.

[3] T. Nakata, R. Noda, T. Ikeda, D. Chen, Y. Yoshinaga, K. Ishibashi, C. Rao, M. Hirose, Y. Li, and H. Liu, Development of bio-inspired low-noise propeller for a drone, *ImPACT Tough Robotics Challenge – A National Project of Disaster Robotics Aiming at Disruptive Innovation in Safety and Security* (2018).